Graphene and Boron Nitride: Members of Two Dimensional Material Family

A Thesis Submitted to the University of Manchester for the Degree of Doctor of Philosophy in the Faculty of Engineering and Physical sciences

2011

By

Ibtsam Riaz

School of Physics and Astronomy

Contents

List of figures

7

9

List of Tables

Abstract

Graphene and monoatomic boron nitride as members of the new class of two dimensional materials are discussed in this thesis. Since the discovery of graphene in 2004, various aspects of this one atom thick material have been studied with previously unexpected results. Out of many outstanding amazing properties of graphene, its elastic properties are remarkable as graphene can bear strain up to 20% of its actual size without breaking. This is the record value amongst all known materials. In this work experiments were conducted to study the mechanical behaviour of graphene under compression and tension. For this purpose graphene monolayers were prepared on top of polymer (PMMA) substrates. They were then successfully subjected to uniaxial deformation (tension- compression) using a micromechanical technique known as cantilever beam analysis. The mechanical response of graphene was monitored by Raman spectroscopy. A nonlinear behaviour of the graphene G and 2D Raman bands was observed under uniaxial deformation of the graphene monolayers. Furthermore the buckling strength of graphene monolayers embedded in the Polymer was determined. The critical buckling strain as the moment of the final failure of the graphene was found to be dependent on the size and the geometry of the graphene monolayer flakes. Classical Euler analysis show that graphene monolayers embedded in the polymer provide higher values of the critical buckling strain as compared to the suspended graphene monolayers. From these studies we find that the lateral support provided by the polymer substrate enhances the buckling strain more than 6 orders of magnitude as compared to the suspended graphene. This property of bearing stress more than any other material can be utilized in different applications including graphene polymer nanocomposites and strain engineering on graphene based devices. The second part of the thesis focuses on a two dimensional insulator, single layer boron nitride. These novel two dimensional crystals have been successfully isolated and thoroughly characterized. Large area boron nitride layers were prepared by mechanical exfoliation from bulk boron nitride onto an oxidized silicon wafer. For their detection, it is described that how varying the thickness of SiO_2 and using optical filters improves the low optical contrast of ultrathin boron nitride layers. Raman spectroscopy studies are presented showing how this technique allows to identify the number of boron nitride layers. The Raman frequency shift and intensity of the characteristic Raman peak of boron nitride layers of different thickness was analyzed for this purpose. Monolayer boron nitride shows an upward shift as compared to the other thicknesses up to bulk boron nitride. The Raman intensity decreases as the number of boron nitride layers decreases. Complementary studies have been carried out using atomic force microscopy. With the achieved results it is now possible to successfully employ ultrathin boron nitride crystals for precise fabrication of artificial heterostrutures such as graphene-boron nitride heterostrutures.

DECLARATION

No portion of the work referred to in the thesis has been submitted in support of an application for another degree or qualification of this or any other university or other institute of learning;

COPYRIGHT STATEMENT

i. The author of this thesis (including any appendices and/or schedules to this thesis) owns certain copyright or related rights in it (the "Copyright") and s/he has given The University of Manchester certain rights to use such Copyright, including for administrative purposes.

ii. Copies of this thesis, either in full or in extracts and whether in hard or electronic copy, may be made **only** in accordance with the Copyright, Designs and Patents Act 1988 (as amended) and regulations issued under it or, where appropriate, in accordance with licensing agreements which the University has from time to time. This page must form part of any such copies made.

iii. The ownership of certain Copyright, patents, designs, trade marks and other intellectual property (the "Intellectual Property") and any reproductions of copyright works in the thesis, for example graphs and tables ("Reproductions"), which may be described in this thesis, may not be owned by the author and may be owned by third parties. Such Intellectual Property and Reproductions cannot and must not be made available for use without the prior written permission of the owner(s) of the relevant Intellectual Property and/or Reproductions.

iv. Further information on the conditions under which disclosure, publication and commercialisation of this thesis, the Copyright and any Intellectual Property and/or Reproductions described in it may take place is available in the University IP Policy (see http://www.campus.manchester.ac.uk/medialibrary/policies/intellectual-property.pdf), in any relevant Thesis restriction declarations deposited in the University Library, The University Library's regulations (see http://www.manchester.ac.uk/library/aboutus/regulations) and in The University's policy on presentation of Theses

ACKNOWLEDGEMENTS

Chapter 1

Introduction

The isolation of a mono-atomic layer of Carbon, termed graphene, in 2004 [3] opened the door to a new research field: the study of two-dimensional materials. It is remarkable in itself in a way that two dimensional crystals of large sizes cannot be grown in free space [2]. The trick of the Manchester research group was to take a three-dimensional crystal of graphite and extract a single layer out of it by mechanical exfoliation. While soon after their landmark discovery, the research group around Andre Geim and Kostya Novoselov published another work demonstrating the isolation of many different two-dimensional crystals [83], the initial focus of interest has been on graphene. Not only that this two-dimensional crystal was shown to exist and remain stable at all, but it additionally showed amazing and previously unprecedented properties.

Graphene was found to be a zero-gap semiconductor with its charge carriers (electrons and holes) following a linear energy dispersion, similar to photons, but with an effective "speed of light" of only around 1×10^6 m/s, 1/300 of the speed of light in vacuum [4]. The pioneering experiments further revealed a very high mobility of graphene's charge carriers, exceeding the one of Silicon by one order of magnitude (and being almost independent of charge carrier concentration and temperature) and an ambipolar field effect [3]. For their ground breaking experiments, Andre Geim and Kostya Novoselov were awarded the Nobel Prize in Physics in 2010.

As of late 2011, graphene remains in the centre of interest of fundamental research [14,53], industry [104-106] and even government [107]. This is not only due to its amazing optical and electronic transport properties, which with respect to microelectronics includes ballistic charge carrier transport [2] and optical transparency [12] and at the same time being highly conductive [97], but also from the fact that graphene possesses unexpected mechanical properties.

While one could possibly expect to break graphene easily, since it is only one atom thick, it instead turned out that graphene is the strongest material ever measured [9]. It can sustain strain up to 20% without breaking [9] and has a Young's modulus of ~1TPa, larger than steel having 200 GPa. First demonstrations of how these properties can be exploited on a large scale have been demonstrated by e.g. showing how graphene could reinforce polymers to a great extent [98], an application having massive impact in aerospace, construction and textile fabrication. Moreover, the resistance of graphene depends in a quite sensitive way to the amount of lattice deformation induced, which is very important in the area of strain sensors [99]. Another very interesting fact about graphene, on a more fundamental level, is that it might offer a straight-forward possibility to manipulate its native band structure, and thus could possibly alter its material properties altogether, by mechanically deforming its crystal lattice (often called "strain engineering) [45].

Looking at these fascinating mechanical properties and the possible implications, it is of great importance to exactly quantify and understand the response of graphene to mechanical deformations of its crystal lattice. The initial results on the breaking strength of graphene and its Young's modulus were obtained using a scanning probe microscope-base technique. Since this technique strongly relies on the condition of the usually atomically sharp tip, the results obtained have to be evaluated with this constraint in mind [9]. In the mentioned application of using graphene to reinforce composite materials, which should have a higher breaking strength, one desires to have a full understanding of graphene's intrinsic mechanical response, since these materials are thought to be used in areas where uncertainties in the mechanical properties can lead to extremely dangerous situations (aerospace, car manufacturing or building industry). Furthermore, when considering the use of graphene as a strain sensor (by measuring changes in its resistance upon deformation), one definitely has to have a calibration procedure. For this, the amount of mechanical deformation of graphene has to be quantified as exactly as possible. Last but not least, fundamental studies aiming at exploring changes in graphene's band structure through mechanical changes of the equilibrium crystal lattice will greatly benefit from a detailed understanding of the sensitivity of the material to external mechanical perturbations.

In order to answer these underlying questions about graphene's mechanical properties, we employed Raman spectroscopy experiments on specially prepared graphene crystals. Raman spectroscopy is a very sensitive technique allowing to quantify the amount of strain induced in a material [27,39,40,43]. Raman spectroscopy is an inelastic light scattering technique. On a microscopic level, it can be explained through the interactions of light incident on a crystal with the electrons and holes of the crystal and the crystals lattice vibrations (phonons). It is this relation which allows a quantification of lattice deformation, since the lattice vibrations of a deformed lattice differ from that of the unperturbed crystal. In the past, Raman spectroscopy has proven to be an invaluable tool in characterising the mechanical response of a variety of materials under mechanical strain like silicon in integrated circuits, carbon nanotubes and composites [100-102]. To allow for a well-defined application of strain, for both expanding and compressing graphene's crystal lattice, graphene crystals had to be prepared on special substrates. To finally be able to interpret our experimental results in a straight-forward way, a special technique, the so-called cantilever beam technique, has been chosen. This technique enables us to successfully apply the tensile and compressive stress to the graphene monolayers embedded in the polymer substrate. The studies for the determination of the various type of stress (tensile and compressive) intake by graphene is a key requirement for above mentioned applications.

Apart from graphene, recently other two-dimensional crystals reached the surface of scientific interest [103]. Common to all of them is the route of fabrication, namely taking a layered bulk three-dimensional crystal, and mechanically extracting a single plane out of it. A very interesting candidate is two-dimensional Boron nitride. Hexagonal bulk Boron nitride shares some structural similarity with graphite. It is composed of vertically stacked layers, with each layer being made of a honeycomb lattice, with alternating Boron and Nitrogen atoms [84,85]. As opposed to graphene, which is a zero-gap semiconductor, a single layer of Boron nitride is a strong insulator with a band gap of 5.9 eV [88]. Having a two-dimensional insulating crystal would open a fantastic playground when combining it with a two-dimensional conductor such as graphene. The resulting interaction between graphene and boron nitride planes would be used for tunnelling or coulomb drag studies [108].

It was the second main objective of the work presented, to successfully and reproducibly prepare and identify single layer boron nitride. These isolated monolayer boron nitride layers would be alternately stacked with graphene to make heterostrutures having properties different from both the boron nitride and graphene. Therefore graphene layers can be coupled depending on the number of the insulating boron nitride layers introduced in between the graphene layers.

The thesis is organized as follows. Chapter 2 provides an overview of graphene and a description of its electronic properties. Further, it is presented how to routinely fabricate and identify graphene. In Chapter 3, the experimental technique of Raman spectroscopy is described in detail and a theoretical explanation of the Raman scattering phenomena is given. The characteristic Raman spectrum of graphene and the results of Raman spectroscopy experiments on graphene are discussed here in detail. The findings of this chapter provide the basis for Chapter 4. After presenting a general review of the elastic properties of the graphene in Chapter 4, the results of Raman spectroscopy on graphene subjected to strain are presented and discussed. The compression behaviour of single layer graphene is presented in chapter 5 of the thesis. Method to prepare graphene on polymer (PMMA) substrate and their optical analysis is also described in detail. Further, Raman measurement of graphene under stress and the buckling strain analysis of the graphene flakes of different geometries is also presented. Chapter six of the thesis deals with the two dimensional insulator Boron nitride. Preparation of the large boron nitride flakes using mechanical cleavage is discussed and the results of optical and Raman spectroscopy analysis are presented. The applications of the two dimensional insulator boron nitride in graphene based electronics are also briefly discussed. The work presented in the thesis is summarized in chapter 7. In this chapter I will give the conclusions of the thesis and an outlook of the future work based on the findings given in this thesis.

The work presented in Chapter five and six has been published and in order for better presentation of the results the original papers are attached in each of these chapters.

Chapter 2

Two Dimensional form of Carbon: Graphene

This chapter of the thesis deals with recently discovered material graphene. Graphene has been extensively studied since it was first isolated from the bulk graphite in 2004. In order to understand this new material the study of its electronic band structure is necessary and is described here. The properties of graphene and its potential in future applications is also discussed. Method for graphene preparation and its characterization using optical microscopy, atomic force microscopy and Raman spectroscopy are presented in this chapter.

2.1 Introduction

The three dimensional (3D) allotropes of Carbon, diamond, graphite and amorphous carbon are well known materials since ages. Few years ago Fullerenes (Bucky balls) and carbon nanotubes, the zero- dimensional and one dimensional forms of carbon have been discovered [1]. Graphene is the name given to a two dimensional (2D) sheet of carbon atoms arranged in a hexagonal lattice. It can be considered the fundamental building block of all other carbon materials: (graphite (3D): stacked graphene layers, Carbon nanotubes (1D): rolled graphene layer, Bucky balls (0 D): Wrapped graphene layers) [2]. The crystal structure of 3D graphite is shown in Fig. 2.1.

Graphite structure
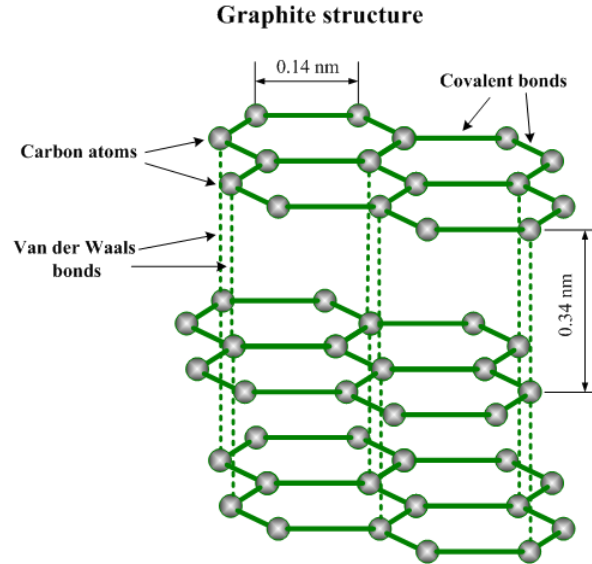
Figure 2.1: Arrangement of in-plane covalently bonded carbon atoms (NN distance 1.42 Å) in a graphite crystal. The graphene layers themselves are weakly bonded to each other by Van der Waals forces (interlayer spacing 3.35 Å).
(Image taken from http://www.substech.com/dokuwiki/doku.php?id=graphite_as_solid_lubricant)

Since it is only one atom thick, the two dimensional material graphene was thought not to exist in the free state and it was considered to be thermodynamically unstable [2]. Therefore, one atom thick crystals were considered only as an essential part of 3D structures. Until the truly two dimensional material graphene was discovered in 2004 [3]. Two dimensional graphite i.e graphene has been theoretically studied for more than sixty years as a model for carbon material [5]. Earlier attempts to obtain free standing 2D atomic crystals from layered materials by separating/isolating the atomic layers only resulted in nanometre sized crystallites [2]. In 2004 at the University of Manchester, the first ever free standing two dimensional crystals, graphene was isolated [3]. Instead of trying to grow 2D crystals they extract a single layer out of an already existent 3D structure. In the same manner they were able to demonstrate that any number of the layers crystal can be mechanically peeled from a bulk graphite. The present interest in graphene has arisen by unprecedented experiments on isolated single, bi and few layer graphene crystals revealing and exploiting the graphene's unusual band structure. Due to graphene's exceptional properties its use is highly anticipated by lots of commercial areas like microelectronics, optoelectronics, material engineering. The charge carriers in graphene can be described as massless Dirac fermions [4] governed by the

26

Dirac equation. Therefore further it provides an alternate to study fundamental phenomena of quantum electrodynamics in solid state structures.

2.2 Graphene Unique Properties and Applications

As graphene was first material discovered in the new class of two dimensional materials. It has been extensively studied from the very beginning. It shows remarkable electronic, optical and mechanical properties due to the particular arrangement of carbon atoms in a honeycomb lattice and the resulting electronic band structure [1, 6, 7]. These exceptional properties of graphene make its room for upcoming applications.

The unusual electronic properties of graphene arising because of its electronic band structure such as ambipolar field effect and ballistic charge carrier transport over sub-micron distances at room temperature make it extremely interesting for future electronic devices [1, 2]. The charge carriers concentration can be tuned by applying an electric field reaching concentrations up to 10^{13} cm^{-2} [3]. The high crystalline quality of graphene's lattice gives rise to high electrical conductivity of charge carriers [4] with mobilities ~ 20,000 cm^2/Vs at room temperature and are routinely obtained on Si/SiO$_2$ substrates. However a hurdle in the use of graphene in electronic applications is the switching of electronic devices due to significant conductivity σ_{min} even at neutrality point [2] but high frequency graphene transistors are not much affected by this problem and have already been reported [8].

Graphene mechanical properties are not less outstanding. It is the strongest material measured so far, about 200 times stronger than steel [9]. Graphene has a Young's modulus of 1.0 TPa and a fracture strength of 130GPa [9]. These exceptional qualities can be employed in various applications such as reinforcing the polymer nanocomposite materials, in which graphene can be used as a nanofiller with the polymer matrix [10, 11]. The field of strain engineering is the second area of application where strain is applied to obtain the improved and desired properties of the material [28]. Because of its high elasticity without fracturing, strain can be applied to tune the graphene's properties over a wide range.

The study of the optical properties of graphene shows that it absorbs only $\pi\alpha \approx 2.3\%$ of white light, where α is the fine structure constant [12]. Due to this high transparency it has a large potential for applications as transparent conductive electrodes, may be eventually replacing the presently dominating ITO electrodes.

27

The chemical functionalization of graphene [13, 14] is another major area where novel findings were reported and are expected to occur. It has already been demonstrated that new materials can be synthesized from the graphene using chemical treatments (hydrogenated graphene [13] and fluorographene [14]) which themselves show new and remarkable properties.

2.3 Band structure of Graphene

2.3.1 Crystal Structure

To start with we will first examine graphene's structure, closely following Ref. [15]. A carbon atom has four valence electrons. Each carbon atom in the lattice structure of graphene has one s and three p orbitals for bonding (σ and π). Within the graphene sheet, the s orbital and two in-plane p orbitals generate three SP^2 orbitals forming strong covalent (σ) bonds with their three neighbouring carbon atoms as shown in Fig. 2.2 . The nearest neighbouring distance between these atoms within the plane is 1.42 Å. Whereas the fourth valence electron occupies a p_z

Figure 2.2: The SP^2 hybridization of carbon atoms with one S and two in-plane P orbitals in the honeycomb lattice structure of graphene.
(Image taken from http://courses.cit.cornell.edu/ece407/Lectures/handout11.pdf)

orbital perpendicular to the sheet and is leftover. It contributes to the delocalized electron gas which explains graphene's high conductivity. Each carbon atom contributes an electron to the P_z orbital to form a π band along z-direction. So in total graphene has three in plane σ orbitals which are responsible for the strength of graphene and a P_z - band perpendicular to the sheet of graphene.

Graphene's honeycomb lattice structure is not a Bravais lattice; it rather consists of two interpenetrating triangular lattices. It can well be described by attaching a two atom basis (blue and red) to the hexagonal point lattice. This is shown in Fig. 2.3.

Figure 2.3: A 2D honeycomb is formed by placing a two atom basis (blue and red) to each point on hexagonal lattice [16].

To understand why graphene shows extraordinary behaviour it is useful to look at its theoretical description. In the following we will denote one sublattice corresponding to one of the two basis atoms as A and the other sublattice as B. Any lattice point of the respective sublattice can be reached from a chosen origin by the lattice translation vector [16] as:

$$\mathbf{R} = n_1\mathbf{a_1} + n_2\mathbf{a_2} \tag{2.1}$$

Where $\mathbf{a_1}$ and $\mathbf{a_2}$ are the lattice vectors of the respective sublattice, n_1 and n_2 are the integers.

The primitive lattice vectors $\mathbf{a_i}$ join atoms on the same sublattice (A or B), in a way that the reference points of the unit cells (the A-atoms in Fig. 2.4 (b)) form a triangular lattice [17]. So the hexagonal carbon lattice can be broken down into more primitive triangular sublattices A and B that are identical. A carbon atom on the A sublattice is at the centre of a triangle formed by three atoms from the B sublattice, and vice versa [18].
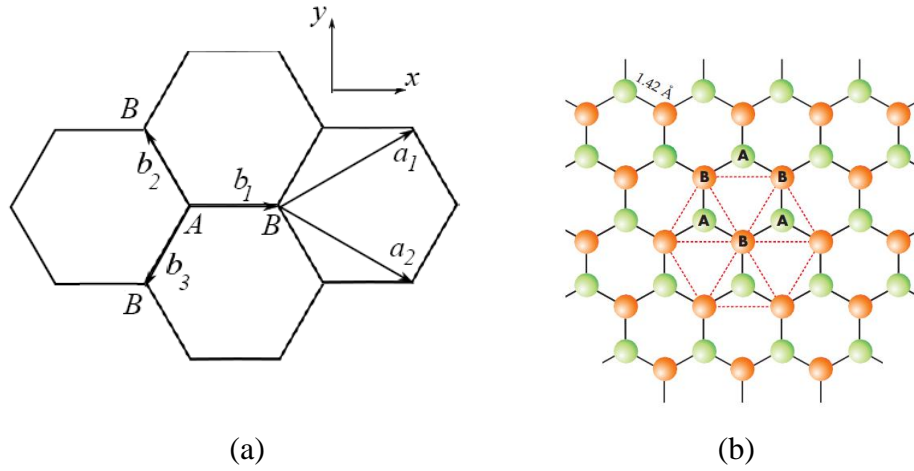
Figure 2.4: (a) Honeycomb lattice structure of graphene with carbon atoms A and B belonging to the two sublattices having a_1 and a_2 as lattice unit vectors $\mathbf{b_i}$, i=1,2,3 are the nearest neighbor vectors [17]. (b) Illustration of the two interpenetrating triangular sublattices. The position of sublattice (green) is at the centre of the triangle (red) formed by other sublattice (orange) [18].

The lattice vectors shown in Fig. 2.4 (a) can be represented as [6]:

$$\mathbf{a_1}=a\left(\frac{3}{2},\frac{\sqrt{3}}{2}\right) \quad \text{and} \quad \mathbf{a_2}=a\left(\frac{3}{2},-\frac{\sqrt{3}}{2}\right) \tag{2.2}$$

with $a \approx 1.42$ Å being the nearest neighbour distance between two carbon in the honeycomb lattice. The nearest neighbouring carbon atoms can be reached from any given carbon atom and given by the vectors:

$$\mathbf{b_1}=a\left(1,0\right), \quad \mathbf{b_2}=a\left(-\frac{1}{2},\frac{\sqrt{3}}{2}\right) \text{ and } \mathbf{b_3}=a\left(-\frac{1}{2},-\frac{\sqrt{3}}{2}\right) \tag{2.3}$$

To come to a theoretical description of the graphene's band structure which enable us to explain its electronic properties, we have to consider the reciprocal lattice of graphene. The reciprocal lattice vectors $\mathbf{c_i}$ can be determined from the direct lattice vector using the relation,

$$\mathbf{c_i}. \mathbf{a_j} = 2\pi\delta_{ij} \tag{2.4}$$

where δ_{ij} is the Kronecker delta with $\delta_{ij}=1$ for $i=j$ and $\delta_{ij}=0$ for $i \neq j$

The reciprocal lattice is again a honeycomb lattice, but rotated under 90 degrees with respect to the real lattice. The reciprocal lattice vectors are given by:

$$\mathbf{c_1}=\frac{2\pi}{a}\left(\frac{1}{3},\frac{1}{\sqrt{3}}\right) \quad \text{and} \quad \mathbf{c_2}=\frac{2\pi}{a}\left(\frac{1}{3},-\frac{1}{\sqrt{3}}\right) \tag{2.5}$$

The Brillouin zone (primitive unit cell of the reciprocal lattice) of a honeycomb lattice structure is a hexagon as shown in Fig. 2.5.

(a)   (b)
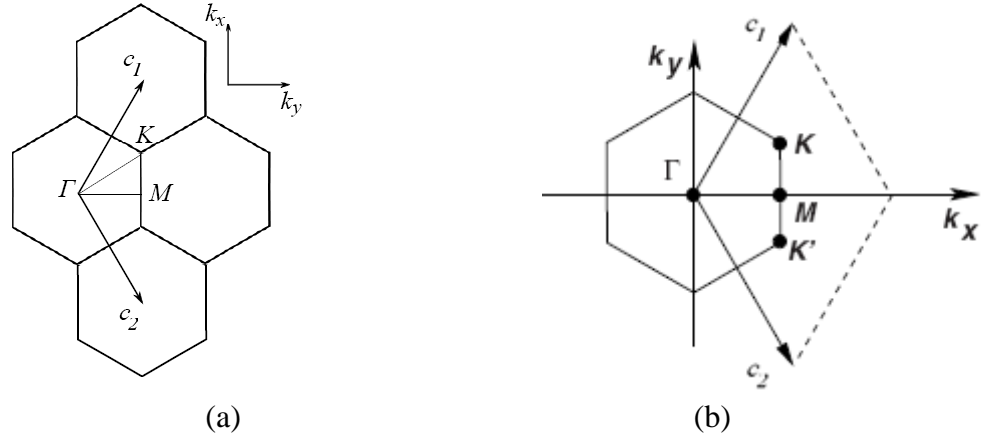
Figure 2.5: (a) Hexagonal Brillouin zone of graphene with reciprocal lattice vectors c_1 and c_2 [17]. (b) The graphene's hexagonal brillouin zone with Γ as centre and point K and K' as corners of the brillouin zone [6].

The center of the Brillouin zone is conventionally labelled Γ. Because the honey lattice consists of to sublattices ,there are two non equivalent parts in the reciprocal space named K and K'. The position of K and K' in reciprocal (or momentum) space is given by:

$$\mathbf{K}=\frac{2\pi}{a}\left(\frac{1}{3},\frac{1}{3\sqrt{3}}\right) \quad \text{and} \quad \mathbf{K'}=\frac{2\pi}{a}\left(\frac{1}{3},-\frac{1}{3\sqrt{3}}\right) \tag{2.6}$$

2.3.2 Band Structure

The electronic band structure of graphene can be described quite well by simple tight binding approximation for the π electrons [5,20,21]. The tight binding model presented below follows Ref. [22]. For this purpose we are solving the time independent Schrödinger equation for the π electrons of the graphene crystal.

$$H\psi = \mathrm{E}\psi \tag{2.7}$$

Where ψ is the wavefunction of one of π electron in the crystal lattice. Hence it must fulfil the Bloch's theorem.

$$\psi(r+R)=e^{ik.R}\psi(r), \tag{2.8}$$

31

A weighted linear combination of the wave functions of the electrons of the A and B sublattices is taken as:

$$\psi(k,r) = C_A \phi_A(k,r) + C_B \phi_B(k,r) \tag{2.9}$$

The subscript A and B are the two different sublattices. The functions ϕ_A and ϕ_B are the so called Bloch function. They are taken here to be taken the linear combination of the atomic orbitals or wavefunctions as:

$$\phi_A(k,r) = \frac{1}{\sqrt{N}} \sum_J^N e^{ik.R_{Aj}} \varphi(r - R_{Aj}) \tag{2.10}$$

$$\phi_B(k,r) = \frac{1}{\sqrt{N}} \sum_J^N e^{ik.R_{Bj}} \varphi(r - R_{Bj}) \tag{2.11}$$

Where N is the number of unit cells in the lattice and R_A (R_B) are the lattice vectors for all A (B) atoms in graphene lattice.

Substituting eq. (2.9) into the Schrödinger equation given by eq. (2.7) and solving for the energy bands of graphene,

$$C_A H \phi_A(k,r) + C_B H \phi_B(k,r) = E(k) C_A \phi_A(k,r) + E(k) C_B \phi_B(k,r) \tag{2.12}$$

Multiplying by the complex conjugate of ϕ_A , and separately by the complex conjugate of ϕ_B, generates two separate equations. Integration of both equations over the entire volume of the crystal Ω produces,

$$C_A \int_\Omega \phi_A^* H \phi_A dr + C_B \int_\Omega \phi_A^* H \phi_B dr = EC_A \int_\Omega \phi_A^* \phi_A dr + EC_B \int_\Omega \phi_A^* \phi_B dr$$

$$C_A \int_\Omega \phi_B^* H \phi_A dr + C_B \int_\Omega \phi_B^* H \phi_B dr = EC_A \int_\Omega \phi_B^* \phi_A dr + EC_B \int_\Omega \phi_B^* \phi_B dr \tag{2.13}$$

Using the following symbolic definitions to make the equations simpler:

$$H_{ij} = \int_\Omega \phi_i^* H \phi_j dr, \qquad S_{ij} = \int_\Omega \phi_i^* \phi_j dr, \tag{2.14}$$

Where H_{ij} are the matrix element of the Hamiltonian or transfer integral and have the units of energy. S_{ij} are the overlap matrices between Bloch functions and are unitless.

Simplifying the matrix elements by considering that the overlap between all A-type atoms must be same as overlap between all B-type atoms i.e, $S_{AA}=S_{BB}$ and $H_{AA}=H_{BB}$ and using the condition $H_{BA}=H_{AB}{}^*$ and $S_{BA}=S_{AB}{}^*$,

$$C_A(H_{AA} - ES_{AA}) = C_B(ES_{AB} - H_{AB}) \tag{2.15}$$

$$C_A(H^*_{AB} - ES^*_{AB}) = C_B(ES_{AA} - H_{AA}) \tag{2.16}$$

Solving the eq. (2.16) for C_B and substituting in eq. (2.15) gives a quadratic equation and its solution gives the energy:

$$E(k)^{\pm} = \frac{E_0(k) \pm \sqrt{E_0(k)^2 - 4(S_{AA}(k)^2 - |S_{AB}(k)|^2)(H_{AA}(k)^2 - |H_{AB}(k)|^2)}}{2(S_{AA}(k)^2 - |S_{AB}(k)|^2)} \tag{2.17}$$

With

$$E_0(k) = \left(2H_{AA}(k)S_{AA}(k) - S_{AB}(k)H^*_{AB}(k) - H_{AB}(k)S^*_{AB}(k)\right) \tag{2.18}$$

Positive and negative energy branches in eq. (2.17) are called conduction (π^*) and valence (π) bands respectively.

The following assumptions and their mathematical results are considered here to develop the final band structure equation.

Taking into account the Nearest Neighbor Tight-Binding (NNTB) model, the wavefunction of an electron in any primitive unit cell overlaps only with the wavefuntions of nearest neighbors. In Fig. 2.4 (a) the nearest neighbor of atom A in the graphene lattice are three B atoms so the P_z wavefunction of the A atom overlaps with the P_z wavefunction of three nearest neighbor B atoms and does not overlap with the wavefunction from farther atoms, so the eq.(2.17) simplifies as the Hamiltonian matrix reduces to:

$$H_{AA}(k) = \int_{\Omega} \phi^*_A H \phi_A dr = \frac{1}{N} \sum_j^N \sum_l^N e^{-ik.R_{Aj}} e^{ik.R_{Al}} \times \int_{\Omega} \phi^*(r - R_{Aj})H\phi(r - R_{Al})dr \tag{2.19}$$

$$H_{AA} = \frac{1}{N} \sum_j^N \sum_l^N e^{ik.(R_{Al} - R_{Aj})} E_{2p}\delta_{jl} = E_{2p}, \tag{2.20}$$

Where the δ_{jl} is the Kronecker delta function and constant E_{2p} is close to the energy of the 2p orbital in isolated carbon. Similarly the overlap matrix reduces to

$$S_{AA}(k) = \int_{\Omega} \phi^*_A \phi_A dr = \frac{1}{N} \sum_j^N \sum_l^N e^{-ik.R_{Aj}} e^{ik.R_{Al}} \times \int^{\Omega} \phi^*(r - R_{Aj})\phi(r - R_{Al})dr \tag{2.21}$$

$$S_{AA}(k) = \frac{1}{N} \sum_j^N \sum_l^N e^{ik.(R_{Al} - R_{Aj})}\delta_{jl} = 1, \tag{2.22}$$

Where we have taken advantage of the normalized feature of the Wannier functions which is the Fourier transform of the Bloch function taken as $\int \phi^*(r - R_j)\phi(r - R_j)dr = 1$

For the energies close to the Fermi energy E_F, the π and π^* branches of the ab-initio band structure of graphene shows a similar structure. Therefore the energy branches are mirror image of each other within this restricted range, since electrons are the charge carriers in the π^* band and holes are the charge carriers in the π band. This approximation called the electron-hole symmetry is used here to further proceed with the band structure calculations. This approximation is useful as in practical devices the electron dynamics occur over a small range of energies close to the Fermi energy. Closely following the details of ref. [22] that uses this approximation, we proceeds with these calculations. Mathematically, electron-hole symmetry forces S_{AB} (k) $=0$ as can be seen in eq. (2.17); the only part that possesses symmetry about some number is the plus/minus square root term. In order to retain symmetry in eq. (2.17), $S_{AB}(k)$ must vanish to zero. Therefore

$$E(k)^{\pm} = E_{2p} \pm \sqrt{H_{AB}(k)H_{AB}^{*}(k)}, \tag{2.23}$$

Which is the energy dispersion originally proposed by Wallace [12] in 1947. In order to simplify further setting $E_{2p} =0$. This is because energy is defined to within an arbitrary reference potential and in graphene the reference potential is the Fermi energy (independent of k) and is set to 0 eV. Only parameter independent of k in equation (2.23) is E_{2p}, therefore it is convenient to take it as the reference and hence $E_{2p} = E_F = 0eV$

$$E(k)^{\pm} = \pm\sqrt{H_{AB}(k)H_{AB}^{*}(k)} \tag{2.24}$$

The Hamiltonian matrix element H_{AB} (k) can be calculated as,

$$H_{AB}(k) = \int_{\Omega} \phi_A^* H \phi_B dr = \frac{1}{N} \sum_{j}^{N} \sum_{l}^{N} e^{-ik.(R_{Aj}-R_{B_l})} \times \int_{\Omega} \phi^*(r - R_{Aj}) H \phi(r - R_{B_l}) dr \tag{2.25}$$

Defining the nearest neighbor distances between a type-A and its three type-B atoms,
$R_1 = R_{Aj} - R_{Bj}$, $R_2 = R_{Aj} - R_{Bj+1}$, $R_3= R_{Aj} - R_{Bj-1}$ where j, j+1, j-1 are the indices of the primitive unit cells as the nearest neighbor distances.

$$H_{AB}(k) = \frac{1}{N} \sum_{j}^{N} \sum_{m=1}^{3} e^{-ik.R_m} E_m \tag{2.26}$$

Where E_m is the finite value of the nearest neighbor functions. By necessity $E_1=E_2=E_3$, because the integral are radially dependent and the nearest neighbor distances are radially symmetric. Taking Em $= \gamma$ as the nearest neigbor overlap energy (sometimes called hopping or transfer energy).

The following expression for the energy dispersion is obtained after substituting the values of $H_{AB}(k)$ and $H^*_{AB}(k)$,

$$E(k)^{\pm} = \pm\gamma\sqrt{1 + 4\cos\frac{\sqrt{3}a}{2}k_x \cos\frac{a}{2}k_y + 4\cos^2\frac{a}{2}k_y} \qquad \textbf{(2.27)}$$

The value of γ commonly ranges from about 2.7 eV- 3.3 eV [22]. The minus and plus sign corresponds to the valence and conduction bands. Therefore

$$E(k) = \gamma f(k) \qquad \textbf{(2.28)}$$

Where $\qquad f(k) = \sqrt{1 + 4\cos\frac{\sqrt{3}a}{2}k_x \cos\frac{a}{2}k_y + 4\cos^2\frac{a}{2}k_y} \qquad \textbf{(2.29)}$

The two energy bands of graphene derived here under the assumption of zero overlap between two sublattices $(S_{AB}=0)$ are shown in Fig. 2.6 (a).
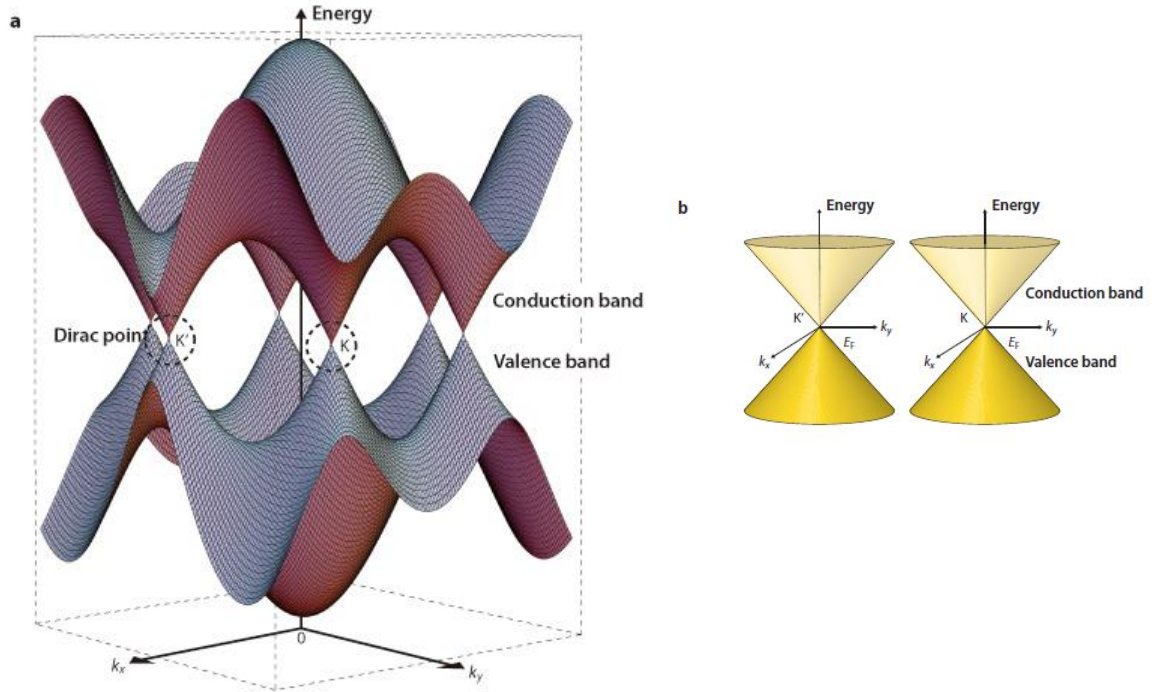
Figure 2.6: (a) Graphene energy bands near Fermi level. The valence and conduction bands meet at the K and K′ points in the Brillouin zone. (b) Conical energy bands near K and K′ points [23].

The electronic bands touch at the six corners of the brillouin zone forming cones of charge carriers (holes and electrons) at each corner [7]. The points where these cones touch are called "Dirac points" and are characterized by **K** and **K′** momentum vectors as represented in Fig. 2.6 (a). Therefore graphene is a gapless semiconductor or semi-metal [7].

In graphene the low energy excitations near **K** and **K´** play an important role and energy dispersion relation around these points is given by:

$$E(\text{k})^{\pm}_{linear} = \pm\hbar v_F |\text{k}|$$ (2.30)

Here k is the momentum taken at point K or K´, $\hbar = h/2\pi$ and v_F is the Fermi velocity. The above linear relation is expressed in Fig. 2.6 (b).

The linear dispersion of graphene charge particles can be related to the relativistic particle behaviour in physics. The energy dispersion of a relativistic particle is given by the Dirac equation:

$$E = \pm\sqrt{c^2\hbar^2 k^2 + m^2 c^4}$$ (2.31)

Setting mass to zero in the above equation, the following equation can be obtained:

$$E = \pm c\hbar|k|$$ (2.32)

This is the similar equation as obtained in the low energy dispersion for graphene in eq. (2.30). In graphene the Fermi velocity v_F takes the role velocity of light c.

So the graphene quasiparticles obey E= |ℏ k|v_F Dirac like linear dispersion with the Fermi velocity v_F ~ c/300. The velocity of these charge carriers is found to be as high as 1×10^6 m/s at the Dirac point .Therefore the charge particles are described by a relativistic Dirac equation rather than a conventional non-relativistic Schrodinger equation with an effective mass [2]. The linear energy dispersion (unlike other materials) is responsible for the high conductivity of graphene and term "massless Dirac fermions" for its carriers [2].

2.4 Density of States (DOS)

The density of states (DOS) g(E) describes how many states per unit energy interval can be occupied by the electrons or holes respectively. The total number of states available between an energy E and E_+ for a two dimensional material is given by dividing the differential area dA in k-space by the area of the k-space. Mathematically

$$g(E)dE = 2g_z \frac{dA}{(2\pi)^2/\Omega}$$ (2.33)

The factor 2 in the numerator accounts for the spin degeneracy and g_z is the zone degeneracy. Ω is the area of the lattice and dA is the infinitesimal area element in the k-space.

For six equivalent k-points in graphene each k-point is shared by three hexagons therefore g_z =2. A circle of constant energy in k-space is considered to find dA. Taking $2\pi k$ and $2\pi k dk$ as the perimeter and the differential area dA of the circle the DOS becomes,

$$g(E) = \frac{2}{\pi}\left|k\frac{dk}{dE}\right| = \frac{2}{\pi}\left|k\left(\frac{dE}{dk}\right)^{-1}\right|$$

(2.34)

Where g (E) has been normalized to the Ω.

Using eq. (2.30) yields the following linear DOS relation,

$$g(E) = \frac{2}{\pi(\hbar v_F)^2}|E| = \beta_g|E|$$

(2.35)

The important dependence is the linear dependence of the DOS on the energy. This situation is shown in Fig. 2.7.The DOS becomes zero at the Fermi energy E_F =0. This is the reason why graphene is considered as zero-gap semiconductor.
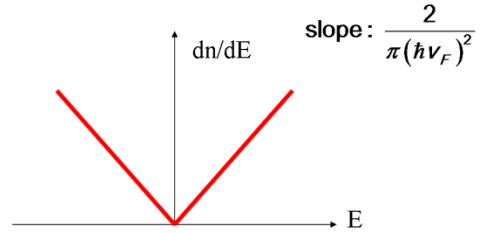
Figure 2.7: Density of states near the Fermi level of graphene.

2.5 Graphene Fabrication by Mechanical Cleavage

The pioneering technique for isolating graphene was micromechanical cleavage, as demonstrated by Novoselov et al. in 2004 at the University of Manchester [3]. Still to date (2011) proves to provide the highest quality graphene crystals [3, 4]. While after the initial discovery other methods of graphene fabrication have also been reported [10, 24] such as chemical exfoliation of graphite, epitaxial growth by chemical vapour deposition of hydrocarbon or by thermal decomposition of silicon carbide. The samples examined in this thesis were obtained by micromechanical cleavage. Micromechanical cleavage consists of repeatedly thinning down a crystal and eventually transferring the thinnest pieces onto a substrate for further inspection. The process can be depicted as the scheme below in Fig. 2.8. This technique is highly reproducible and it can be used to make graphene by using this

method graphene can be made on various substrates like Si/SiO$_2$, PMMA, mica, glass and quartz.

In details explained below, the fabrication process of graphene using mechanical cleavage is given and it consists of three steps:

• Pre-cleaning of substrate

• Mechanical cleavage of graphite

• Identification of graphene on the substrate
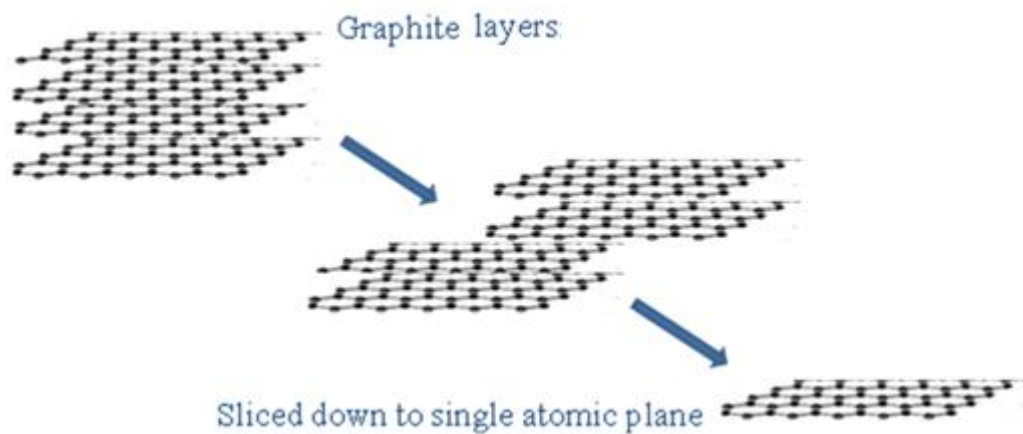
Figure 2.8: Extracting of Single layer from Graphite by micromechanical Cleavage.

Pre-cleaning of substrate

The standard size (21 * 25 mm^2) Si/SiO$_2$ substrate is used to prepare the graphene flakes. To improve the adherence of graphene to the substrate and to minimize contamination, the substrate needs to be pre-cleaned before mechanical cleavage and deposition of graphite. The pre-cleaning consists of two sequential steps, standard solvent cleaning followed by oxygen plasma cleaning. The procedure below describes the different steps during solvent cleaning:

- Substrate is put into a beaker with acetone.
- Beaker (acetone + sample) is placed in an ultrasonic bath (10 mins).
- Substrate is transferred into a beaker with deionised water to dissolve the acetone using ultrasonic bath (2 mins).
- Sample is put into a beaker with isopropanol to dissolve the water.
- Beaker (isopropanol + sample) is put into ultrasonic bath (10 mins).
- Then the sample is blow dried completely with nitrogen.

The substrate is then treated for 5-10min in an oxygen: argon plasma in 1:2 ratio to remove the remaining organic contamination from the surface of the substrate.

Mechanical Cleavage of Graphite

In the second step, a piece of natural graphite is first pressed on adhesive tape and repeatedly cleaved to obtain the thin graphite layers (planes). The tape with thin graphite is then pressed to the surface of pre-cleaned oxidized silicon substrate, afterwards the tape is removed. There are two ways to remove the tape, either it is peeled off gently using tweezers or solvent is used to dissolve the tape. The sample (substrate + graphite) needs to be cleaned again with solvents to remove the contamination coming from the tape. Sample is then baked at elevated temperature to get rid of any water content. Finally a fresh adhesive tape is used to peel off thick graphite layers on substrate to obtain graphene. The process is illustrated in Fig. 2.9 along with the graphene flakes obtained. The size of the resulting flake is affected by a number of factors such as the size of the initial graphite crystal and the substrate cleaning procedure. The method described above can be used to produce large size (~millimetre) graphene flakes on different substrates.
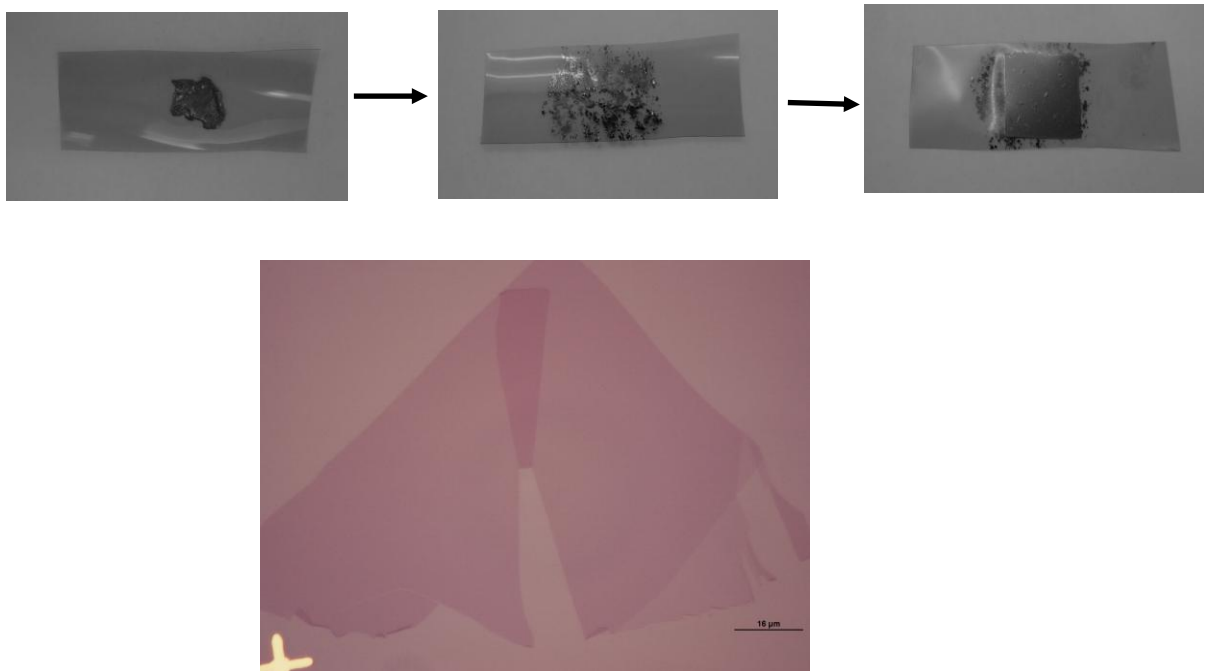
Figure 2.9: Step by step procedure of micromechanical cleavage of graphite (top) and optical images for graphene on 300 nm Si/SiO$_2$ obtained by this procedure(bottom).

39

2.6 Identification of graphene

To identify single-layer, bi-layer or multilayer graphene flakes on a given substrate, we use techniques of optical microscopy, Raman spectroscopy and Atomic force microscopy (AFM). In most cases, Raman spectroscopy and AFM were used to determine the thickness of a particular graphene flake found by optical microscopy. For experimental research, optical microscopy is the quick method to identify single layer graphene from the exfoliated graphite flakes on substrate. Raman and AFM are also performed to determine the single layer nature of a given graphene flake.

2.6.1 Optical Microscopy

Thin graphene flakes can be easily detected on an oxidized silicon substrate because the flakes add an additional optical path for the light reflected off the substrate surface [25]. Typically, the colour for a 300 nm SiO_2 wafer is violet-blue and the extra thickness due to graphitic flakes shifts it to blue. A change of few nanometres thickness in the oxide layer may result in suppressing of the visibility of graphene In general, the optical contrast of single layer graphene depends very sensitively on the oxide thickness of the underlying substrate [25].
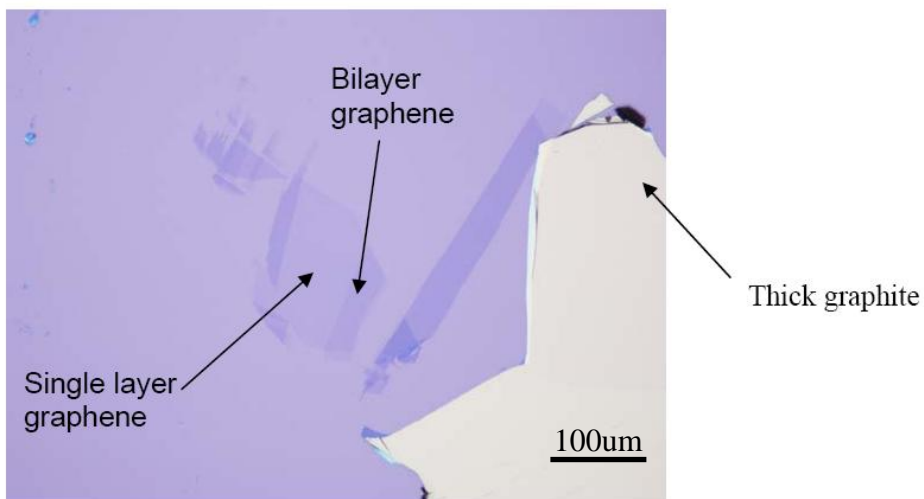
Figure 2.10: Optical images for single, Bi-layer and few-layer graphene on 285nm Si/SiO_2.

Fig. 2.10 shows an image of a graphene flake obtained by mechanical cleavage on 300 nm Si/SiO_2 wafer. To obtain a better contrast optical filters can be applied in the optical

microscope. Figure 2.11 illustrates the typical improvement in image quality with the optical filters in microscope.
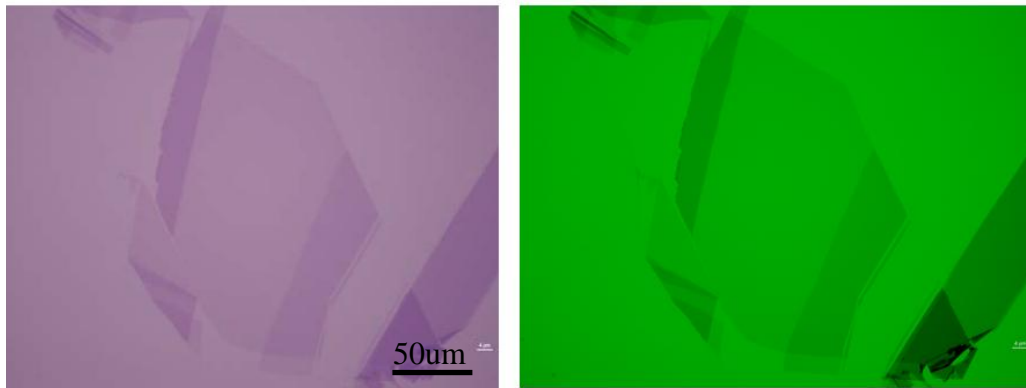
a) Without optical Filter   **b)** using a 560 nm optical filter

Figure 2.11: Improvement in the optical contrast of graphene flakes using optical filter.

2.6.2 Atomic force microscopy

For determining the thickness of the cleaved graphite crystallites showing the faintest contrast in optical microscopy, atomic force microscopy (AFM) seems to be the natural choice. In AFM, a sharp probe tip, mounted to a bendable cantilever, is raster-scanned across the surface of the sample. This scanning motion is facilitated by piezoelectric elements. When the tip is brought into close vertical vicinity of the surface, then during the lateral scanning various interactions between tip and surface can cause the cantilever to bend. A common way to record this bending is given by laser deflection, in which a laser is deflected off the backside of the cantilever onto a position sensitive four quadrant photodiode.

For obtaining an image of the sample surface, the vertical distance between the probe tip and the sample surface is permanently adjusted in order to keep the interaction between tip and sample surface constant. If variations in the tip-sample interaction cause a change in the bending of the cantilever, an error signal is calculated (using a feedback-loop circuit) from the difference between the user-defined and the actual value of the laser deflection. This error signal is then applied to the z-piezo, which controls movement of the tip perpendicular to the sample surface, to adjust the tip-sample distance such that the user-defined laser deflection is being kept constant. If one monitors the error signal at each point of the two-dimensional

raster mesh (parallel to the surface), one obtains a two-dimensional image of constant tip-sample interaction. Commonly, this image is interpreted as the height of the sample surface.

The most common operating schemes of an AFM are contact mode (static) and Tapping Mode (dynamic). In the static mode of operation, the tip is pressed against the surface under a user-defined force and repulsive forces constitute the main interaction between tip and sample. However, the friction that tip experiences when being scanned across the sample surface (causing a lateral deflection of the cantilever) might lead to artefacts in the height image (which is recorded according to changes in the vertical deflection of the cantilever). In the dynamic mode, the tip is forced to oscillate continuously, at a frequency close to its resonance frequency. This oscillation is further characterized by its amplitude and phase. If the interaction between tip and sample changes, the parameters of the cantilever's oscillation change accordingly. In most commercially available instruments, the change of the oscillation amplitude is monitored. The vertical tip-sample distance is then adjusted, as described above, in order to keep the oscillation amplitude of the tip constant. Because of its permanent oscillation, the tip only touches the sample point-wise. This eliminates the influence of frictional forces and provides thus a better resolution. Tapping Mode AFM imaging was used exclusively for the AFM data presented in this thesis.

Because of using piezoelectric elements to raster-scan the sample parallel and perpendicular to its surface, the positioning accuracy[1] of the tip relative to the sample (both parallel and perpendicular to the sample) is in the sub-nm range. If the thinnest graphite crystals identified would consist of only a single atom thick graphene layer, a step height of around 3.34 Å between the underlying silicon oxide surface and the graphene flake is expected to be measured. This is within the accuracy of the AFM used.

In Fig.2.12 the AFM image of graphene layers on 300 nm Si/SiO2 is shown. The inset of the Fig. 2.12 is the AFM image of a bilayer and single layer graphene and the corresponding line profiles, the height of the graphene layer from the bilayer graphene is about ~3.3 Å.

Thus, while AFM does allow distinguishing single from few layer graphene crystals, it carries the risk of being ambiguous. Additionally, its throughput, in terms of the time required to take an image, is too low to be routinely used for single layer identification.

---

[1] The resolution in the direction perpendicular to the sample surface for a typical AFM used (DI Multimode with Nanoscope IIIa controller) is given as 0.3 – 1 Å by the manufacturer [95].
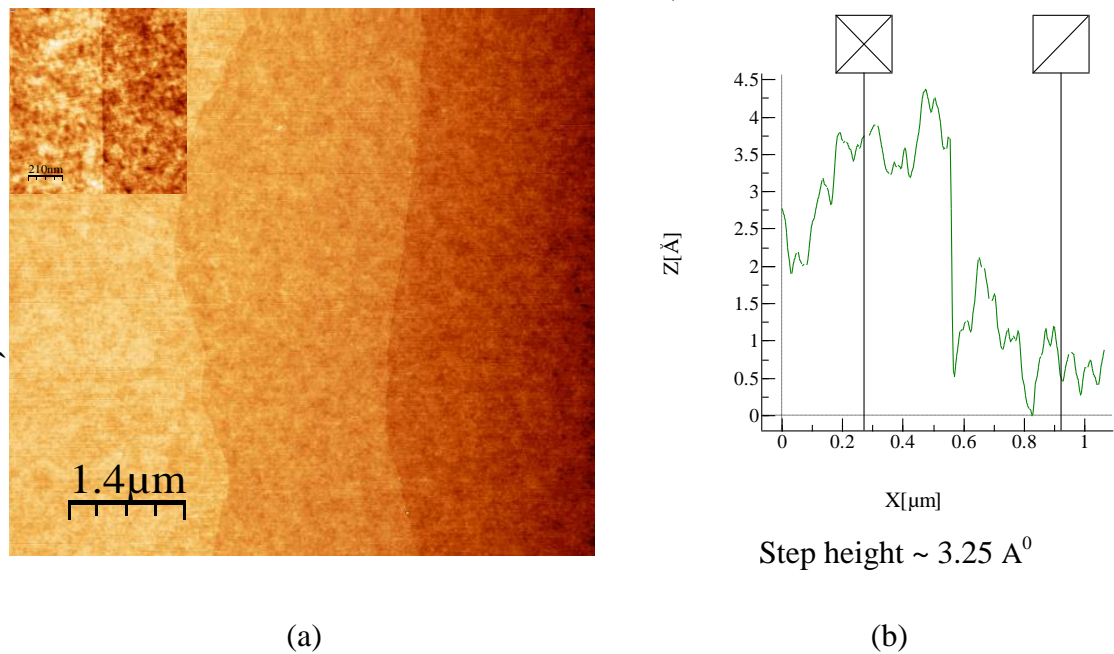
Figure 2.12: (a) AFM image of graphene layers on 300 nm Si/SiO$_2$. The inset of the image shows the step from bilayer to single layer (b) The height profile of the bilayer graphene to single layer graphene ~ 3.25 A^0 is shown.

2.6.3 Raman Spectroscopy

Raman study of single layer, bi-layer and multilayer graphene has been reported for the first time in 2006 [26]. This method provides us with reliable information about the number of graphene layers and is an extensively used technique for quick and unambiguous identification of the graphene layers. The Raman spectra of graphite and graphene using 514 nm excitation wavelength is shown in Fig. 2. 13 (a). The prominent peaks observed in the Raman spectra of graphite, few layers and single layer graphene (SLG) are : G peak at 1580 cm^{-1} and 2D peak (G′ peak) at 2700 cm $^{-1}$. The intensity of the G line changes with the number of graphene layers. G peak position is another important parameter which is sensitive to doping [26] and strain [27] . 2D peak conventionally called G′ peak which appears near 2700cm^{-1} in the Raman spectra of graphite and graphene layers and is used to find the number of graphene layers. 2D peak of bulk graphite is a split peak with intensity much less than the G peak whereas the single layer graphene has a single sharp peak with large intensity than the G peak. The single layer graphene 2D peak is a single Lorentzian but the bilayer graphene cannot be a single Lorentzian rather it can be described by a multiple Lorentzian line shape.

43

Also the full width half maximum (FWHM) of 2D peak for single layer graphene is half as compared to the bilayer graphene. The evolution of the Raman spectrum in Fig. 2.13 (b) shows the variation in the 2D peak with the graphene layers.
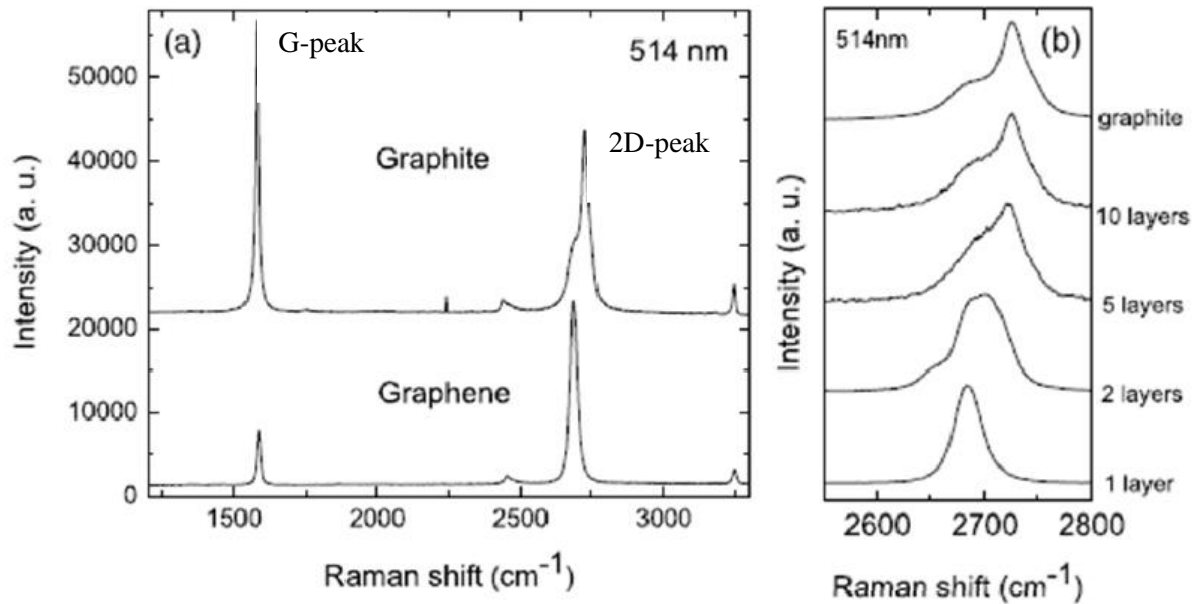
Figure 2.13: (a) Raman spectra of bulk graphite and graphene obtained using 514 nm excitation source. The prominent peaks obtained are at 1580 cm^{-1} and 2700 cm^{-1} .The peaks are scaled to have similar heights at ~2700 cm^{-1} .(b) Evolution of 2D peak with the number of graphene layers. The 2D peak can be used to count the number of graphene layers. Figure taken from Ref.[26].

A peak around 1350 cm^{-1} is observed in defected graphene. The origin of this peak is attributed to the number of defects present in the graphene sample.

All this information has served as a starting point for the investigations presented in the next chapters.

Chapter 3

Raman Spectroscopy in Graphene

3.1 Introduction

In the past few years major advances in the applications of Raman spectroscopy to materials studies has been observed and Raman spectroscopy has become a useful material characterization tool. Historically Raman spectroscopy has played an important role in exploring the characteristics of the graphitic materials which is the basis for many new nanomaterials. Raman spectroscopy is a sensitive and versatile technique for the nano-world and gives useful information like chemical impurities, optical gaps, doping, and defects about nanocarbon materials.

The main source of the Raman spectra are the vibrational modes of the crystal lattice in solids where the phonon is the quantum of the atomic vibration. These vibrational modes are related to the chemical and structural properties of the materials. Since every material has a unique set of the vibrational modes, Raman active phonon spectra can be used to distinguish the various materials of the carbon family. Monolayer graphene which is the building block of all the carbon based materials has Raman spectra as presented in the top spectrum of the Fig. 3.1. All other carbon materials have distinct spectra which can be used to study their properties on the basis of their Raman spectra. The rapid development in the study of the Raman spectroscopy has promoted advances in this field of carbon materials.
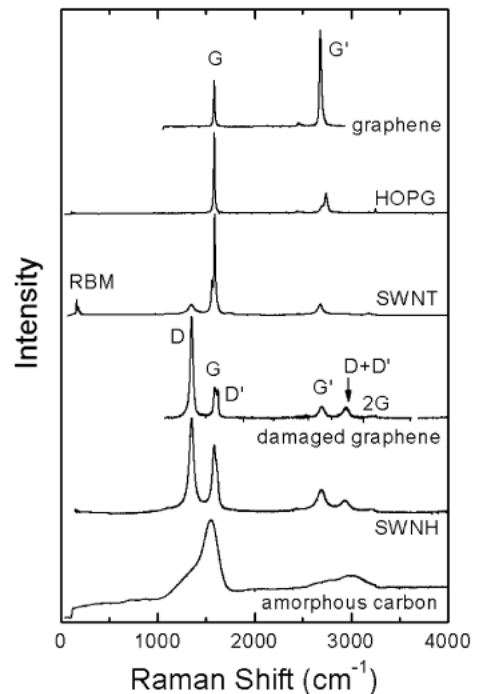
Figure 3.1: Raman spectra of different crystalline and disordered carbon nanostructures [29].

The basics of light scattering in solids, the Raman Effect, characteristic features of the Raman spectrum particularly the Raman spectroscopy in graphene are discussed in this chapter. Figure 3.1 represents the Raman spectra of various types of nanocarbons and the topmost spectrum shows the Raman spectra of the monolayer graphene. This chapter closely follows the reference [31, 32].

3.2 Raman Spectroscopy

Raman spectroscopy is very well employed to study the vibrational spectra of materials. It is a crucial analytical and research tool to study the properties of the materials and can be used both as a qualitative and quantitative technique to probe the material properties in detail.

In Raman spectroscopy the sample is irradiated by intense laser beams in the UV-visible region (υ_0) and the scattered light is detected as described in the Fig. 3.2. Scattered light of two types can be seen: Raleigh scattering which is strong and has the same frequency as of the incident beam (υ_0) and the other one is the Raman scattering which is weak and has the frequencies $\upsilon_0 \pm \upsilon_q$, where υ_q is the vibrational frequency [30].
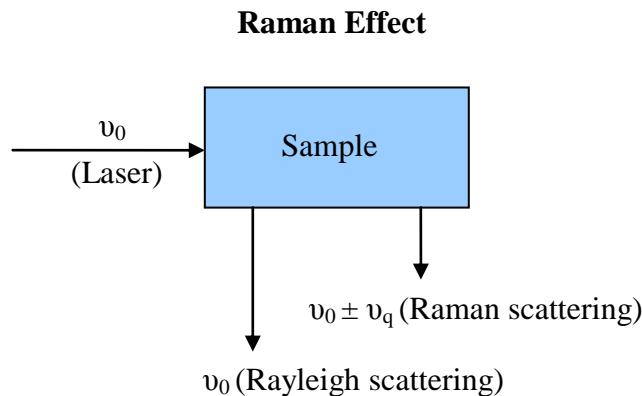
Raman Effect

Figure 3.2: Schematic diagram for the Raman (inelastic scattering) and Rayleigh (elastic scattering) effect of light [30].

So the vibrational frequency as a shift from the incident frequency υ_0 is measured in the Raman spectroscopy as represented in Fig. 3.2. The lines υ_0-υ_q and $\upsilon_{0+}\upsilon_q$ represents the stokes and anti- stokes lines respectively as shown in Fig. 3.4.

3.2.1 Vibrational modes from crystal Lattice in Solids

The characteristic vibrational modes are called the normal modes and are related to the chemical and structural properties of the materials. There is a periodic arrangement of a large number of atoms in the crystal. Consider 'N' as the number of atoms in the unit cell and N_Ω ~10^{23} per mole as the number of unit cells in a mole of the crystal. So the vibrational modes will be $3 \times N_\Omega \times N$ for a crystal of infinite size and these vibrational modes are grouped into various phonon branches. $3 \times N_\Omega$ modes are related to the translation, N_Ω unit cell along the three direction of the space and all the remaining $3 N_\Omega$ -3 modes are vibrational modes and grouped in three branches called acoustic branches that can be longitudinal acoustic (LA) or transverse acoustic (TA) depending whether the vibrational amplitude is parallel or perpendicular to the wave propagation vector respectively. All other $3 N_\Omega N$ -3 N_Ω are also the vibrational modes and are grouped into the 3N-3 branches called the optical branches. Similar to the acoustic branches these optical branches are also taken into longitudinal and transverse modes. Inelastic light scattering by the optical phonons is called Raman scattering. The difference among phonons in the branch is given by the phonon wave vector. Phonon wave vectors denoted by 'q' have the energy relation $E_q = \hbar\omega_q$ and a plot of ω_q and q gives the phonon dispersion relation as shown in Fig. 3.10(b) for graphene.

3.2.2 Light Scattering Phenomena in Solids

When the light is imparted to a material, part of it simply passes through the materials while the remaining photons of light interact with the material via light absorption, reflection or light scattering. The electronic and vibrational properties of the material determine the amount of light transmitted and interacting with the material. Depending upon the energy of the incoming light different phenomena can occur and Raman scattering is one of such phenomena discovered in 1927 by Chandrasekhara Venkata Raman. The light scattering phenomena is a useful tool to study the properties of a solid material by observing the excitations in the solids.

In Raman scattering no real absorption of light occur rather the photons cause vibrations of the atoms producing the phonons in the material. In this process the photon shakes the electrons and these electrons scatter the energy back into another photon. This photon will

have lost or gained the energy to or from the vibration of the atom. Therefore Raman scattering is an inelastic scattering process that creates or absorbs a phonon. When the photon loses energy in creating a phonon it is a stoke process and is an anti-stoke process if the photon gains energy by absorbing the phonon as shown in Fig.3.4. In Raman scattering the optical phonons are responsible for the inelastic scattering process. Figure 3.3 represents the elastic (Rayleigh) and inelastic (Raman) scattering of the incoming light and respective transitions in the vibrational levels of the atoms in the solid.
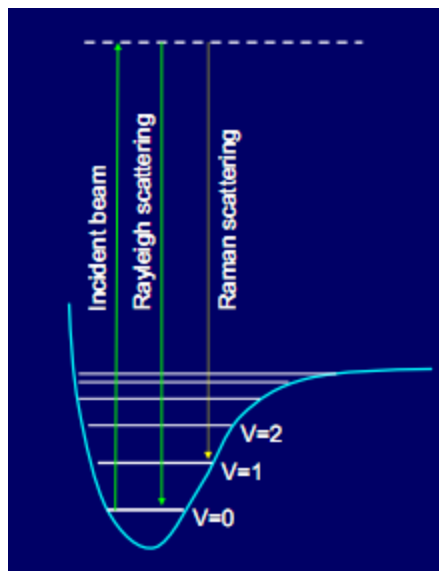
Figure 3.3: Raman scattering process showing the transition between the vibrational levels by incident light.
(Image taken from:
http://www.chem.purdue.edu/jcheng/Lectures/Lecture%202%20Aug%2024%20ligh%20matt er%20interactions.pdf)

In Raman spectroscopy we can have Normal Raman and the Resonance Raman. In case of the normal Raman, the exciting frequency υ_0 is such that its energy is far below the first excited electronic state. Whereas in the Resonance Raman (RR) scattering the exciting frequency υ_0 has the energy matching an excited electronic state. The probability of the scattering events increases by many orders of the magnitude which show the strong enhancement of the Raman band. Similarly if the scattered light energy is equal to the electronic transition energy, the resonance takes place. The resonance effect is extremely important in nanostructures and the large enhancement of the Raman signal associated with the resonance Raman scattering

(RRS) process also provides a means to study the Raman spectra of single graphene layer [32].

3.2.3 Raman Scattering Effect

In this process an incident photon with energy $E_i = E_{laser}$ and momentum $k_i = k_{laser}$ reaches the material and scattered, resulting in a photon with different energy E_s and momentum K_s. The energy and momentum conservation represents:

$$E_s = E_i \pm E_q \text{ and } k_s = k_i \pm q \tag{3.1}$$

Where E_q and q are the energy and momentum of the phonon that is created or absorbed in the inelastic Raman scattering process.

The inelastic scattering by the phonons occur because at different atomic positions in the vibrational mode of the atom, the ability of the photon to shake the electron will be different and is measured in terms of the polarizability that can be explained by the classical description of the Raman effect.

3.2.4 Theory of Raman Scattering:
Classical description

Classical electromagnetic theory can be used to describe and explain the Raman effect. Light scattering on the basis of the classical theory can be explained by considering a solid in an electric field E. The applied field E polarizes the atoms in the solids and the resulting polarization P is:

$$\boldsymbol{P} = \alpha.\boldsymbol{E} \tag{3.2}$$

Where α is the polarizibility tensor of the atom in the solid.

The electric field of the light is given as:

$$\boldsymbol{E} = \boldsymbol{E_0} sin\omega_i t, \tag{3.3}$$

ω_i is the optical frequency, the lattice vibrations in the solid with frequency ω_q modulates the polarizibility α of the atoms

$$\alpha = \alpha_0 + \alpha_1 sin\omega_q t \tag{3.4}$$

Where ω_q is the normal mode frequency of the solid that couples to the electric field of the light so that the polarization induced by the electric field becomes:

$$P = E_0(\alpha_0 + \alpha_1 sin\omega_q t)sin\omega_i t \tag{3.5}$$

$$P = E_0[\alpha_0 sin(\omega_i t) + \frac{1}{2}\alpha_1 \cos(\omega_i - \omega_q)t - \frac{1}{2}\alpha_1 \cos(\omega_i + \omega_q)t] \tag{3.6}$$

The above equation obtained by the classical theory of light shows that the light is scattered both elastically and inelastically. The second term in the equation downshifted by the vibration frequency ω_q of the atom shows the stokes process and the term upshifted by the same frequency ω_q gives the anti-stokes process.

3.2.5 Raman Selection Rules

Raman line is the representative of the mode of the vibration. Out of all the vibrational modes particular modes in the materials are Raman active and are referred as the selection rules. Equation (3.7) shows that the Raman scattering will obey the condition that

$$\left(\frac{d\alpha}{dq}\right) \neq 0 \tag{3.7}$$

The above condition can be interpreted as if the rate of the change of the polarizibility with the vibration is not zero then the vibrational mode will be Raman active. Therefore if the mode of vibration satisfies the above condition the mode will be Raman active and the Raman spectrum will show a Raman line of the material. So that each mode of vibration will give rise to a particular change in the polarizibility of the atom.

3.2.6 Raman Spectrum

A typical Raman spectrum is a plot of the scattered intensity I_s along the ordinate and the E_{laser} - E_s (Raman shift) along the abscissa. The energy conversation given by equation 3.1 as: $E_s = E_i \pm E_q$ is valid in Raman spectroscopy. Where E_s is the light (photon) energy different from the initial energy $E_i = E_{laser}$ and E_q is the energy change during scattering process. Phonons are involved in scattering phenomena so E_q can be considered as the energy of the phonon created or annihilated in the inelastic scattering process. The Raman spectrum shows the peak at $E_{laser} - E_s = E_q$. With respect to the Rayleigh signal, the anti-stokes signal appears in the opposite position relative to the stokes signal and usually the anti-stokes signal is weaker than the stokes signal as shown in Fig. 3.4.
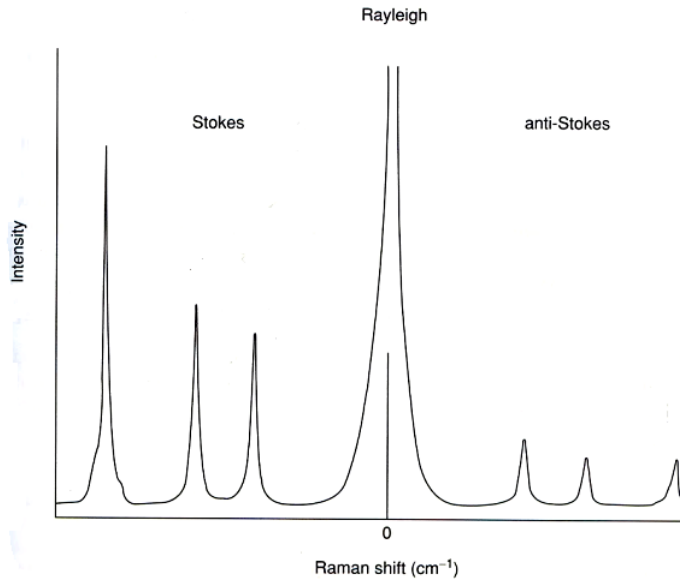
Figure3.4: Schematic showing the Raman spectrum. Rayleigh peak (at 0 cm^{-1}) has intensity always much higher than the Raman signal and Raman stokes process is usually stronger than the anti-stokes process.

3.2.7 First and Higher order Raman bands

The number of the scattering events involved in the Raman process gives the order of the Raman process. The first Raman order is the most common case in which the photon energy exchange generates a phonon with very small momentum ($q \approx 0$) whereas the second, third or higher Raman orders occur if two, three or more Raman events will take place. In the first order Raman process which is a one-phonon scattering process, the momentum transfer is small and can be neglected that is $k_s - k_i = q \sim 0$. The momenta associated with this process of first order scattering are of the order of k_i and the incident wave vector $k_i = 2\pi/\lambda_{light}$ where the value for λ_{light} is in the range of 800-400 nm. Therefore k_i is very small compared to the dimensions of the first Brillouin zone (given by q=2π/a, a= 0.246 nm for graphene). For this reason only the phonons near the center of the Brillouin zone Γ that is at q~0 are activated in the first order Raman process. The phonon momentum q ≠0 is important only in higher order Raman scattering processes. The first order Raman spectra give the basic quantum of vibration and higher orders give information about overtones and combination modes. In addition to the Raman peaks of the Raman active modes some other modes are commonly observed in the Raman spectrum. These modes are called combination and overtone modes.

51

Combination mode appears when two Raman active modes are combined together and a new Raman peak appears in the Raman spectrum. Its position will be at or very close to the sum of the positions of these Raman active modes. In the combination modes the Raman signal appears at the sum of different phonons energies that is $E_{q1}+E_{q2}$,... . Overtone modes are the higher orders of Raman active modes and have a lower intensity than the original peak. The peak of a second order mode will be at or close to twice of the frequency of the original mode and a third order mode will be at or close to three times frequency of the original mode and so on. Raman signal appears at nE_q (n=2,3,...) in the overtones .

As an example Fig. 3.5 shows Raman spectra of pyrocarbon. The Raman peaks of the graphitic material (pyrocarbon) shown in figure 3.5can be taken. The Raman spectra have peaks at 1354, 1581 and 1620cm^{-1} as the first order Raman and Raman peaks at the 2708, 3185, 3245 cm^{-1} as the second order peaks. In addition to these overtones, the Raman spectrum exhibits the combination peak at 2950 cm^{-1} due to the combination of the peaks at 1354 and 1581 cm^{-1}.
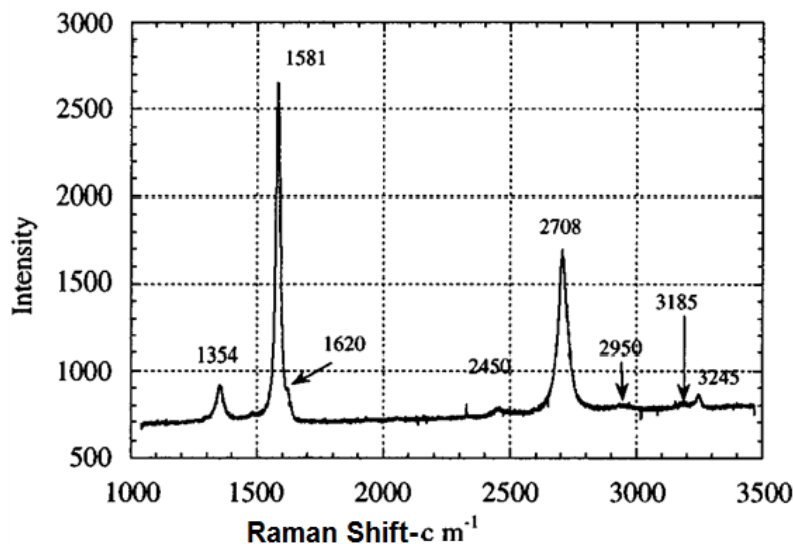
Figure 3.5: Raman spectra of graphite with Raman first order, second order and combination modes [31].

3.2.8 Quantum description of Raman Scattering

The atomic configuration in the crystals is not changed by exciting one electronic state whereas the second order perturbation can give rise to the elastic (Rayleigh) scattering. It is necessary to involve third order perturbation theory to describe the Raman process in crystals.

In this process the excited electron perturbs the atom in creating a phonon through an electron-photon interaction as shown in Fig. 3.6.
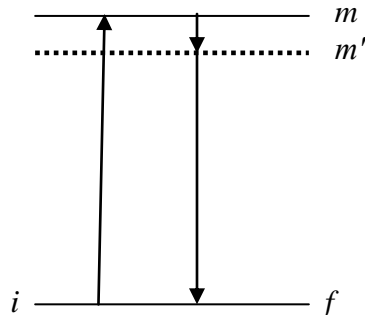
Figure 3.6: Schematics of the Raman process in crystals with upward and downward arrows showing the transitions [32].

In the above Fig. 3.6 the vibrational states are not displayed and only electronic states are displayed to explain the Raman process. The small downward arrow in this figure shows the electron-phonon scattering event during this process.

If i represents the initial state of the electron with energy E_i and the absorption of the incident energy E_{laser} excite the electron to a higher energy state m with energy E_m and if m is a real electronic state, the process is a resonant process. The electrons will be further scattered by q ≈ 0 phonon to a virtual state m' and come back to the initial state by emitting the scattered light. Therefore the initial system has an electron in the initial state i and a photon of energy E_m-E_i and the final system has an electron in the state i , a phonon of the energy E_q and the photon of energy E_m-E_i- E_q. Also the scattered resonance process is possible, during which photon emission is resonant instead of photon absorption resonance process. In this process the incident photon can excite the electron to the virtual state with the higher energy and light scattering bring the system back to the final state of the system. For the higher order of the Raman process the fourth order perturbation theory is to be considered. In the 2nd order Raman scattering process there is an internal electron scattering process by a phonon and another by a lattice defect which is an elastic process. In the two-phonon scattering processes with phonon wave vectors q and −q, the momentum conservation is possible with q$\neq$0.

3.2.9 Components of the Raman Spectrometer

Modern Raman Spectrometer comprises of the six main components which can be described as:

1. Excitation light source
2. Optical guiding system
3. Optical microscope
4. Spectrometer
5. Detector
6. Data acquisition unit

Figure 3.7 is the schematic diagrams of the different components of the Raman system.
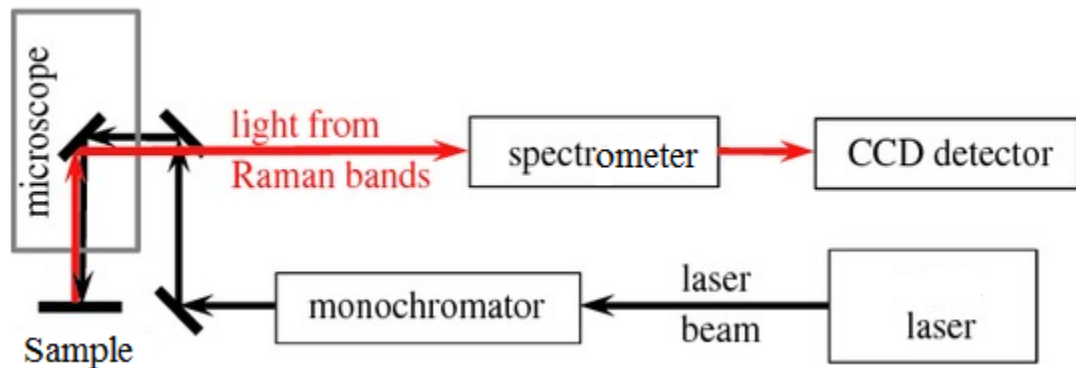
Figure 3.7: Schematic of the Raman Spectroscopy system.

A laser is always used as an excitation source. The monochromatic lasers usually used in the Raman Spectrometers as an excitation source are:

Visible range: Helium Neon red (632 nm) and argon ion green (514 nm)

Infrared range: (785 nm and 830 nm)

UV range: (200-300 nm)

An optical microscope is used for focusing of light on the sample, collection of the backscattered light and sending the light to the spectrometer. Microscope movement in micron and sub-micron steps is usually very useful in many Raman mapping experiments.

The spatial resolution of this technique is limited to the size of the laser spot interaction volume with the sample.

The optical guiding system consists of the group of mirrors to direct the laser beam from the source to the sample and back to the spectrometer, to holographic filters to remove the plasma lines from the laser beam and a set of the polarizing units to control the polarization of the incident and the scattered beams.

The spectrometer has a group of gratings and mirrors that can be adjusted in different ways. The spectrometer has the following two purposes: One is to separate the Rayleigh scattered light from the Raman signal. This can be done by the holographic notch filter, an edge filter or a monochromator. Notch filter can collect both stokes and anti-stokes lines whereas the edge filters can collect stokes Raman lines only. The other purpose of the spectrometer is to analyze the collected signal. This optical signal is dispersed according to its wavelength and the output spectrum is reimaged at the exit slit. The spectrometer has a group of gratings and mirrors that can be arranged in different ways to give one of the spectrometer subclasses including monochromator, scanning monochromator, polychromator, spectrograph or imaging spectrograph.

Detectors in the Raman system can be single or multi-channel. The single channel detectors (Photomultiplier tubes (PMTs)) take one wavelength to read at a time. They are widely used in the Raman systems due to their high sensitivity, low background counts, wide covered range and relatively low costs. The main disadvantage is that it need a long time to record the spectrum. The multi-channel detector can be used in the form of a charge coupled device (CCD) or an array of light sensitive units. They can record the wide range of wavelengths at the same time.

The data acquisition unit which is the last component of the Raman system is a PC interfaced with the detector to store, display and manipulate the data Advanced software has been developed and used to interpret the data in a better manner.

Figure 3.8(a) is the image of the Raman system used now a days and figure 3.8(b) illustrate the schematic of the Raman spectrometer.
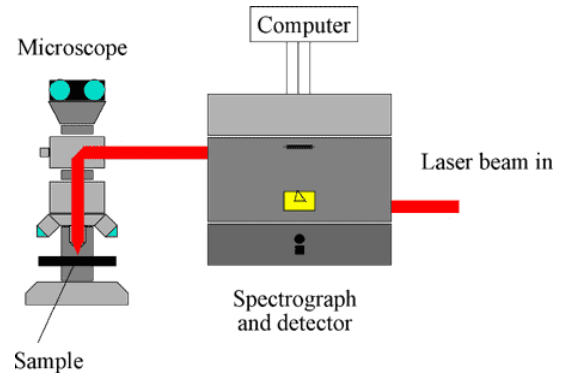
| (a) | (b) |

Figure 3.8: (a) Image of the Raman Spectroscopy system and (b) schematic of the Raman spectroscopy system.

The images of figure 3.8 (a) and (b) are taken from: http://chem.skku.ac.kr/~skkim/reseach-facility.html and http://www2.angstrom.uu.se/nanocentre/infrastructures/m_raman.html

3.3 Phonons in Graphene

The creation or annihilation of the polaritons, plasmons, magnons or any elementary excitations in solids gives rise to the inelastic process of Raman scattering. The phonons are the quanta of the vibrations in the solids and are the main source of the Raman spectra. Like electrons, the phonons also depend on the atomic structure of the material and Raman phonon spectra can be used to study and distinguish the members of carbon family. The plot between the phonon wave vector and phonon frequency represents the phonon dispersion relation and figure 3.10(b) represents the phonon dispersion relation of monolayer graphene. The discussion of phonon dispersion in graphene closely follows the reference [32]. Six branches in these phonon dispersion relations are due to the reason that the graphene crystal has a unit cell with two distinct atoms A and B. Graphene phonon dispersion relation has three acoustic (A) branches and three optical (O) branches. For one acoustic branch (A) and one optic (O) phonon branch, the atomic vibrations are perpendicular to the graphene plane, and they correspond to the out-of plane (o) phonon modes. For two acoustic and two optic phonon branches, the vibrations are in-plane (i). The directions of the vibrations are considered with

56

respect to the direction of the nearest carbon_carbon atoms and, therefore, the phonon modes are classified as longitudinal (L) or transverse (T) according to vibrations parallel with or perpendicular to the A_B carbon_carbon atoms respectively. The modes associated with out-of-plane, in-plane longitudinal and in-plane transverse (T) atomic motions are shown in Fig. 3.9(a). The six phonon dispersion curves shown in Fig. 3.9(b) are assigned to the six phonon modes LO, iTO, oTO, LA, iTA, and oTA.

(a)   (b)
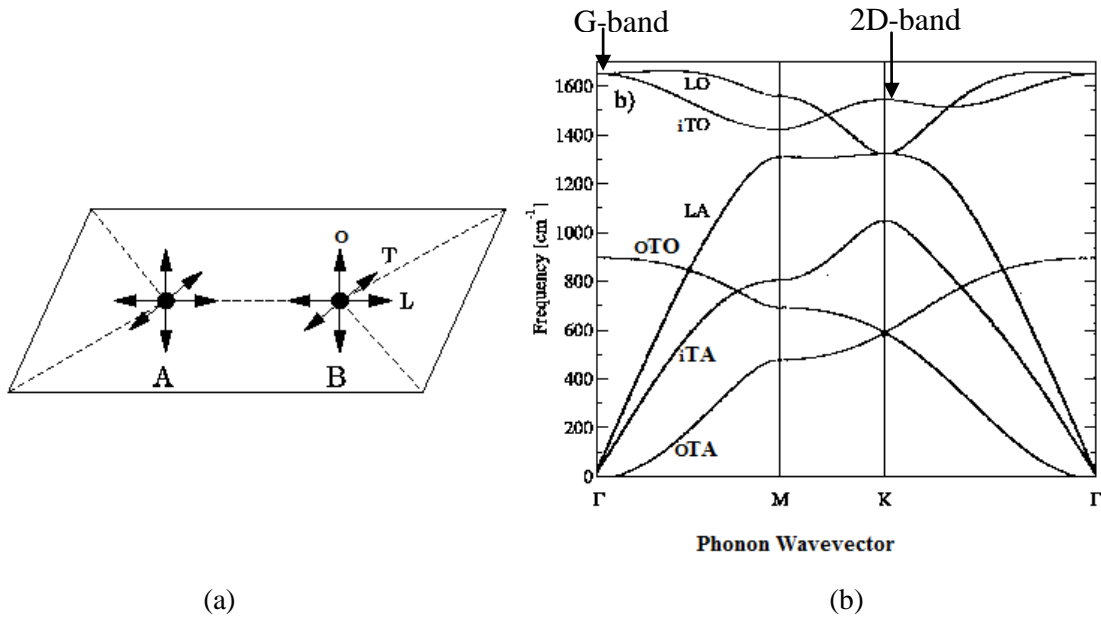
Figure 3.9: (a) Atomic motions of carbon atoms in graphene can be along the out-of-plane (O), in-plane transverse (T), and in-plane longitudinal (L) direction.(b) The Phonon dispersion curves for monolayer graphene plotted along high symmetry directions [20].

The in-plane iTO and LO optic modes near the Γ point correspond to the vibrations of the sublattice A against the sublattice B as shown in Fig. 3.10, and these modes are degenerate at the Γ point. The degenerate zone-center LO and iTO phonon modes belong to the two-dimensional E_{2g} representation according to Group Theory and are Raman active modes.
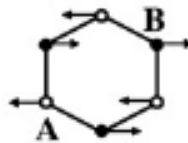
Figure 3.10: Schematic of the carbon atom motion in G phonon lattice vibration [33].

The phonon modes around the K point are especially important as they contribute to the Raman peaks specific to graphene. Exactly at the K-point, the phonon which comes from the iTO branch is non-degenerate. The LO and LA phonon branches meet each other at the K point giving rise to a doubly degenerate phonon.

3.4 Raman Spectroscopy of Graphene

Graphene has been extensively studied both theoretically and experimentally since its discovery in 2004 and these investigations reveal its extra-ordinary electrical, mechanical and other physical properties including its potential for future application in numerous fields. Raman spectorscopy has the powerful ability to investigate the vibration modes and the perturbation effects and is also successfully employed to study graphene in this respect [34-37]. Raman fingerprints for single, bi and few layer graphene lead to the authenticated, high throughput and non-destructive identification of the number of layers [36]. The graphene Raman spectrum has two major Raman active modes as G-band around 1580 cm^{-1} and G′-band (2D band) around 2700 cm^{-1}. The comparison of the graphite and graphene Raman spectra is shown in Fig. 3.11.
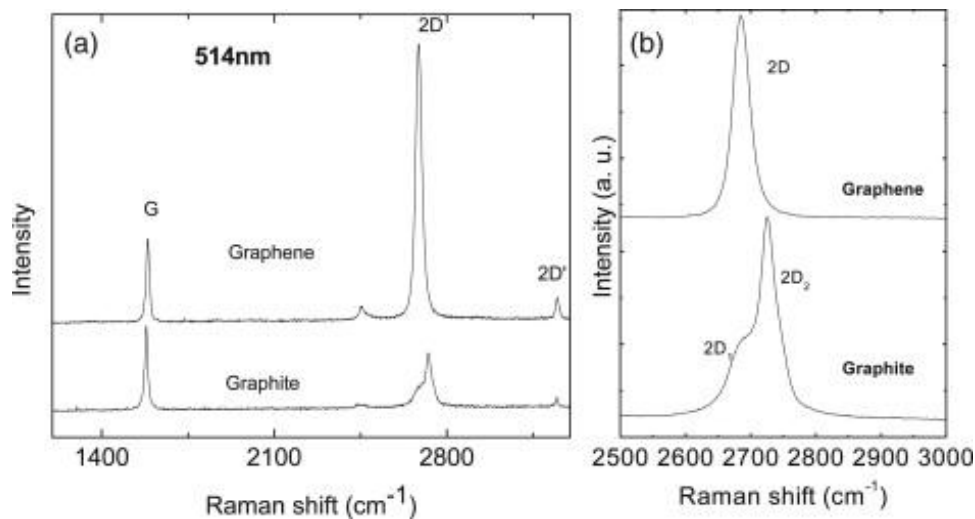
Figure 3.11: (a) Comparison of the Raman spectra of graphene and graphite measured at 514.5 nm. (b) Comparison of the 2D peaks in graphene and graphite [34].

The G-band is related to the doubly degenerate (iTO and LO) phonon mode (E_{2g} symmetry) at the Brillouin zone center [35] shown in Fig. 3.9(b). In fact, the G-band is the only band coming from a normal first order Raman scattering process in graphene. Figure 3.10 represents the carbon atom motion giving rise to the lattice phonon vibration responsible for the G band.

The intensity of single layer G peak and bulk graphite is comparable as can be seen in Fig. 3.11(a). The G peak position is an important parameter and the position of the G peak is 3-5 cm^{-1} higher than in the bulk graphite. The Raman shift (cm^{-1}) of the G peak towards higher wave number for few layer Graphene and Single Layer Graphene (SLG) is attributed to doping [26] and lower wavenumber shifts represent strain [27].

On the other hand, the G′ and D bands originate from a second-order process, involving two iTO phonons near the K point for the G′ band or one iTO phonon and one defect in the case of the D-band as schematically explained in Fig. 3.12. The G′ band appears at the frequency twice the D band frequency and is often called 2D band in the literature.
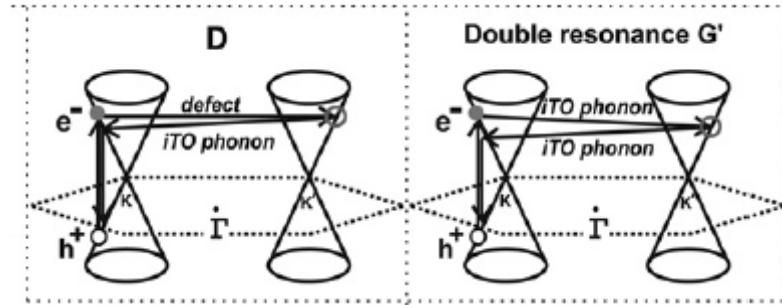
Figure 3.12: Electron dispersion diagram for one-phonon second-order double resonance (DR) process for the D-band and two-phonon second-order resonance Raman spectral processes (intervalley process) [35].

In the process of double resonance (DR) as shown in the above Fig. 3.12, the electron of wave vector **k** around K absorbs the incident photon energy E_{laser}. The electron is inelastically scattered by a phonon or a defect of wave vector **q** and energy E_{phnon} to a point around K′ with wave vector **k** + **q**. The electron is then scattered back to the k point by emitting a photon of wave vector **k**. The double resonance mechanism is used to explain the 2D band in which two phonons are taking part and both processes are the inelastic scattering events. The DR is called an intervalley process as it joins the points around K and K′ points. For the D band out

of the two scattering processes one is an elastic scattering by the defects in the crystal lattice and one is inelastic by emitting or absorbing a phonon.

The 2D peak in graphene is due to the two phonons with opposite momentum in the highest optical branch near K shown in Fig. 3.9(b). The 2D band is the second order of zone boundary phonon excitations. Since the zone boundary phonons do not satisfy the Raman selection rule [26] as described by the equation (3.7), they are not present in the first order Raman spectra of defect free graphite. The process of double resonance (DR) given by Thomsen and Reich [38] can be introduced to explain the splitting of the 2D peak in multiple graphene layer [26]. The process of DR relates the phonon vectors to the electronic band structure [38] and Raman scattering is the fourth order process of the virtual transitions within DR described in [26]:

i.   An electron-hole pair (vertical) excitation a →b by laser.
ii. Electron-phonon scattering with an exchanged momentum q close to K (b →c).
iii. Electron-phonon scattering with an exchanged momentum −q (c → b).
iv. Electron- hole recombination (b → a).
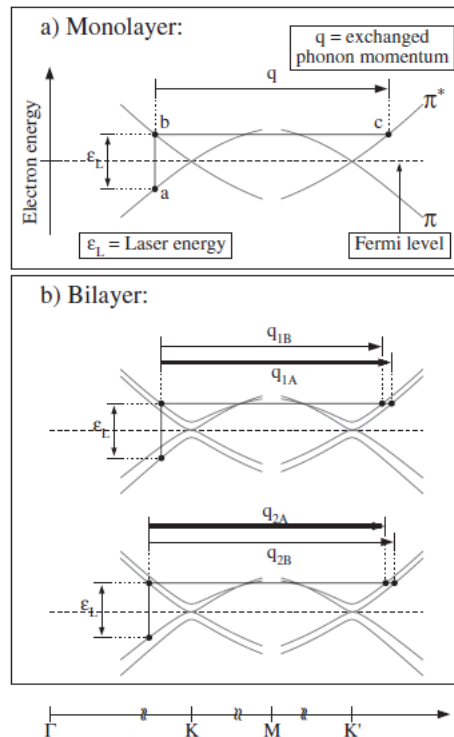
Figure 3.13: Phonon dispersion for double Resonance (DR) for 2D peak in graphene (a) single layer and (b) bilayer [26].

If the energy is conserved in all these transitions then DR condition is attained and the Raman frequency at the output is twice the frequency of the scattered phonon with the q determined by the DR condition. Only the dispersions along, $\Gamma - K - M - K' - \Gamma$ are considered in the DR process and the phonons with momentum $\mathbf{q} > \mathbf{k}$ satisfying the DR condition along $\Gamma - K - M$ are present in Fig. 3.13. Two other possible phonons, $\mathbf{q} < \mathbf{k}$ and $\mathbf{q} \sim \mathbf{k}$ contribute very small signals in the Raman intensity. The splitting of the 2D peak in bilayer graphene is due to splitting of the electronic band structure. The interaction between the graphene layers divides the graphene bands into four bands, and out of the four possible optical transitions the incident light couples more strongly with the two transitions shown in Fig. 3.13 (b). Due to the high sensitivity of the G′ band (2D band) for the electronic structure it is used for the identification of the graphene layers (mono, bi, tri,….multi layers).

A significant change in the shape and the intensity of the 2D peak of graphene compared to the bulk graphite can be seen in Fig. 3.11 (b). The 2D peak of bulk graphite has two components $2D_1$ and $2D_2$ with roughly ¼ and ½ the height of the G-peak whereas the graphene has a single sharp 2D peak roughly 4 times more intense than the G-peak as shown in Fig. 3.11(b). The evolution of the 2D band as a function of the layers for the 514 nm excitation source is shown in Fig. 3.14. It is obvious that the 2D peak of the bilayer is much broader and up-shifted with respect to graphene. The four components of bilayer graphene are $2D_{1B}, 2D_{1A}, 2D_{2A}, 2D_{2B}$ as shown in Fig. 3.15 The intensity of two components $2D_{1A}$ and $2D_{2A}$ is higher than the other two.
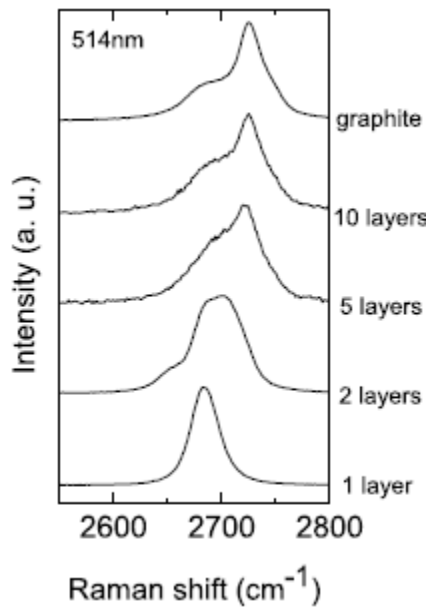
Figure 3.14: Evolution of 2D peak in graphene layers [26].
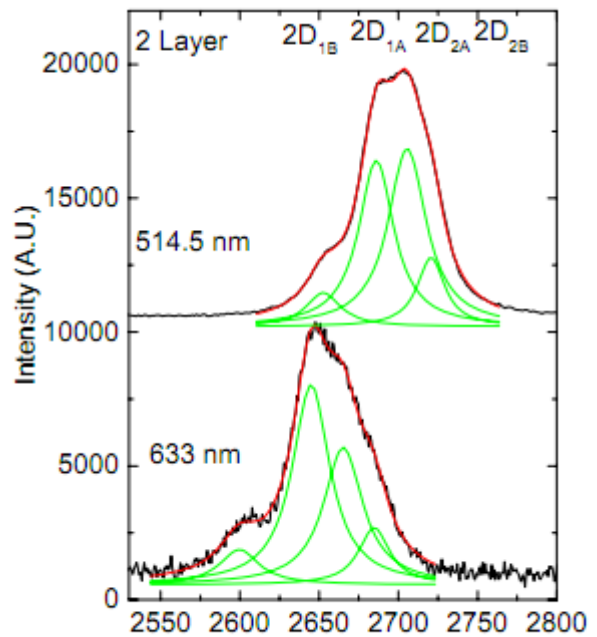
Figure 3.15: The four components of the 2D band in 2 layer graphene at 514 nm and 633 nm for 2D peak [26].

A disorder induced double resonance D-band around 1360 cm^{-1} is also observed in the graphene Raman spectra. It is considered that Double Resonance is the activation mechanism for the D-peak [26, 35] as explained above and Transverse optical (TO) phonons around K are responsible for this D-peak. The D-peak at the edge of a monolayer graphene flake using 514 nm excitation source is shown in Fig. 3.16.
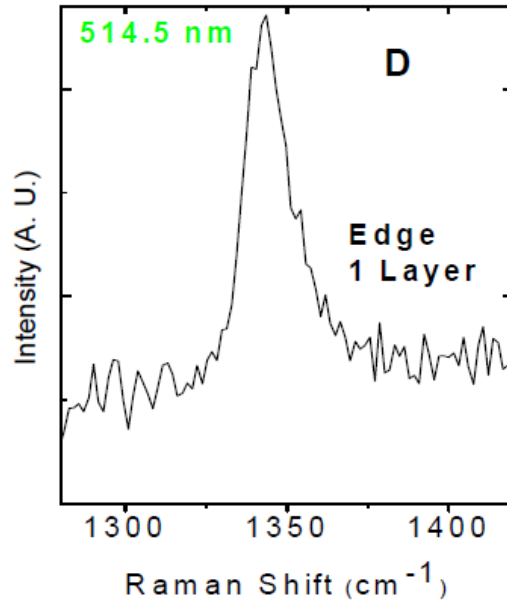
Figure 3.16: D peak at the edge of single layer graphene using 514 nm excitation source [26].

In the graphene films deposited on the substrate, strain is induced in graphene due to substrate roughness (1-2nm) which is thought to be the reason of the D-band [31]

The basics of Raman scattering and the Raman Effect in graphene explained in this chapter are helpful to study and understand the next two chapters describing the effect of strain on graphene and the study of the compressive behaviour of graphene.

Chapter 4

Effects of Strain on Graphene properties

4.1 Introduction

Graphene is a material with single-atom thickness having many outstanding properties such as linear electronic band structure, anomalous quantum Hall effects, high mobility, extraordinary high thermal conductivity, highest stiffness and strength. These properties have remarkable dependence on its morphology and atomic structure [2, 4, 6, 28]. Many efforts have been dedicated to study the electronic properties of graphene, and to create a band gap that could allow the use of graphene in electronic applications [42]. A number of mechanisms have been proposed with that purpose: nano-pattering [47], quantum dots [48,60], chemical functionalization (molecular doping) [49] and applying mechanical stress [27,43,44].

The electronic structure changes with the elastic strain [28, 45, 46]. Strain engineering, or more generally tuning material properties by applying mechanical loads or deformation, is a powerful strategy in improving the material performance. Strain engineering is a general strategy employed in silicon based semiconductor industry. Strained silicon has much higher mobility (50% increase in room temperature mobility by strain of the order 1%), and thus much better performance. The effects of strain become much more significant at low dimensions as directional load is more feasible and the bending of two-dimensional membranes or one-dimensional ribbons can easily be excited resulting in a significant local curvature [51].

Recently bendable and flexible electronics have generated much interest from various research areas which deal with graphene deformed under stress. Thus, the study of the deformation of graphene and its resulting impact becomes extremely important. Molecular functionalization on graphene usually induces structural distortion as it disturbs or breaks the underlying sp^2 bonding network thus forming sp^3 bonds locally. Vice versa, mechanical deformation, which modifies the sp^2 bonds features, provides another method to tune

graphene properties, reversibly. This approach, in combination with molecular doping [13,14] is expected to play a critical role in nano-engineering of graphene and related materials. Poly Nanocomposites have attracted considerable interest due to their outstanding mechanical, optical, electrical, and thermal properties [52]. Utilization of graphene in polymer materials introduces a new and advanced class of materials such as graphene polymer nanocomposites [53]. The study of stress transfer from graphene (nanofillers) to the polymer matrix [54] is very important and helpful in the practical applications of these graphene based polymer nanocomposites. Additionally Raman spectroscopy has proven to be an excellent tool to investigate the changes in the electronic band structure of graphene under various perturbations.

4.2 Review of the Elastic behaviour of Materials

The application of graphene as a strongest material in nanoscale devices and composite materials has aroused great interest for the graphene research in this area.

All materials possess the property of elasticity to a certain extend. The material resumes its original state after the stress (external forces) causing the material deformation is removed, if the applied forces do not exceed a certain limit. The amount of the deformation produced in the material is called the strain. The stress applied on the material is the force per unit area and has a normal and a shear stress component depending upon whether the force is acting perpendicular or tangent to the plane respectively as shown in Fig. 4.1.
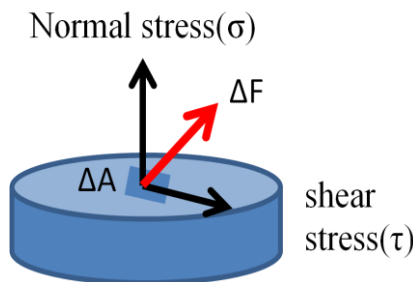
Figure 4.1: Stress component Parallel and perpendicular to the plane.

Out of the various stress types, the effect of tensile and compressive stress on graphene is studied in the work presented in chapter 5. Tensile stress (tension) is the normal stress applied to the body and produces elongation in the applied force direction and the compressive stress (compression) is the normal stress applied to the body and shrinks it in the direction of the applied forces. During load applications tension is taken as positive and compression as the negative. Both stress types are illustrated in the Fig. 4.2.
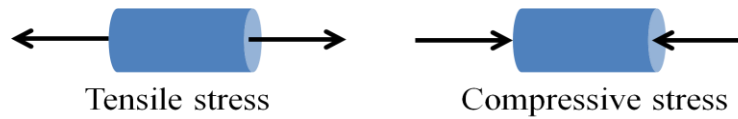
Figure 4.2: Tensile and compressive stress.

The components of the force per unit area on the material surface i.e stress can be written in terms of a second order stress tensor following symmetric condition $\sigma_{ij} = \sigma_{ji}$:

$$\sigma_{ij} = \begin{bmatrix} \sigma_{xx} & \sigma_{xy} & \sigma_{xz} \\ \sigma_{xy} & \sigma_{yy} & \sigma_{yz} \\ \sigma_{xz} & \sigma_{yz} & \sigma_{zz} \end{bmatrix} \tag{4.1}$$

Whereas the symmetric second order strain tensor can be represented as:

$$\varepsilon_{ij} = \begin{bmatrix} \varepsilon_{xx} & \varepsilon_{xy} & \varepsilon_{xz} \\ \varepsilon_{xy} & \varepsilon_{yy} & \varepsilon_{yz} \\ \varepsilon_{xz} & \varepsilon_{yz} & \varepsilon_{zz} \end{bmatrix} \tag{4.2}$$

And the Hook's law describing the stress-strain relation can be represented as:

$$\sigma_{ij} = c_{ijkl}\varepsilon_{ij} \tag{4.3}$$

Where c_{ijkl} are the elastic stiffness coefficients and components of a fourth order tensor.

In the elastic region the stress and strain are linearly related described by Hook's law. The non-linear region of the stress strain curve begins after a certain stress limit called as the elastic limit or yield strength as shown in the Fig. 4.3. Beyond this point the material deforms irreversibly and is in the plastic regime and after this comes the point which tells the maximum strength of a material (i.e Ultimate tensile strength, tensile strength or ultimate strength). It is the maximum stress that a material can sustain without breaking, failure or fracture of the material during stretching or pulling whereas the compressive
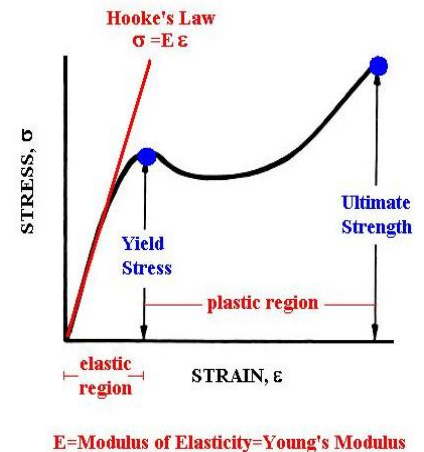
Figure 4.3: Stress-Strain curve for a typical material.
(Image taken from:
http://www.mae.ufl.edu/~uhk/STRENGTH.html)

67

strength is the capability of the materials to sustain axially directed forces.

Composite materials tend to have higher tensile strengths than compressive strengths. The materials which fail at low strain are brittle and the materials that are able to resist before failure are ductile. The Strength (tensile strength) of a solid material depends on the strength of its interatomic bonds. This strength relation is affected by the particular arrangement of atoms particularly in a periodic but imperfect lattice and a small imperfection in this arrangement is very critical and can lead to a plastic (nonlinear) response or brittle failure [55]. The stress induces motion of the existing defects, or a nucleation of the new defects in a perfect solid and the deformation becomes irreversible and permanent. When load is applied to a material in such a way that its crystal is compressed or stretched out of the equilibrium shape then a strain arises in it. The level of strain where the nonlinear effect begins to occur at a noticeable rate gives the yield strain εY or yield stress σY. In the case of tension this threshold shows the strength of chemical-bonds, and is expected to be high for C–C based material [55].

The elastic parameters define the mechanical properties of the material. These parameters are: Young's modulus E, the shear modulus G and the poison's ratio υ. The Young's modulus is the measure of the stiffness of the material and these parameters are linked to each other by the simple expression below taken from Ref [55].

For a three dimensional (3D) solid they can be defined as:

$$E^{3D} = \frac{\sigma_{xx}}{\varepsilon_{xx}} = \frac{1}{V_0}\left(\frac{\partial^2 E_s}{\partial \varepsilon_x^2}\right)_{E_0} \tag{4.4}$$

For a material, Hook's law defines the young's modulus as the ratio between the uniaxial stress σ_{xx} and the uniaxial strain ε_{xx}. Young's modulus can be calculated in terms of the strain energy E_s, tensile strain ε_x and the equilibrium volume V_0.

When the material is subjected to strain, the stored strain energy can be taken as the elastic strain energy density, whereas the strain energy is:

$$E_s = 1/2\sigma_x\varepsilon_x \tag{4.5}$$

The total strain energy is taken by integrating it over the volume of the deformed material.

The shear modulus can be represented in terms of the shear stress σ_{xy} and shear strain ε_{xy} as:

$$G^{3D} = \frac{\sigma_{xy}}{\varepsilon_{xy}} = \frac{1}{V_0}\left(\frac{\partial^2 E_s}{\partial \varepsilon_{xy}^2}\right)_{E_0} \tag{4.6}$$

And poison's ratio υ relates the axial strain ε_x with the transversal strain ε_y,

$$\vartheta = -\frac{\varepsilon_y}{\varepsilon_x} = -\frac{\varepsilon_z}{\varepsilon_x} \tag{4.7}$$

The shear modulus can be expressed as:

$$G^{3D} = \frac{E^{3D}}{2(1+\vartheta)} \tag{4.8}$$

Table 4.1: Young modulus of different materials [56]

Material	Young's Modulus (MPa)
Weak gels	<1ᶜ
Soft rubber	1–10
Hard rubber	100
Soft polymers (nylon, Teflon, PE)	500
Hard polymers (PMMA, PS, PVC)	3,000
Soft metals (Mg, Al), glass	40,000–80,000
Hard metals (bronze, steel, Ti)	100,000–200,000
SiC, WC, diamond	450,000–1,100,000

Whereas the young's modulus of carbon nanotubes is ~ 1TPa.

4.3 Elastic properties of Graphene

For 2D graphene in-plane stiffness is considered instead of the 3D Young's modulus. The in-plane stiffness of graphite is taken by considering an axial load applied on graphene [45] as shown in Fig. 4.4.
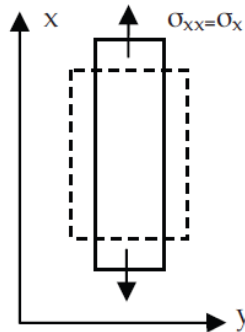
Figure 4.4: Lateral contraction due to an axial stress [45]

69

The elastic parameters for graphene can be written [45] as:

$$E^{2D} = \frac{1}{A_0}\left(\frac{\partial^2 E_s}{\partial \varepsilon_x^2}\right)_{E_0} = E^{3D} C_0 \qquad (4.9)$$

And

$$\vartheta = -\frac{\varepsilon_y}{\varepsilon_x} = -\frac{l_0}{w_0}\frac{\partial w}{\partial l} \qquad (4.10)$$

where A_0 is the equilibrium reference area of the 2D material with length l_0 and the width w_0 and the C_0 is taken as the interlayer distance between graphene layers i.e. $C_0 = 3.35$ Å.

The study of the elastic properties of the graphene is very important and also helpful in the design and control of nanographene structures and devices. The elastic properties of a single graphene layer were measured by Lee et al. [9] showing an elastic modulus value of 1.0 TPa, demonstrating that graphene is the strongest material known and exhibits a breaking strength of ≈40 N/m, reaching the theoretical limit. Graphene can bear ~ 20% threshold strain which no other material structure can. For the measurement of elastic constants Lee et al. [9] used the simple model of the elastic behaviour under uniaxial deformation as:

$$\sigma = E\varepsilon + D\varepsilon^2 \qquad (4.11)$$

Where σ is the stress, ε the strain, E the Young's modulus and D is the third order elastic modulus.

The intrinsic stress can be taken from the maximum elastic stress strain response given by the above equation (4.11) and the resultant values of intrinsic stress and strain obtained by Lee et al. [9] are:

$$\sigma_{int} = \frac{E^2}{4D} \quad \text{and} \quad \varepsilon_{int} = \frac{E}{2D} \qquad (4.12)$$

4.4 Effects of Strain on Graphene

Strain can be induced in graphene intentionally or naturally. Engineering local strain profiles produced by controlled mechanical deformation of the graphene or by introducing geometrical patterns in the substrate provides a promising approach to graphene based electronics. Figure 4.5 represents schematics of the graphene sheet subjected to the

mechanical deformation. The study of strained graphene is useful for several reasons: it can be employed to study the changes in graphene properties under perturbation effects. It also provides an alternative mechanism to open a band gap in graphene . It's a key factor to be known for the use of graphene as polymer nanocomposites.
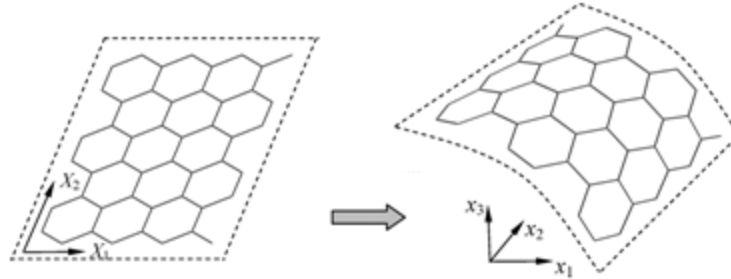
Fig.4.5: Schematic illustration of a 2D graphene sheet before and after deformation [57].

4.4.1 Effects on Electronic Properties

Graphene is a suitable candidate for next generation electronic devices due to its high mobility [58,62] and the excellent thermal conductivity [59]. Graphene lacks an electronic band gap [2] and therefore has no switching capability; which is essential for electronics applications. Opening an energy gap in graphene's electron energy spectrum is therefore a critical prerequisite for graphene based electronic devices such as a graphene transistor [60, 61]. Many mechanisms have been proposed to create a useful electronic band gap e.g. by quantum confinement of electrons and holes in nanostructure like graphene nanoribbons [63] or quantum dots [48,96]. These structures involve nanopatterning of graphene sheets, which tends to introduce unintended disorder and edge roughness [64,65] in the resulting nanostructures, which would be detrimental for the carrier transport and the performance of graphene-based devices.

Strain has been successfully applied to modulate the properties of the carbon nanomaterials [67] therefore attempts were made to utilize strain to modify the electronic properties of graphene [27,43,68,69]. These experiments regarding strain on graphene show that the controlled and reversible strain can be produced in graphene with observable effects. Motivated by the experimental work of graphene under strain theoretical analysis and calculations [44-46] have also been performed to understand the effect of strain on the electronic properties of the graphene.

The calculations of the tight binding model of graphene under strain shows a band gap opening for deformation beyond 20% [44]. According to Pereira and Castro Neto [44], Strain is an ineffective means to get a large/bulk band gap in graphene due to large threshold deformations/strain required to overcome the gap threshold. They describe that local strain can be introduced to affect transport and structural properties of graphene. The effect of local strain was further studied by Pereira and Castro Neto [45] showing that by varying the amount of local strain, the electronic structure (in turn electronic gap) of graphene can be tailored by effectively creating only small deformations of the carbon lattice. The studies [45] show that local strain can therefore generate the same features that are seen in graphene nanoribbons, except that the strain does not require to patterning (cutting) of graphene layers, and the process can be reversed by relieving the applied strain.

4.4.2 Graphene reinforcement in Polymer Nanocomposites

Polymer nanocomposites (PNCs) have become a large material class and are becoming a key area in nanoscience and nanotechnology providing significant potential in numerous and diverse applications [71]. Polymer nanocomposites are a combination of a polymer matrix and additives that have at least one dimension in the nanometre range. Additives can be one-dimensional, such as nanotubes and fibres, two-dimensional, which include layered clay minerals or graphene sheets, or three-dimensional, including spherical particles. PNCs are popular due to the outstanding mechanical, optical, electrical, and thermal properties encountered with only a small quantity of nanofiller incorporated into the polymer matrix. This is caused by the large surface area to volume ratio of fillers when compared to micro- and macro-scale additives. Polymer nanocomposites (PNCs) based on the carbon materials (nanofillers) have been used for their improved mechanical, electrical, thermal and gas barrier properties [72, 73].

High quality mechanical and electrical properties of graphene as well as its high aspect ratio and low density enables graphene to be an ideal candidate for the functional and structural graphene reinforced composites [74]. Therefore graphene as a reinforcement material for the future composite materials has drawn much attention. The ability of graphene to be dispersed into various polymers matrices and remarkably improving the properties of the polymers

introduces a new class of polymer nanocomposites [74-77]. Graphene-based PNCs are high-performance materials that offer improved mechanical, barrier, thermal and electrical properties with small nanofillers concentration [75].

 Dispersion and the interface are the two key parameters in the evaluation of the PNCs and play a very important role in the performance of the PNCs [74,75]. The maximum improvement in final properties can be achieved when graphene is homogeneously dispersed in the matrix and the external load is efficiently transferred through strong filler/polymer interfacial interactions [71]. Because of large flat surface area of graphene sheets they tend to become entangled and restack which can reduce their effectiveness [74]. Therefore, for the best utilization of the graphene sheets into polymer nanocomposites, full exfoliation and dispersion in the polymer matrix is required. In order to have good interfacial strength with the matrix, good dispersion of the nanosheets in the polymer matrix is required.

The key to prepare advanced graphene-based nanocomposites is the engineering at the polymer-graphene interface [71]. It is very important to know how efficiently the stress is transferred from polymer matrix to the graphene nanofillers [54].

4.5 Strain Effects on Raman bands

Raman spectroscopy is well established diagnostic tool to study the changes in the crystal structure in terms of the phonon. The time independent perturbations such as strain have impact on the Raman bands as the strain modifies the crystal phonons. The effect of applied stress/strain on the crystal symmetry and its phonon frequency are taken as the morphic effects. The impact of these effects on the Raman bands has attracted much attention. The study of the strain dependence of the Raman active bands is very helpful for the basic and applied studies of the graphene. Different vibrational modes were found to be affected differently by the strain depending upon the phonon symmetry in strain component direction e.g. Some of the Raman active modes tend to shift towards lower wavenumbers (redshifts), some tend to shift towards higher wavenumbers (blueshift) and some modes did not show any shifts [31]. Under the morphic (loading) effects the crystal symmetry is altered and the vibration modes that once had the same frequency resulting in the degenerate Raman peaks will have different frequencies and result in separate Raman peaks. The tensile stress induces phonon softening (red shift) and compressibility induces phonon hardening (blue shifts).

Usually it is hard to observe the splitting of the Raman bands by uniaxial strain but the G-band allows one to study strain induced splitting.

The G-band is the prominent and important band of the sp^2 materials due to two basic properties as described in Ref [32]:

- It is present in all sp^2 carbon material Raman spectra at around 1580 cm^{-1}. It is related to the in-plane C-C stretching mode which results in both the optical in-plane transverse (iTO) phonon and the longitudinal optical (LO) phonon branches in the graphitic materials.

- Due to the small mass of carbon atoms and strong C-C bonding, the G-band has a relatively high Raman frequency as compared to other materials and very small change in the Raman frequency can be detected and measured.

Both the iTO and LO phonons have the same frequency at the zone centre of the Brillouin zone as the carbon atoms are neutral. Although the iTO and LO are degenerate at the zone center (Γ) in both graphite and graphene, only the LO phonon mode has a large Raman intensity. Under strain the LO and iTO phonon modes are mixed with each other and both phonons become Raman active. The iTO and LO phonon frequencies split into two peaks and splitting increases with increasing strain. Splitting of the two phonon modes is hard to observe however the G-band high frequency makes it possible to observe a strain induced split. A 1% change in the G-band frequency corresponds to ~16 cm^{-1} which is larger than the natural width of the G-band ~ 10cm^{-1}[32].

4.6 Raman Analysis of the strained Graphene

Due to graphene symmetry, the LO and the iTO modes are degenerate at the Γ point of the Brillouin zone. The applied strain modifies the graphene hexagonal lattice structure by changing the bond lengths and angles in graphene [32]. This symmetry breaking effect in graphene splits the LO and iTO mode frequencies. As a result, the Raman G-band split into two peaks G$^+$ and G$^-$ which represents the longitudinal and transverse atomic motion with the strain direction. These bands are linked to the transverse and longitudinal atomic motions with respect to the strain axis shown in Fig.4.6. The G band splitting with strain as a result of the

74

splitting of the doubly degenerate E_{2g} phonon mode has been studied [27]. The two components G^+ and G^- are reported to show the red shifts with strain.
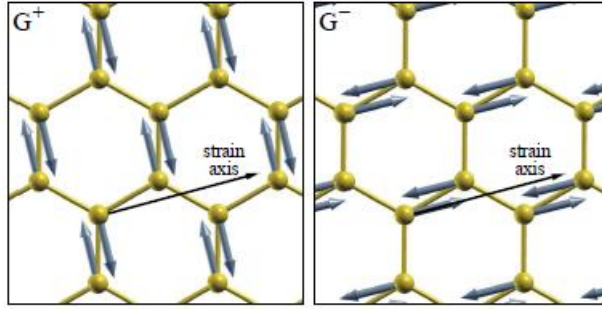
Figure 4.6: Eigenvectors of G+ and G- modes and are perpendicular to the each other. G- polarized along the strain axis and G+ polarized perpendicular to the strain axis [27].

The evolution of the G band in the Raman spectra of a graphene sheet under uniaxial strain is shown in Fig. 4.6 and the measured shifts of G^+ and G^- with uniaxial strain are: $\frac{\partial \omega_{G^+}}{\partial \varepsilon} = -10.8\ cm^{-1}\%\ and\ \frac{\partial \omega_{G^-}}{\partial \varepsilon} = -31.7\ cm^{-1}\%$ for the curves shown inFig. 4.7. The 2D and 2D' bands show red shift but no splitting for small strains as ~ 1.2% [27].
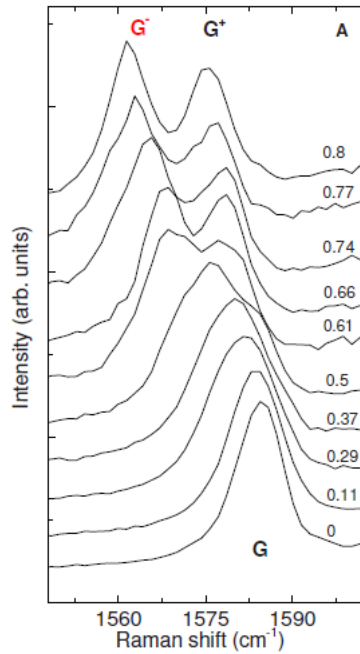
Figure 4.7: G-band as a function of the uniaxial strain that is shown in percentage ranging from 0-0.8. The G-band splits into two subband G^+ and G^- and splitting increases with increasing strain [27].

75

Chapter 5

Graphene under Compressive Strain

5.1 Introduction

In this chapter the study of the compression buckling strain in monolayer graphene flakes of different geometries is discussed. The mechanical response is monitored by the shift of the G and 2D Raman lines with strain, using two different excitation laser wavelengths (514.5nm and 785nm).Graphene being the strongest material with the strength and Young's modulus values of about 160 Gpa and 1 TPa respectively have attracted much interest in various applications. These extraordinary properties can be employed to modify the unique electronic properties of graphene by strain engineering. The strain engineering is very well employed in the silicon device industry to achieve desired functional properties by controlling elastic strain in the material. One more rapidly growing graphene research area is the graphene polymer nanocomposites, which are the polymer matrix composites using graphene as a nanofiller exhibiting enhanced mechanical ,electrical and thermal properties. The study of the mechanical properties of these graphene polymer nanocomposite materials provides significant information about their ability to sustain the external stress and their possible use in the various practical applications. In the present work the experimental study was performed to study the buckling behaviour of the embedded graphene monolayers. The strain is applied using cantilever beam technique and the behaviour of the graphene under tension and compression is monitored by response of the optical phonon. Raman spectroscopy has proven a well employed technique to study the optical phonons and their response to the external changes. The G band and 2D band of the graphene Raman spectra show the non-linear behaviour. Critical buckling strain in monolayer graphene flakes of different geometries is calculated using Euler buckling analysis. Despite the infinitely small thickness of the monolayers, the results show that graphene embedded in plastic beams exhibit remarkable compression bucking strain compared to that of the suspended ones. Due to the effect of the lateral support provided by the polymer matrix, which is indeed dramatic and increases the

effective flexural rigidity of graphene by 6 orders of magnitude. Post strain analysis of the embedded graphene flakes is performed by finding the residual strain in the flakes using Raman spectroscopy.

5.2 Buckling

The introduction of the buckling closely follows the Ref. [77]. Buckling is elastic instability leading to the failure. Buckling is characterized by a sudden failure of a structural member subjected to high compressive stress, where the actual compressive stress at the point of failure is less than the ultimate compressive stresses that the material is capable of withstanding. When load is constantly being applied on a member, such as column, it will ultimately become large enough to cause the member to become unstable. Further load will cause significant and somewhat unpredictable deformations, possibly leading to complete loss of load-carrying capacity. The member is said to have buckled or deformed.

Conventional materials deform or fracture at sample-wide stresses far below the ideal strength, rapid development of nanotechnology need the development of materials with higher strength to sustain large stress. These materials have a good scope in the field of elastic strain engineering where desired properties can be achieved by the controlling the elastic strain and in composite materials. Structural flexibility and buckling behaviour of the carbon nanotubes has been reported [78, 79] showing that the high elastic modulus of the graphite sheet plays a significant role in their mechanical strength. Graphene sheets are stiffer and stronger than any other material [9]. The mechanical properties are predicted to be sensitive to details of the material structure and to the presence of defects so the study of the behaviour of the graphene sheets under compression is important for their particular application.

In order to obtain the critical buckling strain for the graphene we consider the case of the buckling of a rectangular thin plate under uniaxial compression. The critical value of the compressive force in this case is given by classical Euler buckling analysis [81] as:

$$(N_x)_{cr} = K\frac{\pi^2 D}{b^2} \tag{5.1}$$

So the corresponding critical stress value can be evaluated by using the above eq. for the critical load. The value of the critical stress can be employed in Hook's law to obtain the critical strain value given by:

$$\varepsilon_{cr} = K\frac{\pi^2 D}{b^2 C} \tag{5.2}$$

Where

K= geometric constant

b= width of the thin plate

D and C are the flexural rigidity and the tension rigidity

5.3 Experimental Procedure

The experimental procedure to study the compression behaviour of graphene involves the graphene preparation on the plastic substrate, stress application on graphene substrate and Raman analysis of the graphene under strain.

Graphene Making on Plastic/bendable substrates

Following steps were used in preparation of graphene on the plastic substrate:

1. PMMA bar of thickness 3mm was taken.
2. It was wiped with IPA and dried with Nitrogen.
3. The PMMA bar was put in spinner and was spin coated with Su8 2000.5 resist at 4000rpm for 60 seconds.
4. The sample was baked at $95C^0$ in a furnace for 5 minutes.
5. It was put in mask aligner and exposed in UV for 10 sec.
6. The sample was post baked at $95\text{-}110\ C^0$ in a furnace for 10minutes.
7. Developed the sample in EC-solvent for 1 minute.
8. Rinsed with IPA and dried with nitrogen.
9. Water soluble tape was used to put flakes on the PMMA bars.
10. The sample was left for 2 hours under minor stress.
11. Then it was put in water and heated at $90\ C^0$ on hot plate for 10 min.
12. The tape was slowly peeled away from the PMMA bars.
13. Dried with Nitrogen.
14. The sample was baked at $80\ C^0$ in furnace for 5minutes.

15. When the sample cooled down, fresh water soluble tape was put on sample and mechanically peeled to get rid of thick flakes on the PMMA bar.
16. The single layer was identified by optical and Raman analysis.
17. The sample was again spin coated with thin layer of resists (Shipley (S-1805) or PMMA 495).

Sample Making

The samples used in the experiment were prepared by micromechanical cleavage of graphite and putting onto the PMMA (poly methyl methacrylate) bars coated by the ~ 200 nm thick layer of SU-8 photoresist (SU-8 200.5, MicroChem). These graphene samples were coated again by a thin layer of S-1805 (Shipley) or PMMA 495 photoresist on the top. The graphene samples embedded on the top surface of the PMMA bars has a total thickness of 2.9 mm and width 12 mm. Figure 5.1, figure 5.2 and figure 5.3 shows three graphene flakes used in the experiment.
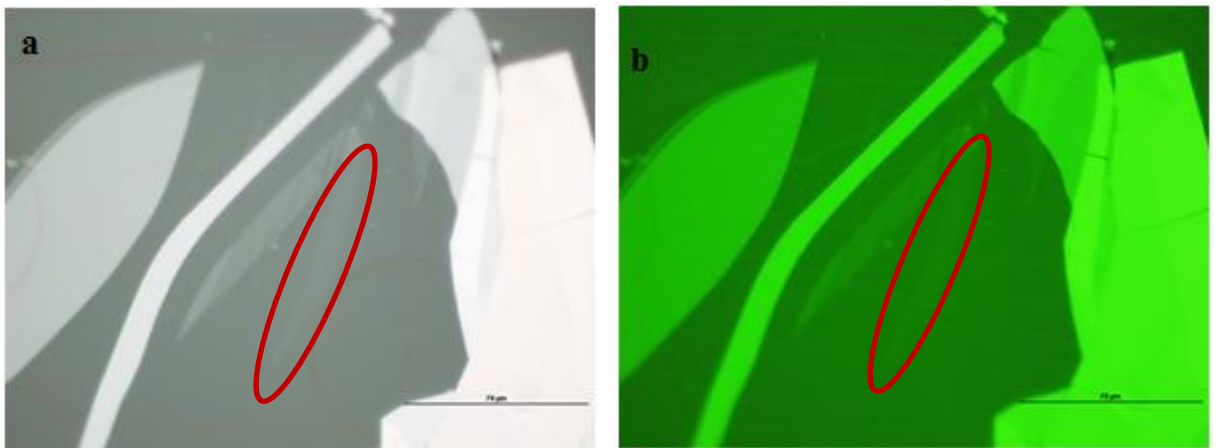
Figure 5.1: (a) Optical image of graphene flake F1on SU-8 coated PMMA bar at 100x (b) Optical image of graphene flake F1on SU-8 coated PMMA bar at 100x with 560 nm optical filter. Scale bar on images indicates 79 µm.
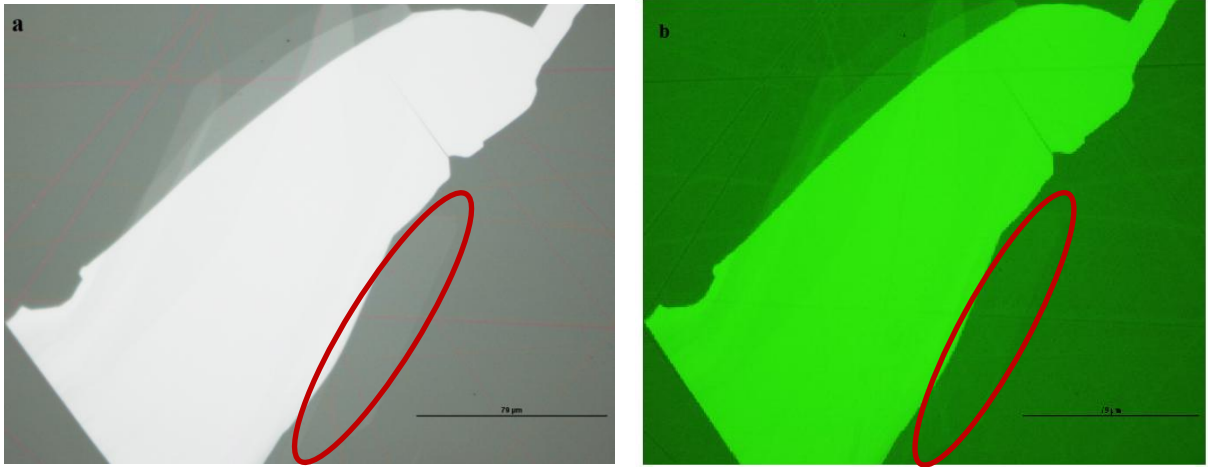
Figure 5.2: (a) Optical image of graphene flake F2 on SU-8 coated PMMA bar at 100x (b) Optical image of graphene flake F2 on SU-8 coated PMMA bar at 100x with 560 nm optical filter
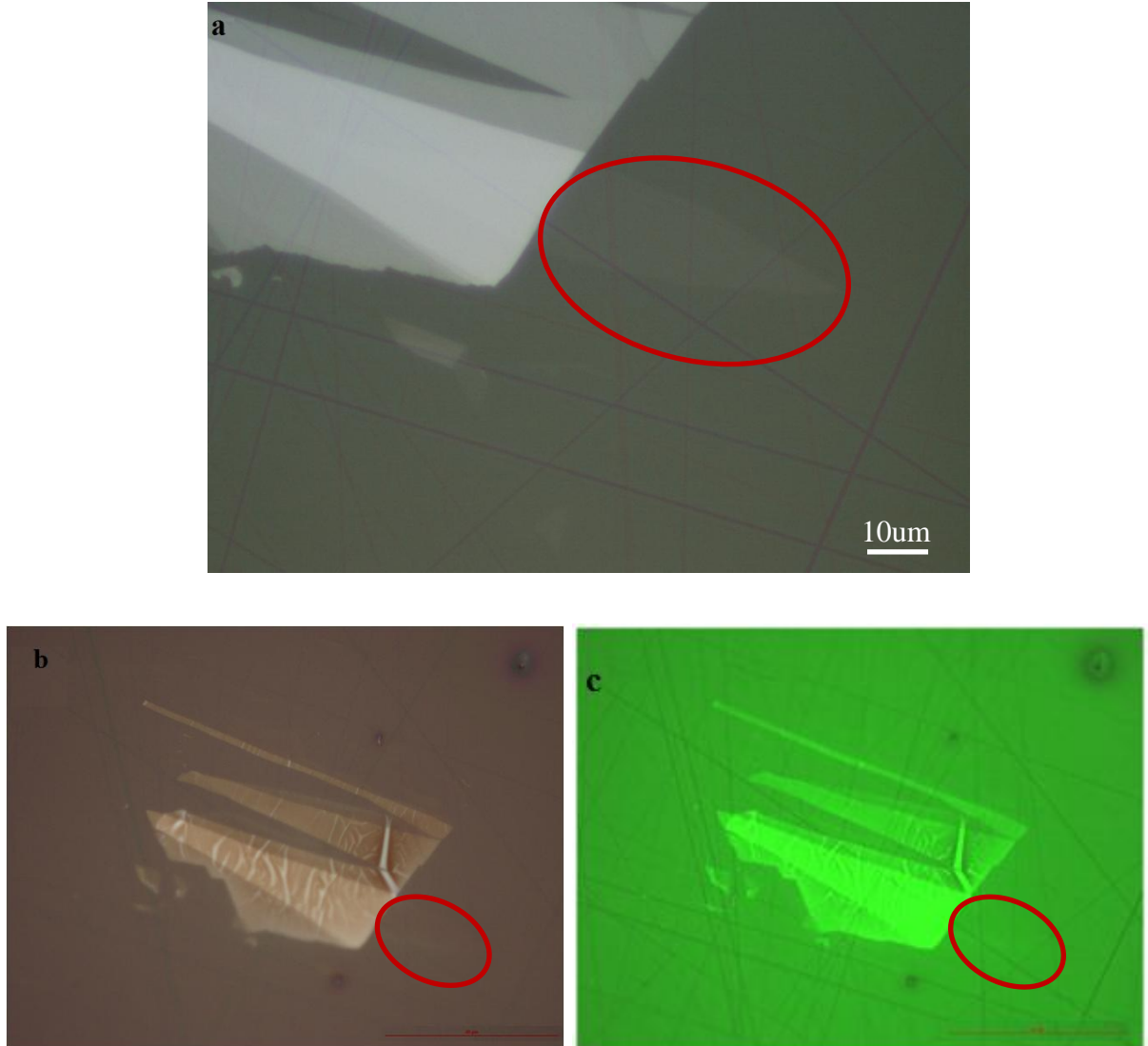
Figure 5.3: (a) Optical image of graphene flake F3 on SU-8 coated PMMA bar at 100x (b) Optical image of graphene flake F3 on SU-8 coated PMMA bar at 50x with PMMA 495 resist coating on the top (c) Optical image of graphene flake F3 on SU-8 coated PMMA bar at 50x with PMMA495 resist coating on the top using 560 nm optical filter.

Strain application

The graphene samples shown in Fig. 5.1-5.3 were subjected to the compression and Raman analysis was performed. The stress was applied smoothly with strain increment of 0.03 or 0.05 % to avoid slippage, and a maximum strain of 0.7% was obtained. A Cantilever beam was employed for the strain analysis of the single layer graphene. The cantilever beam can be flexed up or down by means of an adjustable screw positioned at a distance L = 70.0 mm from the fixed end subjecting the flake to compressive and tensile loads. The graphene flake was located at a distance, x, from the fixed end of 12.97mm and 12.72 mm, resp. The deflection δ was measured accurately using a dial gauge micrometer attached to the top surface of the beam. The experimental arrangement is shown in Fig. 5.4.
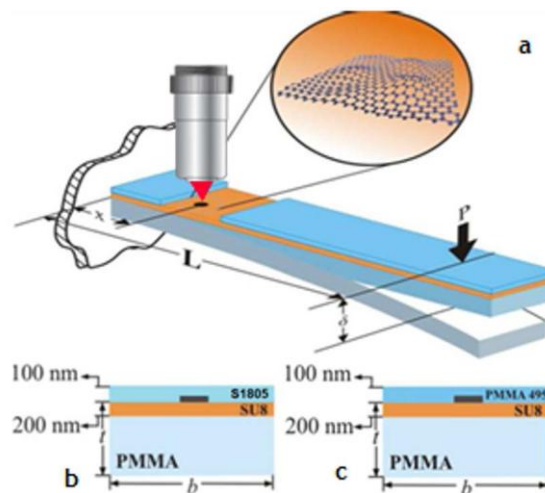
Figure 5.4: (a) Cantilever beam arrangement for (b) flakes F1, F2 and (c) flake F3 [82].

Cantilever Beam Technique

A cantilever beam is a structure which bears the load/stress and deflects a known amount when load is applied to the beam. The beam has two strain gauges, one on the top of the beam and one on the bottom. Figure 5.5 represents the cantilever beam arrangement for stress analysis. The strain is approximately equal and opposite for the two gauges.
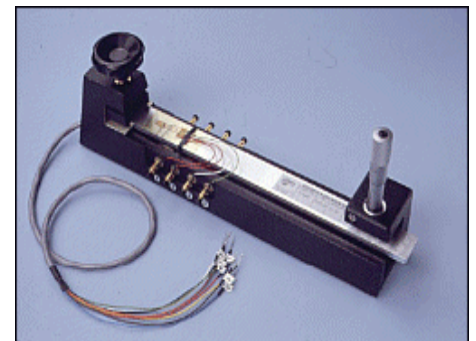
Figure 5.5: Cantilever beam arrangement.
(Image is taken from: www.coursehero.com › Massachusetts)

83

Strain gauge is a valuable tool in the stress analysis applications. It is a transducer which transduces the strain. Strain gauges are small stripes or wires whose resistance change with a change in their dimension when compressed or stretched. The two common types of strain gauge are the resistive metal foil and semiconductor. A typical metal foil strain gauge has a grid-shaped sensing element of thin metallic resistive foil (3 to 6 microns thick) that is sandwiched between a base of thin plastic film (12-16 micron thick)and a covering or lamination of thin film as shown in Fig. 5.6.

The semiconductor strain gauges have silicon chips with a single region of doping to create resistor and usually have higher gauge factor.
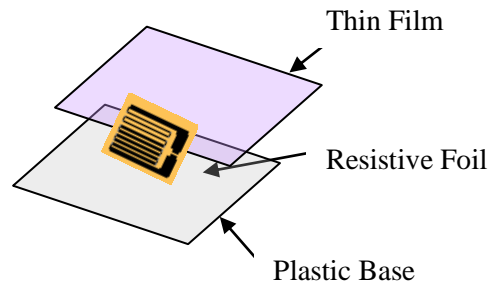
Figure 5.6: Strain gauge construction in a typical cantilever beam arrangement for strain measurement. (Image is taken from: www.me.rochester.edu/courses/ME242/.../A2_StrainGages_2003.do)

A fundamental parameter of the strain gauge is its sensitivity to strain, express quantitatively as the gauge factor (GF). The gauge factor is defined as the ratio of fractional change in electrical resistance to the fractional change in the length (strain).A strain gauge is the unknown resistor in a Wheatstone bridge and is used to observe the oscillations of the beam. Commonly strain gauges are used to measure deflection on beams, columns and small displacements.

The maximum deflection δ of the neutral axis of the beam (elastic behaviour) represented in Fig. 5.7 , is given by the following equation [89].

$$\varepsilon(x) = \frac{3t\delta}{2L^2}\left(1 - \frac{X}{L}\right) \qquad (5.3)$$

where L is the cantilever beam span, δ is the deflection of the beam (at the free end) at each increment of flexure and t is the beam thickness. The position where Raman measurements are taken is denoted by the variable "x".
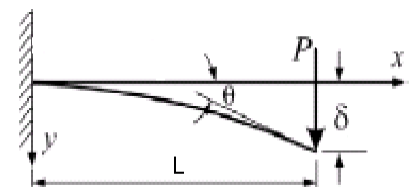
Figure 5.7: Load arrangement in Cantilever beam technique.

Raman Measurements

Raman study was performed to observe the mechanical response of the graphene. Raman spectra were taken using 785 nm (1.58eV) excitation source, while the laser power was kept below 0.85 mW to avoid laser induced local heating on the sample. Raman G and 2D bands were studied as a function of the applied strain and the shift in the G and 2D Raman bands with strain was used to monitor the mechanical response. The nonlinear response of the G and 2D band was observed. G- band splits as a result of the strain into two components G^- and G^+ due to the polarization along the strain axis G^- and perpendicular to the strain axis G^+. The strain rate of both the G band components was determined and their slope analysis $\partial w_G / \partial \varepsilon$ in tension and compression was performed. Raman 2D peak position as a function of the compressive strain for all three flakes was studied. Strain distribution in the graphene flakes is important to study so the Raman mapping on the large flake area using Raman 2D position and full width half maximum (FWHM) was performed. By utilizing the Raman 2D strain analysis, post mortem strain analysis of the graphene flakes was monitored. All the Raman spectra of graphene were Lorentzian fitted.

5.4 Results and Discussion

  The results of this work have been published in *ACS Nano* in 2010. In order to best present our results, the original paper "Compression Behavior of Single-layer Graphene" (**ACS Nano 4(6), 2010, P 3131-3138**) is attached from the next page.

This work presented was carried out in collaboration with several people of different research institutes and universities. My contribution to this work includes the preparation of graphene on bendable (PMMA) substrate by mechanical cleavage and verification of monolayer graphene on PMMA substrate by optical contrast and Raman spectroscopy.

Compression Behavior of Single-layer Graphene

Otakar Frank, Georgia Tsoukleri, John Parthenios, Konstantinos Papagelis, **Ibtsam Riaz**, Rashid Jalil, Kostya S. Novoselov, and Costas Galiotis

Graphene is a two-dimensional crystal, consisting of hexagonally-arranged covalently bonded carbon atoms and is the template for other carbon allotropes [1, 2]. Graphene exhibits a high level of stiffness and strength with Young's modulus values of about 1TPa and strength in excess of 160GPa [3, 4]. It also possesses unique electronic properties, which can be further effectively modified by stress/strain [5, 6]. In fact, strain engineering has been proposed as a route for developing graphene circuits [7] and, in this respect, a precise determination and monitoring of stress and strain are key requirements. Furthermore, there is a growing interest in the exploitation of graphene as a nano-reinforcement in polymer based composites [8-10] for which it is important to know how efficiently the external stress is transferred from the matrix to the nano-inclusions.

Probing the shift of phonon frequencies is an effective way of assessing the degree of stress transfer of a material under an applied stress or strain along a given axis. Raman spectroscopy has proven very successful in monitoring phonons of a whole range of graphitic materials including graphene under uniaxial stress [11-16] or hydrostatic pressure [17,18]. We have recently shown that the position of the 2D peak, ω_{2D}, is related to the applied uniaxial strain, ε, at a rate of approximately -65×10^{-2} cm^{-1} [13, 16]. Past reports of much lower shifts by a number of authors have been attributed [16] to the effect of substrate and/or to the presence of residual strain in the monolayer. The dependence of the G peak position under uniaxial strain has also been the subject of intense interest and, as in the case of the 2D peak; substantial discrepancies have been reported in the literature [12-14]. In the recent work reported by us [13] significant G peak splitting is observed due to the lowering of the E_{2g} phonon symmetry by the imposition of a uniaxial strain.

With a few notable exceptions (see above and e.g. [19-22]), most works dealing with mechanical properties of graphene (see e.g. [6, 7, 23-25]) are of theoretical nature and generally limited to suspended graphene at the atomic scale. Hence, there is a growing

demand for experimental data to validate the models and relate them to graphene attached to various substrates. In the present work, graphene flakes are subjected to a cyclic uniaxial deformation (tension - compression) using the polymer cantilever beam technique. The effect of compressive strain on the doubly degenerate G Raman band is presented for the first time. It was found that for compressive strain of about -0.1% the G band is split in a fashion similar to that observed in tension [13]. The critical strain for graphene buckling was found to be dependent on the flake size and geometry with respect to the strain axis and as such it follows the classical Euler buckling behavior. However, the role of substrate is found to be of a crucial importance, by enhancing the critical buckling strain by several orders of magnitude compared to suspended flakes. Finally, by employing the strain sensitivity of the 2D Raman band *post mortem* strain maps of the flake were constructed. The strain topography on these maps reveals a wrinkling pattern which is established on the flake on the completion of the cyclic deformation. Such patterns are found to be dependent on both the strain axis direction and the flake aspect ratio; a result that should be taken into account in applications such as all-graphene circuits [6].

RESULTS AND DISCUSSION

Graphene monolayers were subjected to compressive and tensile loading by means of a cantilever beam assembly (Fig. 1a). The specimens were embedded into two polymeric layers of SU8 and S1805 and placed onto PMMA bars (Fig. 1a and SI). A detailed description of the experimental set-up and the sample preparation procedure are presented in SI and ref. [16]. Raman sampling was performed *in situ* on different sample locations depicted with crosses in Figs. 1b-d.
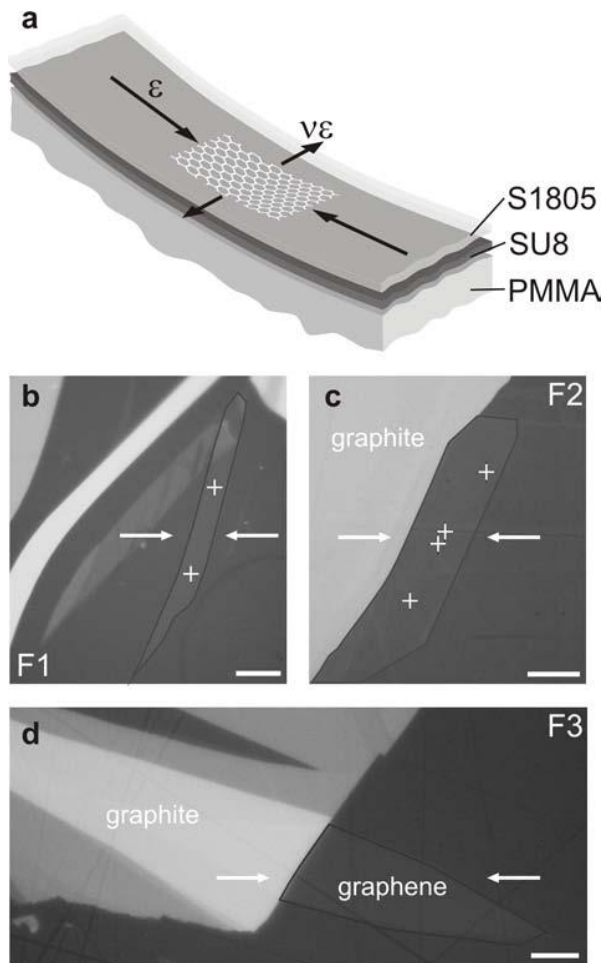
Figure 1. A scheme of the beam bearing the graphene sample under study (a). Optical micrographs of the graphene flakes investigated; flake F1 (b), flake F2 (c) and flake F3 (d). The scale bar is 10 μm and the arrows indicate the strain axis. The crosses in (b) and (c) represent sampling locations.

Figure 2 shows representative Raman spectra of a graphene monolayer in the G peak region as a function of strain recorded on the flake F1 (shown in Fig. 1). Positive (negative) strain values denote data taken under tension (compression). As seen in Fig. 2, the doubly degenerate E_{2g} optical mode (G peak) splits into two components, which have been termed [12,13] G^- and G^+ in analogy with nanotubes, referring to polarization along the strain and perpendicular to it, respectively [12,13]. The most striking feature in Fig.2 is the G peak splitting under both tension and compression; in both cases the E^+_{2g} phonon is perpendicular to the applied strain and thus experiencing smaller softening (redshift) or hardening (blueshift) whereas the E^-_{2g} being parallel to strain is showing much greater rates of shifting in all cases. The rate of shifting of both modes is affected by the Poisson's ratio $\nu=0.33$
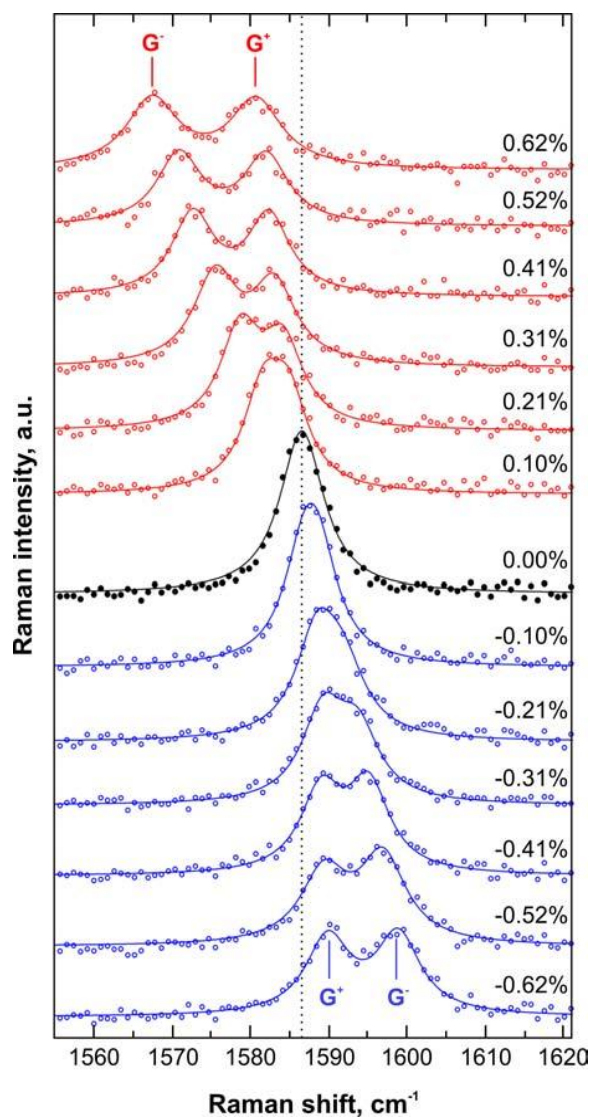
Figure 2. G band Raman spectra of graphene flake excited at 785 nm under uniaxial strain (positive values for tensile and negative for compressive strain). Data were recorded around the center of the flake F1. The original measurements are plotted as points. The solid curves are the best Lorentzian fits to the experimental spectra.

In Figure 3a the G^- and G^+ peak positions (further denoted as Pos (G^-, G^+)) as a function of the compressive strain are shown for flakes F1 and F2. The Pos (G) at zero strain and the slopes $\partial\omega_G^+/\partial\varepsilon$ and $\partial\omega_G^-/\partial\varepsilon$ for all specimens and different experiments are summarized in Table S1 (Supporting Information). The sensitivity of the individual G bands is higher under tension (Table 1), being -31.4 ± 2.8 cm^{-1}/% for the G^- mode and -9.6 ± 1.4 cm^{-1}/% for the G^+. Under compression, the average sensitivities for the two specimens differ. The F1 flake shows 5.5 ± 1.9 cm^{-1}/% for the G^+ mode and 22.3 ± 1.2 cm^{-1}/% for the G^- mode, while the F2 flake exhibits

89

10.1 ± 2.1 and 33.1 ± 2.2 cm^{-1}/% for G$^+$ and G$^-$ modes, respectively. The flake F2 shows $\partial\omega_G/\partial\varepsilon$ values in the linear part of the curves close to zero strain similar to tension, while the F1 flake sensitivities are by ~ 30 % lower. The values extracted in the present study under both tension and compression are given in Table 1. For comparative purposes the reported values in the literature for the slopes $\partial\omega_G/\partial\varepsilon$ under tension are also included.

The issue of residual strain present in the embedded flake is of paramount importance for the mechanical behaviour of graphene as has been shown previously [16, 26, 27]. Especially for the embedded graphene into polymer matrices, the residual strain is due to either the initial deposition process and/or the shrinkage of resin during solidification (curing). The roughness of the polymer substrate may also play a role. The laser Raman technique employed here allows us to identify the presence of residual strain by just measuring the Raman frequency of the embedded flake and compare it to that of an unstressed flake or literature value (e.g. 2680 cm^{-1} for laser excitation at 514 nm). In this work, in order to eliminate the effect of residual strain upon the mechanical data, we selected flakes that exhibited zero or minimal residual strains following a two step methodology. In the first step a Raman mapping is performed that covers a broad area of the flake. The 2D Raman band is then used to generate two separate contour maps whereas the first one presents the topography of the Pos (2D) on the flake and the other the full-width-at-half-maximum (FWHM) of the same flake locations. Based on the fact that the FWHM of the 2D Raman band increases with deformation, the minimum residual strain regions can then be identified by correlating the two topographies; these are the regions where the topography exhibits minimum FWHM values. Even though it is practically impossible to obtain an absolutely prestrain-free monolayer, the small variations in the initial band frequencies observed in our experiments do not seem to affect the measured $\partial\omega/\partial\varepsilon$ at the particular spots. Furthermore, the low prestrain level is evidenced by the linear response of the band sensitivities to tension. As shown previously,
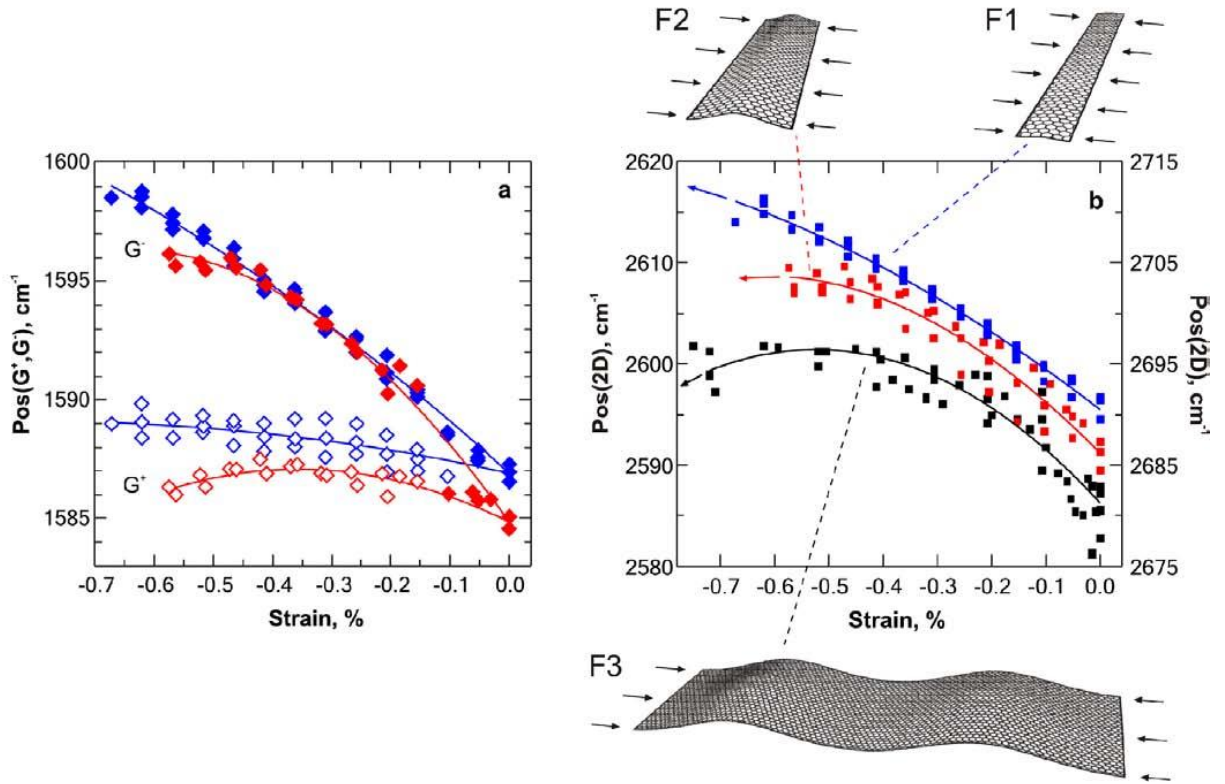
Figure 3. (a) The splitting of G band under compressive strain for F1 (blue) and F2 (red) graphene flakes. Empty and full diamonds indicate the frequency of the G^{+} and G^{-} sub-bands, respectively. Solid lines represent 2nd order polynomial fits where all measurements on a specific flake has been taken into account. (b) Pos(2D) as a function of compressive strain for graphene flakes with different orientations. Blue and red squares belong to F1 and F2 flake, respectively, and are plotted against the left axis. Black squares indicate Pos(2D) for F3 flake and are plotted against the right axis. Data for F3 flake are acquired using 514 nm excitation and reproduced from ref. [16]. Solid lines represent second order polynomial fits to the experimental data. The corresponding graphene flakes are schematically illustrated as rectangular shells with aspects ratios (*l/w*) that correspond to the real ones and schematically indicate the number of half-waves generated by compression (see text). Arrows indicate the compression axis.

Table 1. Summary of $\partial\omega_G/\partial\varepsilon$ values in tension and compression.

	Compression		Tension	
	$\partial\omega_G^{-}/\partial\varepsilon$	$\partial\omega_G^{+}/\partial\varepsilon$	$\partial\omega_G^{-}/\partial\varepsilon$	$\partial\omega_G^{+}/\partial\varepsilon$
	$cm^{-1}/\%$	$cm^{-1}/\%$	$cm^{-1}/\%$	$cm^{-1}/\%$
[14]	--- -	-- 14.2	-	
[12]	---	---	-12.5 ± 2.6	-5.6 ± 1.2
[13]	---	---	-31.7	-10.8
This work	22.3 ± 1.2 [a] * 33.1 ± 2.2 [b] *	5.5 ± 1.9 [a] * 10.1 ± 2.1 [b] *	-31.4 ± 2.8	-9.6 ± 1.4

* the values correspond to the linear part close to zero strain level of the $\omega_G(\varepsilon)$ curves
a – flake F1, b – flake F2

In tension, the Raman wavenumbers of the E_{2g}^{-} and E_{2g}^{+} sub-bands follow almost perfectly linear trends up to the maximum applied strain. However, in compression the linearity holds for strain levels up to 0.3-0.5%. As shown in Fig. 3a, Pos(G^{+}) of F2 reaches a plateau at a strain value of 0.4%, while the $\partial\omega_G^{+}/\partial\varepsilon$ of F1 remains almost constant. Similar differences in behavior of the two flakes can be also detected in the corresponding $\omega_G^{-}(\varepsilon)$ curves. It is worth noting here that the slopes $\partial\omega_{G,}^{-+}/\partial\varepsilon$ in compression evaluated for different mapping locations on a particular flake show small differences that can be attributed to inhomogeneities of the strain field within the flake (Table S1, Supporting Information).

A further insight into the compressive behavior of graphene is provided by the Pos(2D) dependence on compressive strain by comparing previously reported data [16] acquired using an excitation laser line at 514 nm. In Fig. 3b, three distinct sets of experiments for each particular graphene flake are presented. Similarly to the compressive behavior of the G band, Pos(2D) exhibits a non-linear trend with strain for all flakes which can be captured by second order polynomials. The observed $\partial\omega_{2D}/\partial\varepsilon$ is ~+55 cm^{-1}/ % and ~+42 cm^{-1} /% for flake F2 and F1, respectively, at zero strain. For comparison it is recalled that the $\partial\omega_{2D}/\partial\varepsilon$ measured previously using an excitation laser line at 514 nm was +59 cm^{-1} /% [16]. Interestingly it should be noted that in all flakes pos (2D) relaxes after an abrupt uptake. The most strain of the pos (2D) relaxation is at different value for each flake.

The moment of the final failure of the flakes can be expressed by the critical buckling strain (ε_c). For comparison purposes between flakes, we define ε_c as the local maxima in the 2nd order polynomials fitted to Pos(2D) vs. strain values. The ε_c value for F1 flake can be only extrapolated from the polynomial, giving 1.25%. For F2 and F3 flakes which showed clear failure, the ε_c values were estimated at 0.53% and 0.64%, respectively. All compression data are summarized in Table 2.

The critical buckling strain for a flake in the classical Euler regime in air, can be determined through the following equation [28]:

$$\varepsilon_c = \frac{\pi^2 kD}{Cw^2}$$

(1)

where w is the width of the flake, k is a geometric term (see below), and D and C are the flexural and tension rigidities, respectively. A tension rigidity value of 340 GPa nm has been reported by AFM [3] measurements whereas the flexural rigidity has been estimated to 3.18 GPa nm [35, 16]. The above equation (1) is mainly valid for suspended thin films and yields extremely small (~10^{-9}) εc values for graphene monolayers of thicknesses of the order of atomic radii. Such extremely small critical buckling strains are also predicted by molecular dynamics calculations [24] However for embedded flakes the above predictions are meaningless since current and previous experimental results[16] clearly point to much higher values of strain prior to flake collapse.

When embedded in a polymer matrix, the graphene is prevented from full buckling due to the lateral support offered by the surrounding material. At a certain strain the interface between

graphene and polymer should weaken or fail and the flake may buckle as it would do in air. Therefore, assuming that, the different response of the individual graphene flakes to compression can be determined by $\varepsilon_c \propto \dfrac{k}{w^2}$ their geometries and orientation with respect to the strain axis. The geometric term k is dependent on the aspect ratio combined with a number of half waves m into which the flake buckles [28]:

$$k = \left(\frac{mw}{l} + \frac{l}{mw} \right)^2$$

(2)

For the F3 flake, where length (l) = 56 μm and width (w) = 25 μm, 3 half waves are expected to occur at the critical load [28], thus k_{F3} = 4. For flakes F2 and F1, where $l/w < 1$, only one half wave appears, thus k_{F2} = 22.7 and k_{F1} = 89.1. The number of half-waves is illustrated on the respective sketches in Fig. 3b. Accordingly the term $\dfrac{k}{w^2}$ increases from 0.006 μm for F3 flake up to 0.028 μm^{-2} for F1 flake (Table 2). If we now plot the $\dfrac{k}{w^2}$, a linear dependence for the three studied flakes is obtained (Figure 4). The equation of the least-squares-fitted line is given by:

$$\frac{k}{w^2} = a\varepsilon_c + b$$

(3)

where the slope a = -0.03 μm^{-2}.

Since as shown in Figure 4, an Euler type analysis can be applied to the embedded graphene then the critical buckling strain should be given by:

$$\varepsilon_c{}^{embedded} = \frac{k}{w^2} \frac{D^* \pi^2}{C}$$

(4)

where D^* is now the flexural rigidity in the presence of the polymer. With reference to the slope a = -0.03 μm^{-2} in Figure 4, the D^* can be estimated to 12 MPa μm^3, which is, indeed, 6 orders of magnitude higher than the value in air. This is truly a remarkable finding that indicates clearly that the support offered by polymer barriers to a rigid monolayer can provide a dramatic enhancement to its compression behavior. The recently published results [10] showing measurable improvements in the compression behavior of polymers by the addition of graphene at low volume fractions also confirm our findings here. The effect of lateral support can also be deducted from our previously reported results [16] involving a graphene

flake of dimensions, $l = 8$ and $w = 6$ μm, simply laid on top of a substrate. As was shown in ref. 16, the measured $\partial\omega$
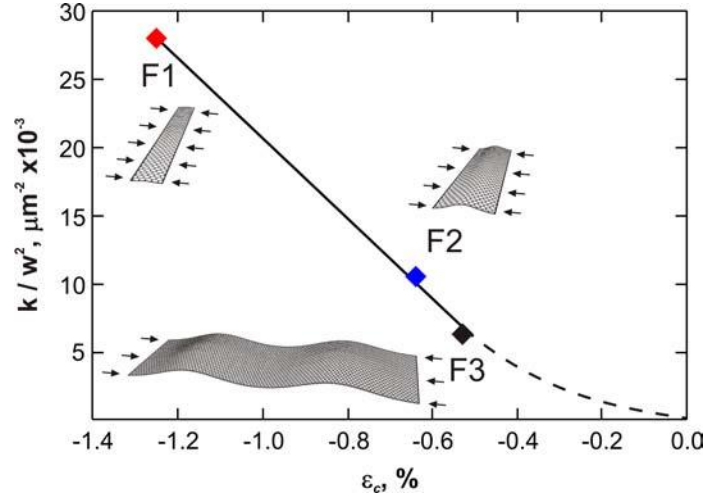
Figure 4. Geometrical term $\dfrac{k}{w^2}$ plotted against critical buckling strain ε when limits to zero. c

for the three flakes under study. The solid line represents a line fit to the obtained experimental points. The dashed line shows the $\dfrac{k}{w^2}(\varepsilon_c)$ possible evolution of when $\dfrac{k}{w^2}$ limits to zero.

Table 2. Critical buckling strain (ε_c), geometrical terms k and k / w^2, and approximate physical dimensions (length l and width w, with l oriented along the strain axis) of the studied graphene flakes.

Sample	ε_c (%)	$k / w2$ (μm-2)	k	l (μm)	w (μm)
F1	-1.25	0.028	89.12	6	56
F2	-0.64	0.011	22.71	11	50
F3	-0.53	0.006	4.02	56	25

It has to be noted that the above described approach of defining the influence of the support, and hence the interaction between the substrate and the graphene flake, by a single term D^{*} is very simplified. Ideally, different stages of the compression process need to be addressed

separately, as described e.g. in [29] to quantify the effect of debonding first, followed by the buckling itself. However, the use of commom phenomenological models is unsatisfactory given the unique nature of 2D memberanes one atom thick, yet macroscopic in lateral dimensions [30]. Similarly, the Euler type buckling observed in the studied flakes is not necessarily universal in the whole $\frac{k}{w^2}$ range. As seen in the Fig.4, the fitted lines does not pass through zero which indicated that its validity for $\frac{k}{w^2} < 5 \times 10^{-3}$ μm^{-2} is questionable. In other extreme case where $l \gg w$ and w is in the nanometer scale, a nonlinear behaviour governed by the matrix effects can be expected too [31]. A further study of this $\frac{k}{w^2}$ region will be essential to assess the mechanical properties of graphene nanoribbons.

Now we come to the FWHM of the peaks studied which provides valuable complementary information on the structural changes in the flake that occur during mechanical loading. The Figure S3 (Supporting Information) shows the G band behavior under compression for a spot in the flake F2. A linear increase of $Pos(G^+,G^-)$ with strain can be observed up to -0.35%, where a subsequent relaxation of the Raman shift values takes place. The FWHM, which is equal for both sub-bands at a given strain level in the whole strain range measured, follows a different evolution. At first, it increases at a rate lower than 2 $cm^{-1}/\%$ and, then, at a strain level of -0.5% increases rapidly, reaching values over 10 cm^{-1} at -0.6%. The rate of broadening in the final stage exceeds 25 $cm^{-1}/\%$. Exactly the same behavior, i.e. rapid broadening at the onset of failure was observed in all compression experiments on flake F2. In contrast, the F1 flake does not show a pronounced FWHM(G) increase. This is in accordance with the almost linear slope of the $\omega_G(\varepsilon)$ curves in F1 sample and the negligible increase of the FWHM(G) under tension, which is less than 2 $cm^{-1}/\%$. Similar dramatic G band broadening is observed on buckled graphene suspended over a trench designed in silicon substrate [32]. In that case, a compression is induced by heating and subsequent shrinkage of graphene due to different thermal expansion coefficient compared to underlying silicon [32].

Figure 5 shows recorded Raman maps from the central part of specimen F2 at rest on the completion of the cyclic loading. Strain levels in Fig. 5a were calculated using the 2nd order polynomial fitted to the Pos(2D) data of the flake F2 as shown in Fig. 3b. Both the 2D band position (Fig. 5a) and FWHM (Fig. 5b) are presented. From Fig. 5a it can be deduced that most of the flake area is under a compressive strain up to -0.3%. As can be clearly seen in Figs 5a and b, Pos(2D) and FWHM(2D) maps point to a graphene monolayer which is not

perfectly flat or at least with an inhomogeneous strain distribution. Indeed, a careful examination of the maps reveals areas with either maximum or minimum Pos(2D) but a significant band broadening in all cases. This is a clear indication of permanent wrinkling formation in the *post-mortem* flakes. Regarding the wrinkling pattern, the orientation of the longer axes of the FWHM isolines (Fig.5b) is approximately parallel to the edge of the neighboring bulk graphite. In the Pos(2D) map, the orientation of the isolines is similar, though more perturbed on the right edge of the graphene flake. The angle between the strain axis and the graphite edge, of about 50°, affects the direction of the formed wrinkles during the loading experiments. The graphite, thus, can act as a "clamp" for controlling the orientation of the wrinkles, which could be a key factor for tailoring the strain field characteristics in graphene-based electronic devices.

CONCLUSIONS

In summary, we documented in detail the response of graphene monolayers to uniaxial strain by probing its optical phonons by Raman spectroscopy. In order to present a complete picture, frequency and FWHM of both G and 2D bands were monitored during tension and compression cycles. Flakes that exhibited minimum residual strain were selected by preliminary mapping. In addition, the linearity of the G and 2D bandshift with tensile strain further confirmed the low pre-strain level of selected flakes. However, in compression the G and 2D band response is non-linear and varies from flake to flake. The corresponding $\partial\omega_{G,2D}/\partial\varepsilon$ values decrease with strain till the eventual turn-over of the slope, which is indicative of progressive buckling that precedes the final collapse of the flake. The gradual decrease of $\partial\omega_{G,2D}/\partial\varepsilon$ is accompanied by an abrupt broadening of the bands, observed particularly in the G mode. The estimated critical buckling strain has been found to depend on size and geometry as would do any thin plate in an Euler buckling regime. It has to be stressed that the critical strain values of the embedded graphene flakes are remarkably high compared to the suspended ones. However, the effect of the lateral support provided by the polymer matrix is indeed dramatic and increases the effective flexural rigidity of graphene by 6 orders of magnitude. Finally, a post-mortem mapping of the flake indicates the presence of permanent wrinkles at an angle dictated by the neighbouring bulk graphite, which acts as a "clamp" supporting one edge of the compressed graphene.

METHODS

Graphene monolayers were prepared by mechanical cleavage from natural graphite (Nacional de Grafite) and transferred onto the PMMA cantilever beam covered by a ~200 nm thick layer of SU8 photoresist (SU8 2000.5, MicroChem). After placing the graphene samples, a thin layer of S1805 photoresist (Shipley) was spin-coated on the top. The beam has a total thickness of $t = 2.9$ mm and width $b = 12.0$ mm. The graphene flake was located at a distance, x, from the fixed end of 12.97 and 12.72 mm, resp. The top surface of the beam can be subjected to a gradient of applied strain by flexing the beam by means of an adjustable screw positioned at a distance $L = 70.0$ mm from the fixed end. The deflection δ was measured accurately using a dial gauge micrometer attached to the top surface of the beam. The validity of this method for measuring strains within the -1.5% to +1.5% strain range has been verified earlier.

MicroRaman (InVia Reflex, Rensihaw, UK) spectra are recorded with 785 nm (1.58eV) excitation, while the laser power was kept below 0.85 mW to avoid laser induced local heating on the sample. A 100x objective with numerical aperture of 0.9 is used, and the spot size is estimated to be ~1x2 µm. The polarization of the incident light was kept parallel to the applied strain axis. Because the graphene peaks overlap with strong peaks originated from the substrate, the spectra were first baseline (linear) subtracted, then normalized to its most intense peak of the substrate at 1450 cm^{-1}, and subsequently the spectrum of bare substrate was subtracted. Figure S1 (Supporting Information) shows the original spectra of bare substrate and unstressed graphene in the G band region, the same free graphene is then shown "as clean" in Fig. 2. All bands in the Raman spectra of graphene were fitted with Lorentzians. The FWHM of the G band for the unstressed graphene was found to be approximately 6-8 cm^{-1}.

The excitation wavelength (785 nm) was chosen with respect to a fluorescence of the polymer matrix embedding the graphene flakes. The fluorescence rendered measurements with lower excitations impossible or at least very difficult. In spite of a lower sensitivity of the CCD camera at higher wavenumbers, the 2D band is still clearly observable and can be evaluated, when the spectra are excited with 785nm laser line. The amplitudes of G and 2D bands of a graphene monolayer are approximately equal in this case. The FWHM of the 2D band in

unstrained flakes was 24-25 cm⁻¹. The 2D linewidths and lineshapes, together with 2D/G relative intensities clearly identify graphene monolayers [34, 35].

The cantilever beam technique has been employed for subjecting tensile/compressive loads to graphene monolayers (see Fig. 1A). The beam can be flexed up or down by means of an adjustable screw subjecting the flake to compressive or tensile loads, respectively. The maximum deflection of the neutral axis of the beam (elastic behaviour), is given by the following equation (for more details see [16]):

$$\varepsilon(x) = \frac{3t\delta}{2L^2}\left(1 - \frac{x}{L}\right)$$

(5)

where L is the cantilever beam span, δ is the deflection of the beam (at the free end) at each increment of flexure and t is the beam thickness. The position where Raman measurements are taken is denoted by the variable "x". For the above equation to be valid, the span to maximum deflection aspect ratio should be greater than 10 [28].

It has to be noted, it is extremely important to apply the stress smoothly in order to ensure reproducibility and no slippage [13]. In our typical experiments, the strain increment was 0.03 or 0.05%. The maximum strain achieved was usually close to 0.7% due to limitations originating mainly from the mechanical response of the substrate. At this strain level, cracks appeared in both underlying SU8 and overlying S1805. Therefore, to minimize the risk of influencing the results by an imperfect stress transfer to graphene or even the danger of irrecoverably damaging the specimen too early, the experiments were stopped at this point. Nevertheless, as shown, the most important features of the behavior of graphene under small strains (<1.5%) can be deduced from its evolution in the range of our experiments. The data presented in this study were measured on two different flakes (on different beams) on several points in each flake (Fig. 1), sometimes in repeated tension and compression cycles. Altogether, more than 100 and 50 spectra were acquired under compression and tension, respectively.
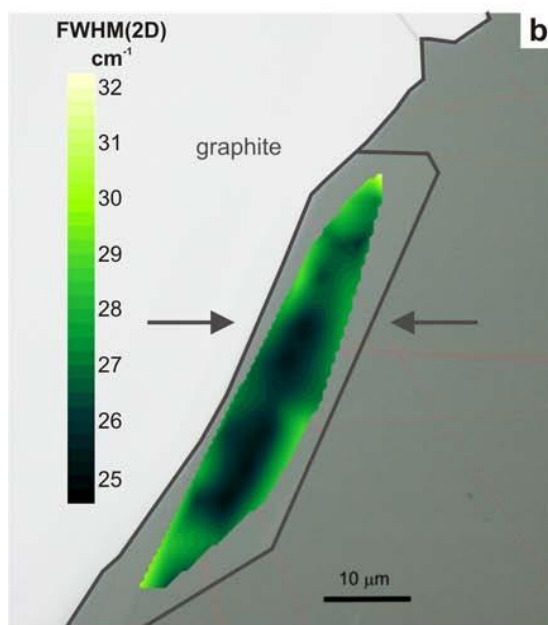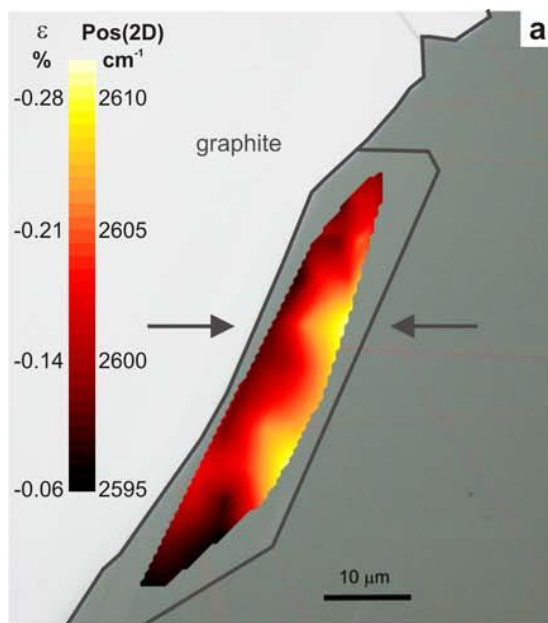
Figure 5. Post mortem (a) Pos(2D) and (b) FWHM(2D) maps of specimen F2 after cyclic loading. The light grey area in both (a) and (b) corresponds to bulk graphite. The arrows indicate the strain direction. See also Figure S4 (Supporting Information) for Pos(G) and FWHM(G) maps on the same flake.

REFERENCES

(1) Geim, A. K.; Novoselov, K. S. The rise of graphene. *Nat. Mater.* **2007,** *6*, 183-191.

(2) Novoselov, K. S.; Geim, A. K.; Morozov, S. V.; Jiang, D.; Zhang, Y.; Dubonos, S. V.; Grigorieva, I. V.; Firsov, A. A. Electric field effect in atomically thin carbon films. *Science* **2004,** *306*, 666-669.

(3) Lee, C.; Wei, X. D.; Kysar, J. W.; Hone, J. Measurement of the elastic properties and intrinsic strength of monolayer graphene. *Science* **2008,** *321*, 385-388.

(4) Zhao, Q.; Nardelli, M. B.; Bernholc, J. Ultimate strength of carbon nanotubes: A theoretical study. *Phys. Rev. B* **2002,** *65*, 144105.

(5) Neto, A. H. C.; Guinea, F.; Peres, N. M. R.; Novoselov, K. S.; Geim, A. K. The electronic properties of graphene. *Rev. Mod. Phys.* **2009,** *81*, 109-54.

(6) Guinea, F.; Horovitz, B.; Le Doussal, P. Gauge fields, ripples and wrinkles in graphene layers. *Solid State Commun.* **2009,** *149*, 1140-1143.

(7) Pereira, V. M.; Neto, A. H. C. Strain Engineering of Graphene's Electronic Structure. *Phys. Rev. Lett.* **2009,** *103*, 046801-4.

(8) Ramanathan, T.; Abdala, A. A.; Stankovich, S.; Dikin, D. A.; Herrera-Alonso, M.; Piner, R. D.; Adamson, D. H.; Schniepp, H. C.; Chen, X.; Ruoff, R. S., et al. Functionalized graphene sheets for polymer nanocomposites. *Nat. Nanotechnol.* **2008,** *3*, 327-331.

(9) Stankovich, S.; Dikin, D. A.; Dommett, G. H. B.; Kohlhaas, K. M.; Zimney, E. J.; Stach, E. A.; Piner, R. D.; Nguyen, S. T.; Ruoff, R. S. Graphene-based composite materials. *Nature* **2006,** *442*, 282-286.

(10) Rafiee, M. A.; Rafiee, J.; Yu, Z. Z.; Koratkar, N. Buckling resistant graphene nanocomposites. *Appl. Phys. Lett.* **2009,** *95*, 223103-3.

(11) Schadler, L. S.; Galiotis, C. Fundamentals and applications of micro-Raman spectroscopy to strain measurements in fibre-reinforced composites. *Int. Mater. Rev.* **1995,** *40*, 116-134.

(12) Huang, M. Y.; Yan, H. G.; Chen, C. Y.; Song, D. H.; Heinz, T. F.; Hone, J. Phonon softening and crystallographic orientation of strained graphene studied by Raman spectroscopy. *Proc. Natl. Acad. Sci. U.S.A.* **2009,** *106*, 7304-7308.

(13) Mohiuddin, T. M. G.; Lombardo, A.; Nair, R. R.; Bonetti, A.; Savini, G.; Jalil, R.; Bonini, N.; Basko, D. M.; Galiotis, C.; Marzari, N., et al. Uniaxial strain in graphene by

Raman spectroscopy: G peak splitting, Grueneisen parameters, and sample orientation. *Phys. Rev. B* **2009,** *79*, 205433-8.

(14) Ni, Z. H.; Yu, T.; Lu, Y. H.; Wang, Y. Y.; Feng, Y. P.; Shen, Z. X. Uniaxial Strain on Graphene: Raman Spectroscopy Study and Band-Gap Opening. *Acs Nano* **2008,** *2*, 2301-2305.

(15) Yu, T.; Ni, Z. H.; Du, C. L.; You, Y. M.; Wang, Y. Y.; Shen, Z. X. Raman mapping investigation of graphene on transparent flexible substrate: The strain effect. *J. Phys. Chem. C* **2008,** *112*, 12602-12605.

(16) Tsoukleri, G.; Parthenios, J.; Papagelis, K.; Jalil, R.; Ferrari, A. C.; Geim, A. K.; Novoselov, K. S.; Galiotis, C. Subjecting a Graphene Monolayer to Tension and Compression. *Small* **2009,** *5*, 2397-2402.

(17) Hanfland, M.; Beister, H.; Syassen, K. Graphite under pressure: Equation of state and first-order Raman modes. *Phys. Rev. B* **1989,** *39*, 12598.

(18) Proctor, J. E.; Gregoryanz, E.; Novoselov, K. S.; Lotya, M.; Coleman, J. N.; Halsall, M. P. High-pressure Raman spectroscopy of graphene. *Phys. Rev. B* **2009,** *80*, 073408-4.

(19) Bunch, J. S.; van der Zande, A. M.; Verbridge, S. S.; Frank, I. W.; Tanenbaum, D. M.; Parpia, J. M.; Craighead, H. G.; McEuen, P. L. Electromechanical Resonators from Graphene Sheets. *Science* **2007,** *315*, 490-493.

(20) Stolyarova, E.; Stolyarov, D.; Bolotin, K.; Ryu, S.; Liu, L.; Rim, K. T.; Klima, M.; Hybertsen, M.; Pogorelsky, I.; Pavlishin, I., et al. Observation of Graphene Bubbles and Effective Mass Transport under Graphene Films. *Nano Lett.* **2008,** *9*, 332-337.

(21) Metzger, C.; Remi, S.; Liu, M.; Kusminskiy, S. V.; Castro Neto, A. H.; Swan, A. K.; Goldberg, B. B. Biaxial Strain in Graphene Adhered to Shallow Depressions. *Nano Lett.* **2009,** *10*, 6-10.

(22) Li, Z.; Cheng, Z.; Wang, R.; Li, Q.; Fang, Y. Spontaneous Formation of Nanostructures in Graphene. *Nano Lett.* **2009,** *9*, 3599-3602.

(23) Atalaya, J.; Isacsson, A.; Kinaret, J. M. Continuum Elastic Modeling of Graphene Resonators. *Nano Lett.* **2008,** *8*, 4196-4200.

(24) Gao, Y.; Hao, P. Mechanical properties of monolayer graphene under tensile and compressive loading. *Phys. E* **2009,** *41*, 1561-1566.

(25) Scarpa, F.; Adhikari, S.; Phani, A. S. Effective elastic mechanical properties of single layer graphene sheets. *Nanotechnology* **2009,** *20*, 065709.

(26) Ferralis, N.; Maboudian, R.; Carraro, C. Evidence of Structural Strain in Epitaxial Graphene Layers on 6H-SiC(0001). *Phys. Rev. Lett.* **2008,** *101*.

(27) Robinson, J. A.; Puls, C. P.; Staley, N. E.; Stitt, J. P.; Fanton, M. A.; Emtsev, K. V.; Seyller, T.; Liu, Y. Raman Topography and Strain Uniformity of Large-Area Epitaxial Graphene. *Nano Lett.* **2009,** *9*, 964-968.

(28) Timoshenko, S. P.; Gere, J. M., *Theory of Elastic Stability*. McGraw-Hill: New York, 1961.

(29) Lanir, Y.; Fung, Y. C. B. Fiber Composite Columns under Compression. *Journal of Composite Materials* **1972,** *6*, 387-&.

(30) Fasolino, A.; Los, J. H.; Katsnelson, M. I. Intrinsic ripples in graphene. *Nat. Mater.* **2007,** *6*, 858-861.

(31) Lourie, O.; Cox, D. M.; Wagner, H. D. Buckling and collapse of embedded carbon nanotubes. *Phys. Rev. Lett.* **1998,** *81*, 1638-1641.

(32) Chen, C.-C.; Bao, W.; Theiss, J.; Dames, C.; Lau, C. N.; Cronin, S. B. Raman Spectroscopy of Ripple Formation in Suspended Graphene. *Nano Lett.* **2009,** *9*, 4172-4176.

(33) Melanitis, N.; Tetlow, P. L.; Galiotis, C.; Smith, S. B. Compressional Behavior of Carbon-Fibers .2. Modulus Softening. *J. Mater. Sci.* **1994,** *29*, 786-799.

(34) Ferrari, A. C.; Meyer, J. C.; Scardaci, V.; Casiraghi, C.; Lazzeri, M.; Mauri, F.; Piscanec, S.; Jiang, D.; Novoselov, K. S.; Roth, S., et al. Raman spectrum of graphene and graphene layers. *Phys. Rev. Lett.* **2006,** *97*, 187401.

(35) Malard, L. M.; Pimenta, M. A.; Dresselhaus, G.; Dresselhaus, M. S. Raman spectroscopy in graphene. *Phys. Rep.* **2009,** *473*, 51-87.

Compression Behavior of Single-layer Graphene

Otakar Frank, Georgia Tsoukleri[1], John Parthenios, Konstantinos Papagelis, **Ibtsam Riaz,** Rashid Jalil, Kostya S. Novoselov, and Costas Galiotis

Supporting Information

Raman study of graphene - background

The recently developed method for graphene preparation by micromechanical cleavage of graphite[1] provides an opportunity for studying the Raman band shifts of both G and 2D modes [2,3] upon tensile or compressive loading at the molecular level [4-9] This is important not only for highlighting the extreme strength and stiffness of graphene but also to link its behaviour with the mechanical deformation of other graphitic structures such as bulk graphite, carbon nanotubes (CNT) and CF. The G peak corresponds to the doubly degenerate E_{2g} phonon at the Brillouin zone centre. The D peak is due to the breathing modes of sp_2 rings and requires a defect for its activation [2, 3, 10]. It comes from TO phonons around the **K** point of the Brillouin zone, is active by double resonance[11] and is strongly dispersive with excitation energy due to a Kohn Anomaly at **K** [12]. The 2D peak is the second order of the D peak. This is a single peak in monolayer graphene, whereas it splits in four in bilayer graphene, reflecting the evolution of the band structure [2,3] .Since the 2D peak originates from a process where momentum conservation is obtained by the participation of two phonons with opposite wavevectors it does not require the presence of defects for its activation, and is thus always present. Indeed, high quality graphene shows the G, 2D peaks, but not D.
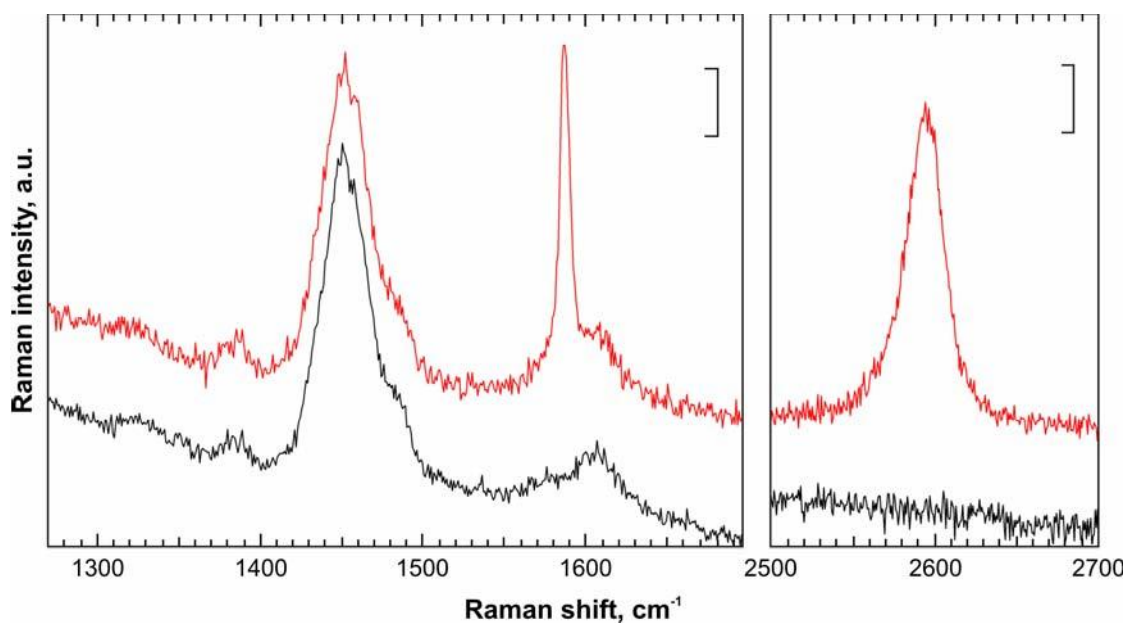
Figure S1. Original Raman spectra excited by a 785 nm laser of the combined SU8 and S1805 substrate (black) and a graphene flake embedded within this substrate (red). The spectra are offset for clarity, and scale bars represent 500 counts in both panels.
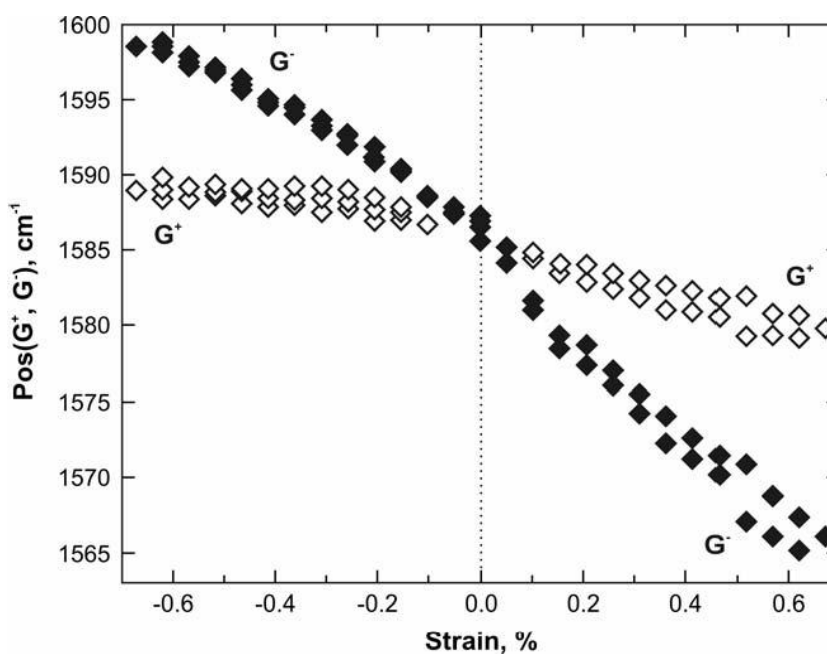
Figure S2. Plot of G band positions as a function of strain from experiments conducted of flake F1 (Figure 1c, main text). Strain with positive (negative) values indicates tension (compression). Full end empty diamonds indicate the frequency position of the G- and G+ sub-bands.
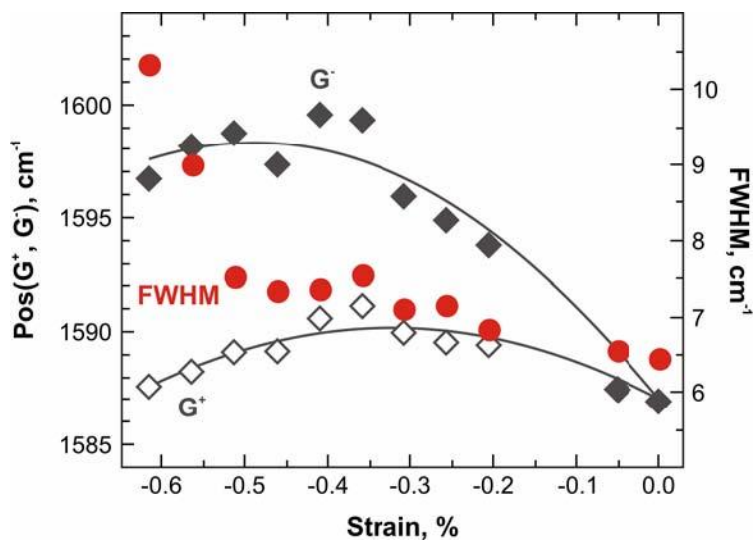
Figure S3. Plot of G- and G+ band positions and their FWHM as a function of strain on a selected spot on flake F2 (Fig. 1c, main text). Full circles indicate the bands FWHM (right axis), full (empty) diamonds show the position of the G- (G+) sub-bands. Only one set of FWHM is presented, since both sub-bands have the same width for a given strain level. Solid (dashed) lines are 2nd order polynomial fits of the G-(G+) band position measurements.
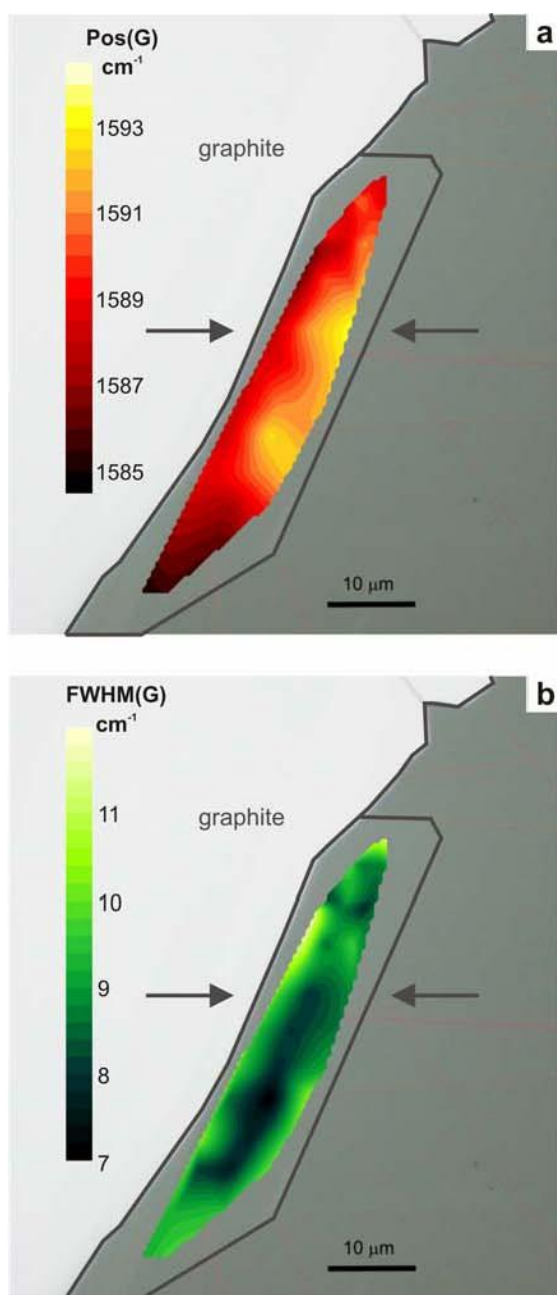
Figure S4. Post mortem (a) Pos(G) and (b) FWHM(G) maps of specimen F2 after cyclic loading. The band was fitted as a single Lorentzian. The light grey area in both (a) and (b) corresponds to bulk graphite. The arrows indicate the strain direction.

		a0	a1	G- a2	a1	G+ a2
F1						
	1	586.9	- 22.5 ± 0.9	-5.9 ± 1.8	-1.8 ± 1.0	1.4 ± 1.9
	2	587.3	-18.8 ± 0.8	-2.5 ± 1.6	-4.0 ± 0.9	-1.94 ± 1.7
	3	586.5	-25.2 ± 1.0	-9.9 ± 2.0	-10.5 ± 1.2	-9.54 ± 2.4
F2						
	1	585.1	-36.1 ± 1.8	-28.9 ± 3.8	-12.2 ± 0.8	-17.14 ± 1.6
	2	584.6	-34.1 ± 2.8	-24.1 ± 6.1	-13.0 ± 1.4	-18.2 ± 3.1
		583.3	-28.4 ± 1.0	-13.0 ± 2.2	-4.5 ± 1.0	-0.7 ± 2.2

	2D a0	a1	a2
F1			
	956.5	-38.0 ± 2.1	-10.3 ± 4.1
	596.6	-36.6 ± 3.4	-13.5 ± 6.3
	594.6	-41.7 ± 3.2	-12.6 ± 6.4
F2			
	592.3	-59.8 ± 4.5	-52.4 ± 9.8
	591.3	-60.1 ± 7.6	-54.8 ± 16.6
	598.4	-45.4 ± 7.8	-19.9 ± 17.2

Table S1. Coefficients of 2nd order polynomial curves fitted to the Raman G_+, G_- and 2D bands evolution with compressive strain. The fit equation can be written: $\omega = a_0 + a_1 |\varepsilon| - a_2 \varepsilon^2$. Thus $a_0 = \omega_0$ (cm^{-1}), a_1 corresponds to the strain sensitivity $\partial_{G,2D}/\partial\varepsilon$ (cm^{-1}/%) close to zero strain, and a_2 expresses the curvature of the slope $\partial_{G,2D}/\partial\varepsilon^2$ (cm^{-1}/%^{2}). The ± sign prefaces a value of 95% confidence interval.

Supporting Information References

1. Novoselov, K. S.; Geim, A. K.; Morozov, S. V.; Jiang, D.; Zhang, Y.; Dubonos, S. V.; Grigorieva, I. V.; Firsov, A. A. *Science* **2004,** *306* (5296), 666-669.

2. Ferrari, A. C.; Meyer, J. C.; Scardaci, V.; Casiraghi, C.; Lazzeri, M.; Mauri, F.; Piscanec, S.; Jiang, D.; Novoselov, K. S.; Roth, S.; Geim, A. K. *Phys. Rev. Lett.* **2006,** *97* (18), 187401. 3. Malard, L. M.; Pimenta, M. A.; Dresselhaus, G.; Dresselhaus, M. S. *Phys. Rep.* **2009,** *473* (5-6), 51-87.

4. Huang, M. Y.; Yan, H. G.; Chen, C. Y.; Song, D. H.; Heinz, T. F.; Hone, J. *Proc. Natl. Acad. Sci. U.S.A.* **2009,** *106* (18), 7304-7308.

5. Mohiuddin, T. M. G.; Lombardo, A.; Nair, R. R.; Bonetti, A.; Savini, G.; Jalil, R.; Bonini, N.; Basko, D. M.; Galiotis, C.; Marzari, N.; Novoselov, K. S.; Geim, A. K.; Ferrari, A. C. *Phys. Rev. B* **2009,** *79* (20), 205433-8.

6. Ni, Z. H.; Yu, T.; Lu, Y. H.; Wang, Y. Y.; Feng, Y. P.; Shen, Z. X. *Acs Nano* **2008,** *2* (11), 2301-2305.

7. Proctor, J. E.; Gregoryanz, E.; Novoselov, K. S.; Lotya, M.; Coleman, J. N.; Halsall, M. P. *Phys. Rev. B* **2009,** *80* (7), 073408-4.

8. Yu, T.; Ni, Z. H.; Du, C. L.; You, Y. M.; Wang, Y. Y.; Shen, Z. X. *J. Phys. Chem. C* **2008,** *112* (33), 12602-12605.

9. Tsoukleri, G.; Parthenios, J.; Papagelis, K.; Jalil, R.; Ferrari, A. C.; Geim, A. K.; Novoselov, K. S.; Galiotis, C. *Small* **2009,** *5* (21), 2397-2402.

10. Tuinstra, F.; Koenig, J. L. *The Journal of Chemical Physics* **1970,** *53* (3), 1126-1130.

11. Maultzsch, J.; Reich, S.; Thomsen, C. *Phys. Rev. B* **2004,** *70* (15), 155403.

12. Piscanec, S.; Lazzeri, M.; Mauri, F.; Ferrari, A. C.; Robertson, J. *Phys. Rev. Lett.* **2004,** *93* (18).

5.5 Conclusion

Compression behaviour of graphene monolayers embedded in polymer substrate is studied. Raman spectroscopy is used to observe the response of the graphene flakes under uniaxial strain. The nonlinear behaviour of the G and 2D band is observed and studied in detail for graphene flakes of different geometries. The estimated critical buckling strain for the graphene flakes was found by Euler buckling analysis and show a strong dependence on the size and geometry of the graphene monolayers. Compared to the suspended graphene monolayers the high values of critical buckling strain for embedded flakes explain that the graphene monolayers embedded in polymers can provide reinforcement in compression to high values of strain. This is very significant for the development of graphene nanocomposites that can provide enhanced buckling stability for structural applications.

Chapter 6

Boron Nitride: A Two Dimensional Insulator

6.1 Introduction

The classification of materials as 0D,1D, 2D or 3D plays an important role in the material characteristics, hence material properties are strongly dependent on dimensionality [83, 86]. The missing class of 2D materials has been theoretically studied for many years but all experimental efforts to obtain 2D materials have ended up in thermodynamically unstable thin films .In this new class of two dimensional materials graphene was the first ever real material obtained in 2004 [17]. Boron nitride is another material which has a layered structure and its atomic planes can be easily separated by using the same technique of mechanical cleavage as used for the graphite to prepare graphene [17,83]. Boron Nitride is the compound of Boron and Nitrogen and is synthetically produced. Boron Nitride is isoelectronic to carbon and has two major allotropes: hexagonal boron nitride (hBN) which is similar to graphite and cubic boron nitride (cBN) that resembles diamond [84]. Both forms have boron and nitrogen as building blocks but have distinct crystalline structure on the basis of the arrangement of these atoms. Hexagonal boron nitride has a honeycomb lattice arrangement. Each atom, Boron (nitrogen), is covalently bonded to three nitrogen (boron) atoms in the plane making an angle 120° between the bonds. Therefore the in-plane strong covalent bond with short length is the same as in graphite.
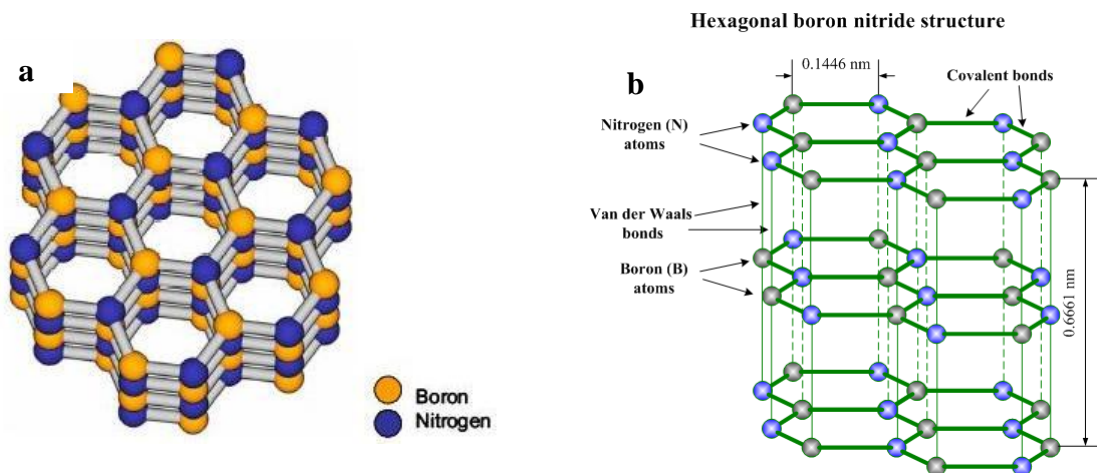

Figure 6.1: Crystal structure of hexagonal Boron Nitride (a) Honeycomb arrangement of boron and nitrogen atoms in the lattice structure (b) Stacking of the atomic planes of hexagonal boron nitride. (Image in Fig. 6.1(b) is taken from: http://www.substech.com/dokuwiki/doku.php?id=boron_nitride_as_solid_lubricant)

It has AA′ stacking with boron and nitrogen atoms on top of each other [85] as shown in Fig. 6.1. The stacking is thus different from graphite's AB Bernal stacking which has the same planar arrangement but offset planes so that only half the carbon atoms have neighbors directly above and directly below [87] as shown in Fig. 6.2. The lattice constant values for boron nitride as indicated in the figure 6.1 are very close to the graphite lattice constant values (hBN lattice constant is only 1.7% larger than graphene). The layered structure of the hBN planes are weakly bonded by the Van der Waals forces, the same as for the graphite planes. The strong in-plane covalent bonding of boron and nitrogen atoms and weak bonding between the planes gives anisotropy in boron nitride.
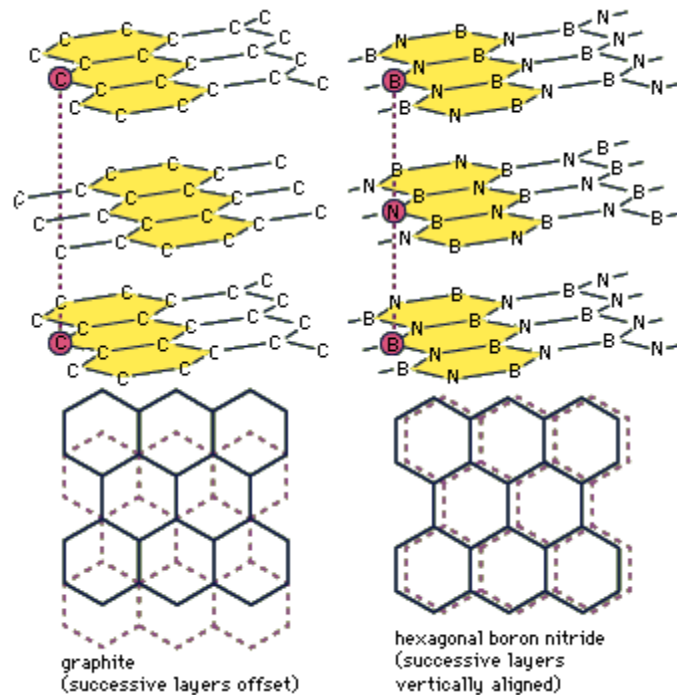
Figure 6.2: Comparison of the hexagonal structures of graphite (left) and boron nitride (right). The AA′ stacking in boron nitride structure with boron and nitrogen atoms on top of each other is different from AB Bernel's stacking in graphite having carbon atoms planes at an offset.

(Boron nitride: hexagonal structures [Art] In *Encyclopædia Britannica*. Retrieved from http://www.britannica.com/EBchecked/media/9370/Comparison-of-the-hexagonal-structures-of-graphite-and-boron-nitride)

In spite of the many structural similarities, graphite and hBN have different electronic properties. No free electrons are present in the hBN for conduction because the P_z orbitals in boron atoms are vacant whereas in nitrogen atoms, they are occupied by the neighbouring electrons. Thus, there are no electrons free to overlap and form π bonds thus giving boron nitride an insulating character [85]. Contrary in graphite the fourth valence

electron is paired with the other electron of the adjacent plane by π bonds, what is therefore responsible for the high conductivity.

The wide range of boron nitride properties e.g an electric insulator of large band gap of ~ 5.9 eV [88],chemically and thermally stable and mechanically strong, makes it a possible candidates for nanosize electronic devices [89].

Among the non-carbon nanotubes, boron nitride nanotubes were studied as the structural analogue of carbon nanotube which are metallic or semiconducting whereas the boron nitride nanotubes are the insulating, chemical stable, mechanically robust and thermally conductive [89]. Similarly, the single layer of graphene is the analogue of the single layer of hBN. Since the discovery of graphene ('sister' material of boron nitride), it has attracted a lot of interest due to its unusual electronic band structure and the nature of its charge carriers that results in high mobility and other exceptional quantum phenomena at room temperature [2, 18, 20]. The lack of interest in boron nitride can be due to the fact that monolayer boron nitride has not been obtained and identified because of the unavailability of bulk hBN for mechanical cleavage and the difficulty in obtaining large layers (20-100 micron).

To utilize the properties of boron nitride layers in practical applications boron nitride layers need to be isolated from the bulk boron nitride and in this work demonstrate that we are able to obtain and identify large boron nitride few layers .

The lack of atomically flat substrates for graphene limits the high mobility of graphene charge carriers and is a hindrance in the more detailed experimental study of the properties of graphene, graphene physics near Dirac point and also device applications of graphene [90]. The most commonly used substrate for the graphene is Si/SiO_2 which is not an ideal substrate for graphene due to charge impurities [91, 92] and high roughness of the surface [93]. Graphene requires an inert substrate for high quality graphene devices. Recently boron nitride was used as a substrate for high quality graphene based electronic devices [68]. In addition to a better substrate for graphene boron nitride has also been used as:

(1) the top dielectric to gate graphene [94] and (2) thin insulator to separate graphene layers in graphene-boron nitride heterostructures [107].

This chapter represents the work of large boron nitride layers preparation, identification and analysis using optical and Raman signatures.

6.2 Experimental Method

The hBN crystal as shown in the Fig. 6.3 was mechanically peeled to prepare hBN thin layers by using the standard method of cleavage [3].
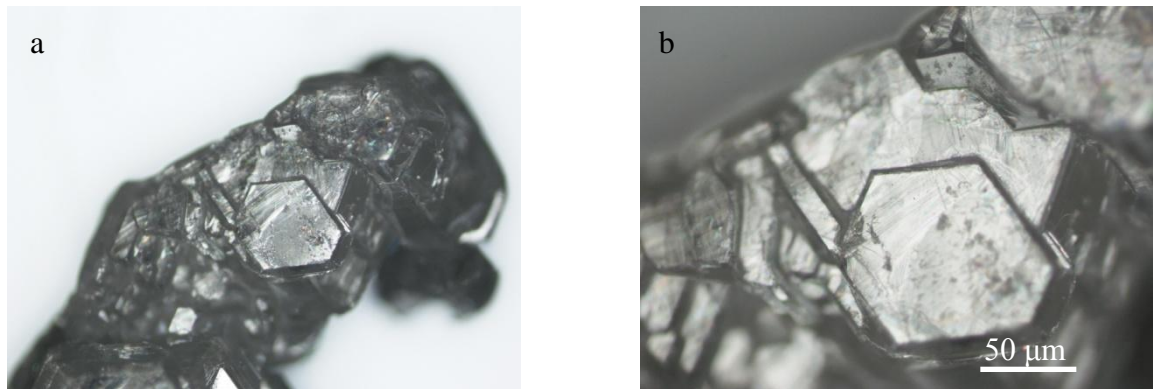
Figure 6.3: Optical image of the bulk hexagonal boron nitride (a) at 20x (b) at 50x.

A clean Si/SiO$_2$ wafer was used as substrate to prepare hBN. The schematic of the standard cleavage procedure is shown in Fig. 6.4.
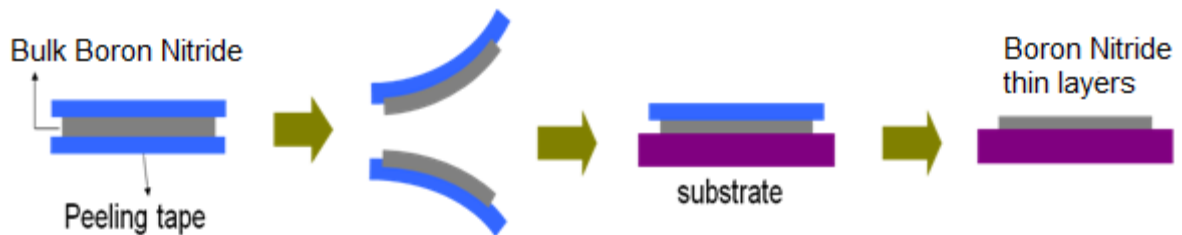
Figure 6.4: Schematic illustration of the mechanical cleavage of the boron nitride using sticky tape

Thin layers of boron nitride (BN) prepared on the oxidized silicon substrates show very little contrast due to zero opacity [25]. Monolayer boron nitride on ≈300nm Si/SiO$_2$ shows <1.5% white light contrast and makes it undetectable by human eye. Silicon wafers of different oxide thickness were used to find the maximum optical contrast conditions.
Figure 6.5 is the optical image of BN thin layers on 290nm Si/SiO$_2$ at 50x with and without 560 nm green optical filter.
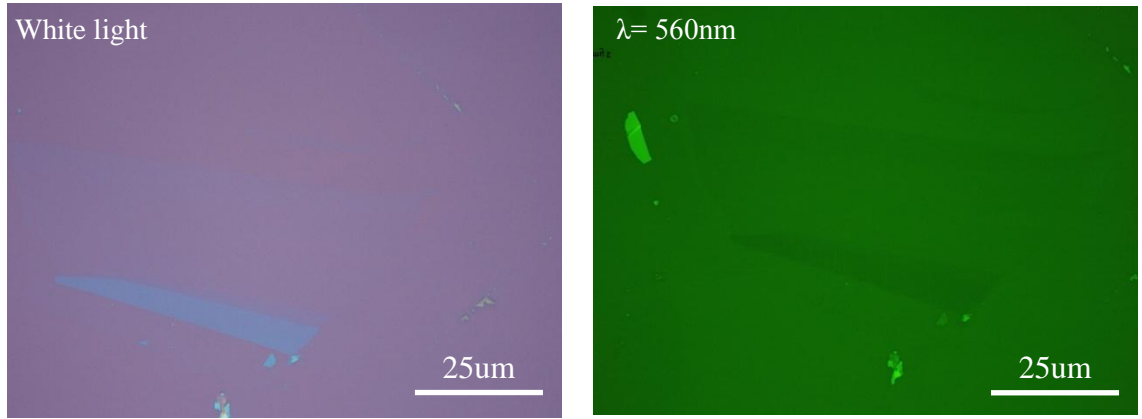
Figure 6.5: Optical image of the BN layers on 290nm Si/SiO$_2$ at 50x with white light and 560 nm optical filter .

Although AFM is a low-throghput technique, is also used here as a mean to confirm the thickness of BN layers. The thickness of different regions of the BN layers was identified by AFM are shown in Fig. 6.6 (b).
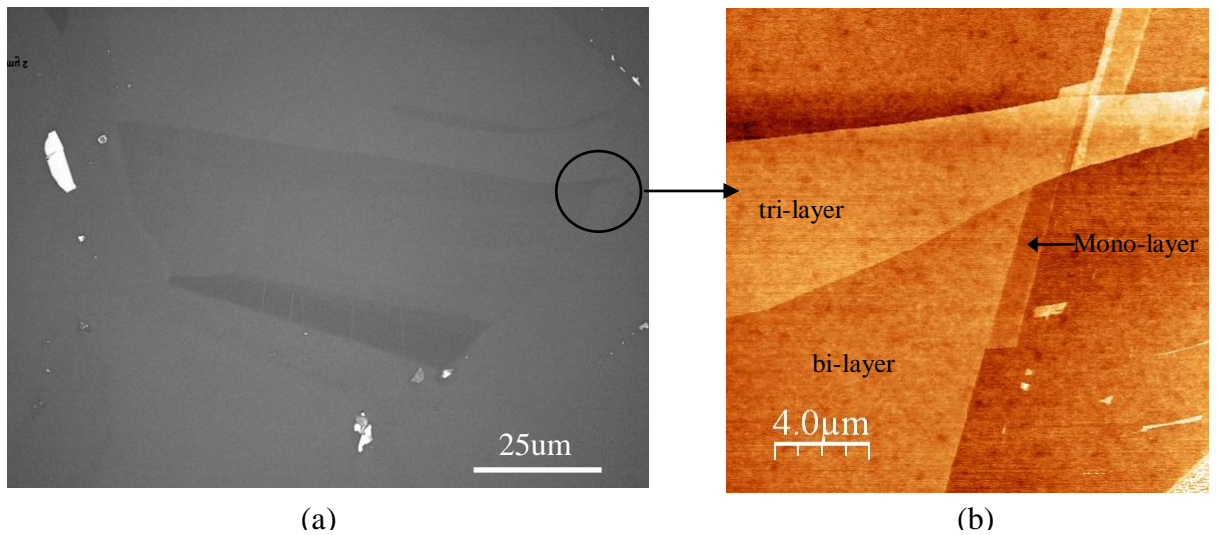
Figure 6.6: (a) Optical image of BN layers with contrast enhanced by a factor of 2 (b) AFM identified BN regions of different thickness.

Raman spectroscopy was another tool used to identify the number of BN layers. The Raman active peak of the BN was observed at ≈1366 cm^{-1}. Raman spectra for single, bi and tri layers of BN are shown in Fig. 6.7. The BN peak intensity was found to be proportional to the number of BN layers; therefore as the number of BN layers decreases the BN peak becomes weaker as in Fig. 6.7. the Raman peak shift for BN layers was also

observed and it was found that the monolayers shift upward whereas bilayer and other thick BN layers shift downwards with respect to the bulk BN peak position.
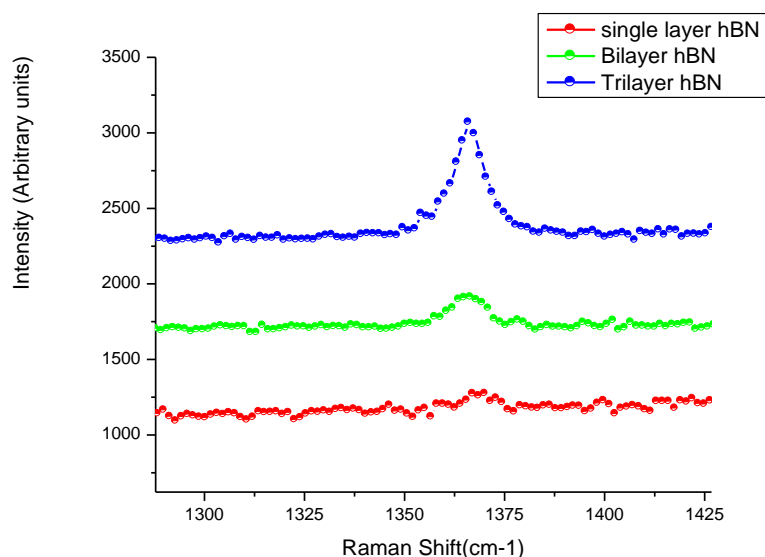
Figure 6.7: Raman spectra of single, bi and tri layer of BN. The intensity of the peak changes with the number of BN layers.

SEM images of the BN flake shown in Fig. 6.8 were taken. Figure 6.8 represents the different regions of the BN observed in the SEM.
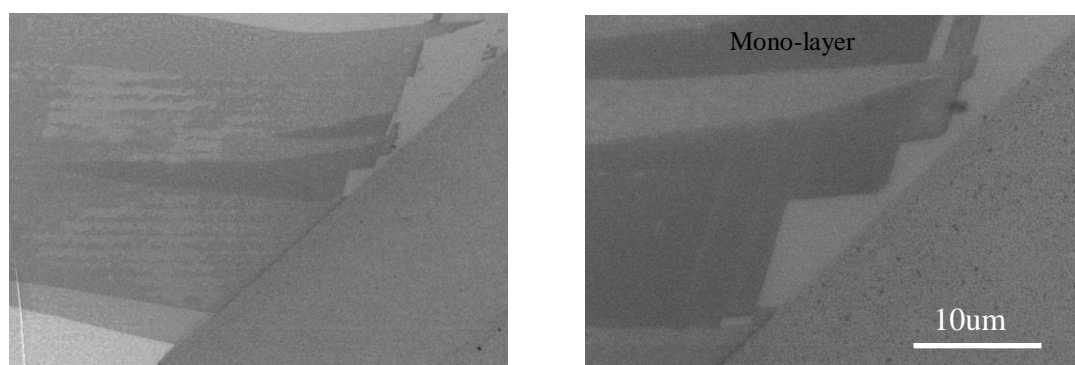
Figure 6.8: SEM image of the BN regions of different thickness.

In order to find the better optical contrast for BN layers, BN flakes were also prepared on the 90nm Si/SiO$_2$ thickness. By optical contrast analysis at different wavelengths it was observed that BN show both positive and negative contrasts at longer and shorter wavelengths by changing the sign at $\approx$ 530 nm. The optical and AFM analysis of the BN layers on 90 nm Si/SiO$_2$ is shown in Fig. 6.9-6.11.

116
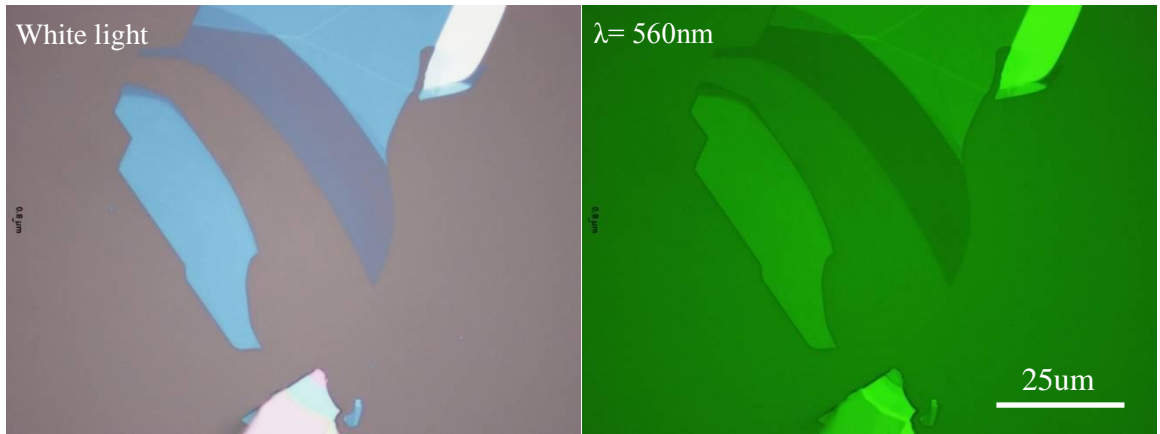
Figure 6.9: Optical image of BN layers on 90 nm Si/SiO$_2$ at 100x with white light and 560 nm optical filter.
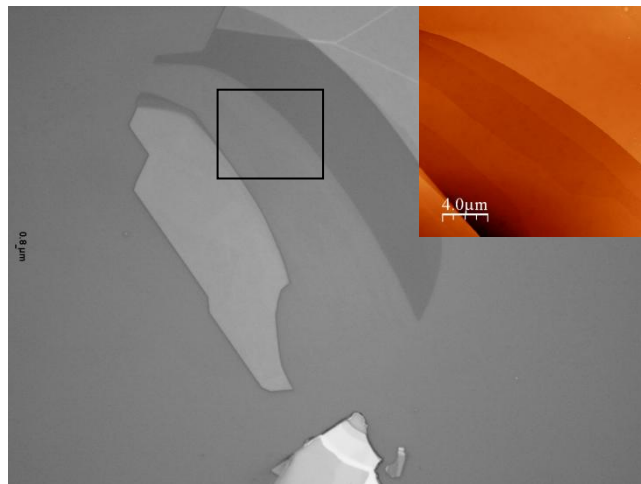
Figure 6.10: Contrast enhanced image of the BN layers on 90 nm Si/SiO$_2$ .Inset of the figure is an AFM image of the BN region in square.

The identified monolayer BN layer showed a step height of ~0.38 nm in the AFM height profile. Figure 6.11 shows the AFM analysis of the BN layer indicated by the square region. The AFM image of the BN flake shows the smooth and clean surface of the BN flakes that makes it ideal for graphene substrates and top gates in graphene based devices.

Step height ~ 0.38 nm
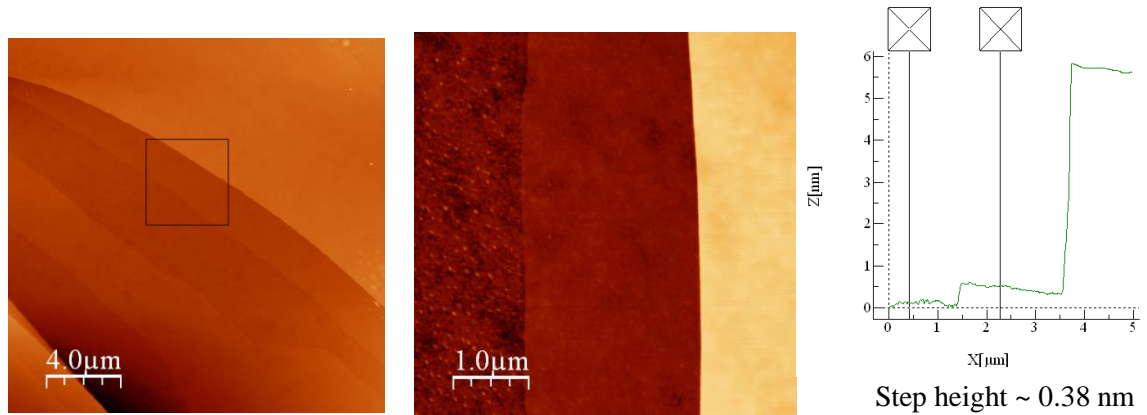
Figure 6.11: AFM image of the BN regions on 90 nm Si/SiO$_2$ wafer. The topographic scan and height profile of region in the square is shown in the second and third images from the left.

BN layers were also made on 72nm Si/SiO$_2$ wafers. For this purpose 90 nm Si/SO$_2$ was taken and etched in KOH solution at 70 C^0. An oxidized silicon wafer (90 nm silicon oxide) was etched for about 10-11 minutes to get the required thickness (72 nm) of oxide. The etching rate and resulting oxide contrast is shown in Fig. 6.12.

(a)   (b)
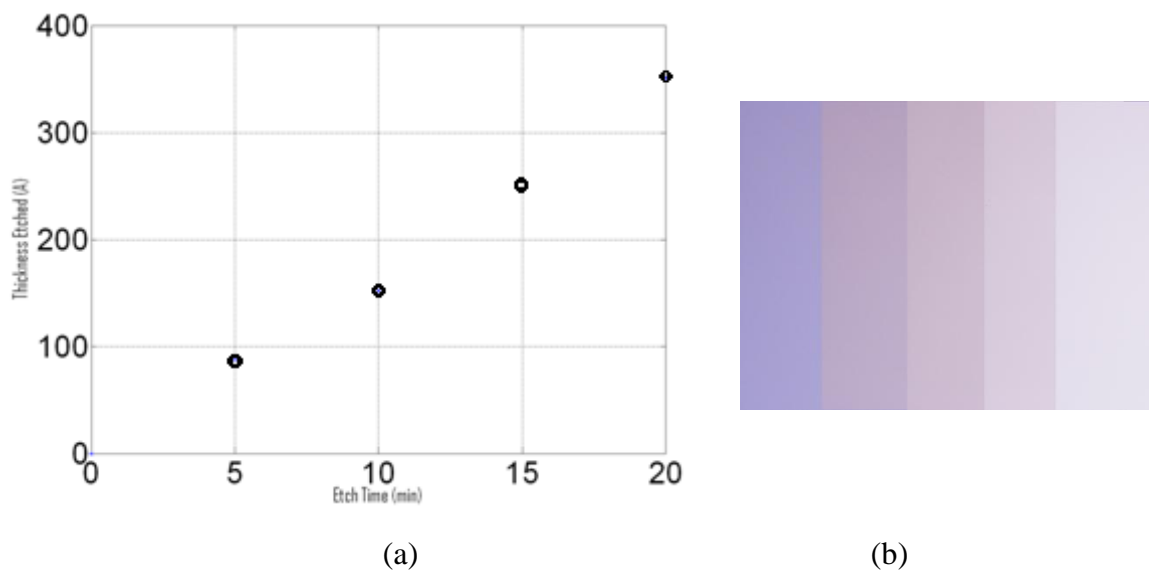
Figure 6.12: (a) Etching rate of an oxidized silicon wafer (90 nm) in KOH (b) Optical contrast of the resulting oxide.

The optical images of the BN layers on 72nm are shown in Fig. 6.13. It was concluded that an oxide thickness of 80 ± 10 nm gives the optimal contrast for thin BN layers. It was found that the contrast reaches ~2.5% per layer, similar for graphene on 90 nm SiO_2.
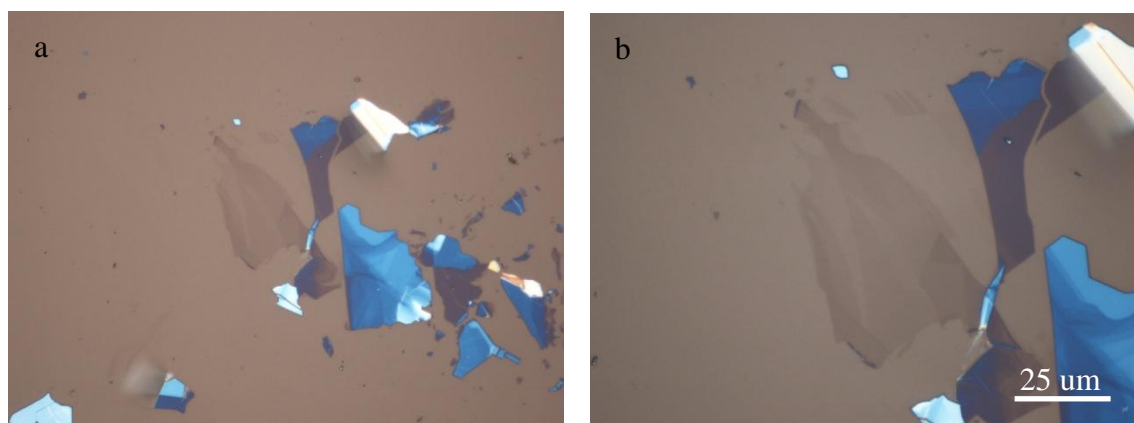
Figure 6.13: Optical images of BN layers on 72 nm Si/SiO_2 at (a) 50x and (b) 100x.

6.3 Results and Discussion

The results of this work have been published in **Small** *in* 2011. In order to best present our results, the original paper "Hunting for Monolayer Boron Nitride: Optical and Raman Signatures" (Small, 7(4), 2011, P 465-468) is attached from the next page.

This work presented was carried out in collaboration with several colleagues of the University of Manchester. My contribution to this work includes the preparation of boron nitride flakes on oxidised silicon substrate by mechanical cleavage and verification of monolayer graphene Si/SiO_2 substrate by optical contrast and atomic force microscopy.

Hunting for Monolayer Boron Nitride: Optical and Raman Signatures

Roman V. Gorbachev, **Ibtsam Riaz**, Rahul R. Nair, Rashid Jalil, Liam Britnell, Branson D. Belle, Ernie W. Hill, Kostya S. Novoselov, Kenji Watanabe, Takashi Taniguchi, Andre. K. Geim, and Peter Blake

Properties of few-nanometer-thick BN sheets (often referred to as few-layer BN) have been attracting steady interest over the last several years. [1] Although individual atomic planes of BN were also isolated [2] and investigated by transmission electron microscopy (TEM) [3-5] and atomic force microscopy (AFM) [6], interest in BN monolayers has been rather limited, especially, if compared with the interest generated by its "sister" material, graphene [7]. This can be attributed to 1) the lack of hexagonal boron nitride (hBN) crystals suitable for the mechanical cleavage approach [7] and 2) difficulties in isolating and finding sufficiently large BN monolayers. The situation is now changing rapidly due to the availability of hBN single crystals, which allow the cleavage of relatively large (~ 100 μm) and relatively thin (several nm) BN samples with an atomically flat surface.[6,8,9] Such crystals have been used as a thin top dielectric to gate graphene[9] and as an inert substrate for graphene devices, which allowed a significant improvement of their electronic quality,[8] unlike the earlier attempts with highly-oriented pyrolytic boron nitride (HOPBN).[10] Most recently, it has been demonstrated that BN films with 2 to 5 layer thickness can also be obtained by epitaxial growth on copper and subsequent transfer onto a chosen substrate.[11] Particularly motivating is the emerging possibility to use BN as an ultra-thin insulator separating graphene layers. The layers could then be isolated electrically but would remain coupled electronically via Coulomb interaction, similar to the case of narrow-spaced quantum well heterostructures.[12] Such atomically thin BN-graphene heterostructures may allow a variety of new interaction phenomena including, for example, exciton condensation.[13]

In the case of graphene, its mono-, bi- and few- layers are often identified by their optical contrast[14] and Raman signatures.[15] Little is known about these characteristics for the case of BN and, in the previous AFM and TEM studies,[2,5,6] one had to rely on finding atomically thin BN regions either randomly or close to edges of thick BN flakes. In this Communication, we report optical and Raman properties of mono- and few-layer BN obtained by micromechanical cleavage of high-quality hBN. Because of its zero opacity (the band gap is larger than 5 eV),[1] atomically-thin BN exhibits little optical contrast, even if the interference enhancement using oxidized Si wafers is employed.[14,16] For the standard oxide thickness of ~ 300 nm SiO_2,[6,7] BN monolayers show white-light contrast of <1.5%, which makes them undetectable by the human eye.[17] Moreover, the contrast changes from positive to negative between red and blue parts of the spectrum, respectively, and goes through zero in green where eye sensitivity is maximum. We show that the use of thinner SiO_2 (≈80±10 nm) offers optimum visualization conditions with contrast of ~ 2.5% per layer, similar to that for graphene on transparent substrates in light transmission mode. Mono- and bi- layers can also be identified by Raman spectroscopy due to shifts in position of the characteristic BN peak that is centered at ≈1366 cm^{-1} in hBN crystals.[1] Monolayers exhibit sample-dependent blue shifts by up to 4 cm^{-1}. This is explained by a hardening of the E_{2g} phonon mode due a slightly shorter B-N bond expected in isolated monolayers,[18] with further red shifts due to random strain induced probably during the cleavage. This strain effect dominates in bilayer, causing red shifts of the Raman peak by typically 1 to 2 cm^{-1}.
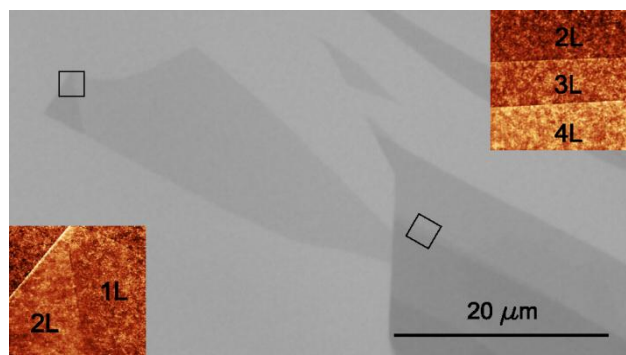
Figure 1. ((Atomically thin BN on top of an oxidized Si wafer (290 nm of SiO_2) as seen in an optical microscope using a yellow filter (λ = 590 nm). The central crystal is a monolayer. For legibility, the contrast is enhanced by a factor of 2. The insets show AFM images of the 3.5x3.5 μm^2 regions indicated by the squares. The step height between the terraces in the images is ~ 4 Å. BN crystals are usually lifted above the wafer by up to extra 10 Å, which can be explained by the presence of a water or contamination layer.[2,6]))

Atomically thin BN crystals were prepared by the standard cleavage procedures[2] and using hBN single crystals grown as described in refs.[19,20] It is important to note that previously we used HOPBN (Momentive Performance Materials) but could only obtain strongly terraced crystallites and no monolayers.[10] BN monolayers mentioned in ref. [2] were extracted from a powder (*Sigma-Aldrich*) and did not exceed a couple of microns in size because of the small size of initial flakes. Using hBN, we can now prepare few-layer samples larger than 100 μm, that is, comparable in size to our single crystals. **(Figure 1)** shows examples of single- and few- layer BN on top of an oxidized Si wafer. The AFM images in Fig. 1 are to illustrate our identification of regions with different thickness.
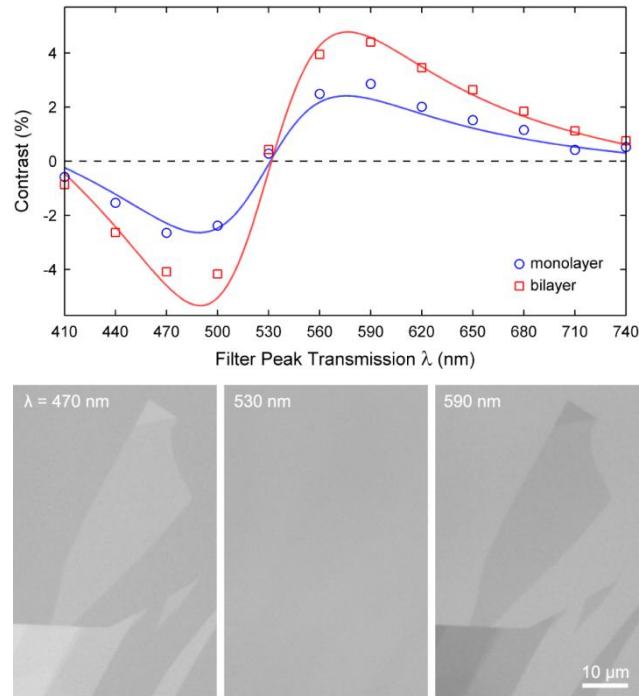
Figure 2. Changes in the optical contrast with wavelength for mono- and bi- layer BN on top of a Si wafer (290 nm SiO_2). We used filters with a 10 nm bandwidth. The solid curves are the dependences expected for mono- and bi- layer BN. In the modeling, we have included the influence of a finite numerical aperture (NA). [21] For the used microscope objective (NA = 0.8), we have integrated over angle assuming a Gaussian weight distribution of width $\theta_{NA}/3$ where θ_{NA} is the maximum acceptance angle of the objective lens.[22] The lower panels show examples of the BN visibility using different filters for the same sample as in Fig. 1. For legibility, the contrast in the images has been enhanced by a factor of 2.

(Figure 2) shows variation of the contrast measured with respect to the bare wafer at different wavelengths λ. To this end, we have taken optical micrographs using illumination through narrow bandpass filters.[14] Representative images for 3 different λ are also presented in Fig. 2. One can see that the contrast is a nonmonotonic function of λ and changes its sign at ~ 530 nm (BN is darker than the substrate at long wavelengths and brighter at short ones). This is different from graphene, in which case the contrast is either

positive or negligible.[14] With increasing the number of BN layers N, the contrast increases proportionally to N. To explain the measured λ dependence, we have used an analysis similar to that reported for graphene [14] and based on the matrix formalism of interference in thin film multilayers.[16] This requires the knowledge of the real n and imaginary k parts of the refractive index. We used spectroscopic ellipsometry for our hBN crystals and found k≈0 and n≈2.2 with a slight upshift for λ <500 nm. Assuming that optical properties of monolayers change little with respect to hBN, we obtain the dependences shown in Fig. 2. The theory accurately reproduces the observed contrast, including its reversal at 530 nm and the absolute value that is related to the extra interference path due to the presence of a transparent monolayer on top of SiO_2.

The developed theory allows us to predict at which SiO_2 thickness the optical contrast for BN monolayers would be maximal. **(Fig. 3)** shows that this is expected for a thickness of 80±10 nm. In this case, the contrast remains relatively strong with the same sign over nearly the entire visible range. This prediction has been confirmed experimentally by imaging BN crystals on top of 90 nm SiO_2. We have found that the contrast reaches ~ 2.5% per layer already in white light (~ 3% with a green filter), and this is sufficient to hunt for and directly see BN monolayers in a microscope. Still note that it is much harder to find BN than graphene monolayers that give a contrast of ~ 10%.[14]
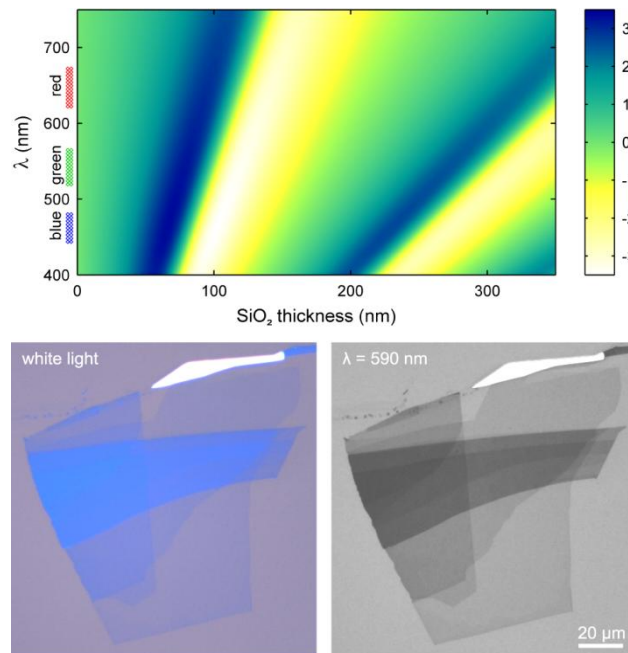
Figure. 3. Optical contrast due to monolayer BN for different λ and SiO_2 thicknesses (top). The plot is for the case of a typical high magnification objective (50X) with NA = 0.8 but changes little for NA = 0.7 or 0.9. The lower images show BN on top of a 90 nm SiO_2/Si wafer (the lower part is a monolayer). Similar to Figures 1 and 2, the contrast is enhanced by a factor of 2.

The optical contrast increases in integer steps (that is, by a factor of N for N-layer BN) and this can be employed for search and identification of mono- and few- layers. However, let us warn that any contamination or a thin layer of water, which is believed to raise atomic crystals above Si wafers, can notably affect the measured contrast. This was previously observed for graphene[22] but the effect becomes much more important for BN because of its weaker contrast. In our experience, it is not unusual for monolayer BN to look like a bilayer. To avoid misidentification and obtain the correct contrast as reported above we annealed our samples at 150 °C in vacuum. For this and other reasons, it is desirable to have another way of confirming BN thickness. Of course, AFM can be used to this end but it is a low throughput technique. For the case of graphene, Raman spectroscopy has proven to be an indispensible tool and, below, we show that it is also useful for identifying monolayer BN.

(Figure 4a) shows Raman spectra of mono-, bi- and tri- layer BN using a green laser with $\lambda = 514.5$ nm. BN exhibits a characteristic peak that is due to the E_{2g} phonon mode and analogous to the G peak in graphene.[1,18] In our hBN single crystals, the Raman peak occurs at ≈ 1366 cm^{-1}. One can see in Fig. 4a that the peak becomes progressively weaker as N decreases and, for monolayer BN, its intensity is ~ 50 times smaller than for graphene's G peak under the same measurement conditions. We have found that the integrated intensity I_T for the BN peak is proportional to N with high accuracy for first several layers (inset in Fig. 4a). Accordingly, once a Raman spectrometer is calibrated for a given substrate, this can be exploited to distinguish between one, two and more BN layers.
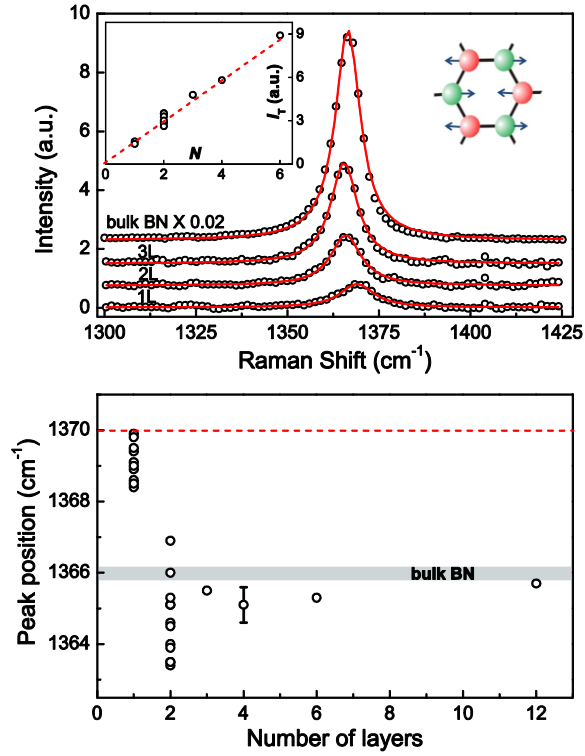
Figure 4. (a) Raman spectra of atomically thin BN. The left inset show changes in integrated intensity I_T with the number of layers N. The right picture illustrates the phonon mode responsible for the Raman peak. (b) Position of the Raman peak for different N. In mono- and bi-layer BN, the peak position is sample dependent and varies by as much as ± 2 cm^{-1}. The dashed line is the Raman shift predicted for monolayer BN.[18] The error bar indicates a typical accuracy of determining the peak position using our spectrometer.

In addition to its intensity proportional to N, we have found that the Raman peak is usually shifted upwards in monolayers and downwards in bilayers with respect to its position in bulk hBN (see Fig. 4b). Monolayers show relatively large shifts (typically, between 2 to 4 cm^{-1}), which vary from sample to sample. The maximum observed blue shift is in agreement with the theory expecting its value to be ≈ 4 cm^{-1} for monolayers.[18] However, Fig. 4 also shows that mono- and bi- layers exhibit unexpectedly strong variations in the peak position whereas these are essentially absent for crystals thicker than 5 layers (not all data for thicker crystals are shown in Fig. 4). To find the origin of these changes, we used different laser powers and ruled out heating effects. We also measured the width of the Raman peaks. The HWHM varied between 10 and 12 cm^{-1} for monolayers and was only marginally larger than the width in hBN (≈ 9 cm^{-1}). No apparent correlation between the width and peak position was found.

To explain the observed variations, we invoke strain that causes additional sample-dependent red shifts in the case of stretching. This is supported by the theoretical and experimental observation of strain induced shift of the Raman peak for the similar material graphene, where the analogous G peak is red-shifted by as much as ~ 20 cm^{-1} per 1% of strain.[23] Strain-induced shifts in pristine graphene deposited on a substrate are completely masked by doping effects[24] which often move the G peak by ~ 10 cm^{-1}. In the absence of such doping effects for insulating BN, strain is expected to become an important factor in determining the Raman peak position. The observed downshifts with respect to the intrinsic blue shift would then imply the stretching of BN monolayers by only a fraction of a percent, which is highly feasible. It seems pertinent to attribute the peak broadening to the same effect. Indeed, strain can also vary within the micron-sized laser spot as monolayers try following the substrate roughness.[25] This argument also applies for bilayers and can explain their random shifts and notably smaller broadening (HWHM of ~ 9 to 10 cm^{-1}). The maximum observed peak position for bilayers in Fig. 4b implies a small intrinsic blue shift of ~ 1 cm^{-1}. We are not aware of any theory for the intrinsic shift in BN bilayers.

In conclusion, BN mono- and bi-layers can be prepared and identified on top of an oxidized Si wafer using the same mechanical exfoliation technique as widely employed for the case of graphene. BN monolayers obtained from hBN crystals can be as big as samples of cleaved graphene and, therefore, should allow a variety of new experiments and proof-of-concept devices, beyond the previous studies by AFM and TEM. The search for atomically thin BN is more difficult than for graphene as the former does not absorb visible light and, therefore, gives rise only to the contrast due to changes in the optical path. Nevertheless, the use of thinner SiO$_2$ and/or narrow optical filters makes it possible to see even BN monolayers. To verify the number of layers, one can employ Raman spectroscopy. It allows the identification of monolayers by an upward shift in the Raman peak position. The shift depends on local strain and, therefore, is not as unambiguous as the Raman signatures for mono- and bi- layer graphene. The step-like increase in the Raman intensity can be used for further confirmation and for counting the number of layers. We believe that the provided analysis and the strategy for hunting for mono- and few-layer BN should facilitate further work on this interesting two-dimensional insulator.))

Experimental Section

Experimental optical contrast and images:

Optical images were taken with a Nikon DS-2MBW monochrome camera in the 12-bit raw mode using narrow band filters (10 nm bandwidth). For each filter, 100 frames were averaged to produce the final image. Exposure times varied in the range 10-300 ms depending on filter. The white light images were taken with a Nikon DS-2MV color camera (100 frames averaged).

Calculations of the optical contrast:

The reflectance of the incident light was calculated (taking into account interference and multiple reflections) for each angular step ranging from normal incidence to the maximum acceptance angle of the objective lens (determined by its 0.8 NA). The difference in reflectance was calculated for the cases of (a) bare substrate and (b) substrate with additional BN layer. The total contrast is the difference in reflectance normalized to substrate value integrated over the angle with a weight distribution determined by the experimental conditions (a Gaussian distribution with a width $\theta_{NA}/3$). The refractive index of BN was taken from our own ellipsometry measurements and those for Si, SiO_2 taken from ref. [26].

The Raman studies were carried with a Renishaw micro-Raman spectrometer at 514 nm excitation wavelength. AFM topography images in Fig. 1 were measured in the intermittent contact mode using a Veeco Dimension V scanning probe microscope.

Acknowledgements

[1]   ((D. Golberg; Y. Bando, Y. Huang, T. Terao; M. Mitome; C. Tang, C. Zhi, *ACS Nano* **2010**, *4*, 2979.))

[2]   ((K. S. Novoselov, D. Jiang, F. Schedin; T. J. Booth, V. V. Khotkevich, S. V. Morozov; A. K. Geim, *Proc. Natl. Acad. Sci. U.S.A.* **2005**, *102*, 10451.))

[3]   ((J. C. Meyer, A. Chuvilin, G. Algara-Siller, J. Biskupek, U. Kaiser, *Nano Lett.* **2009**, *9*, 2683.))

[4]   ((J. H. Warner, M. H. Rümmeli, A. Bachmatiuk, B. Büchner, *ACS Nano* **2010**, *4*, 1299.))

[5]   ((W. Q. Han, L. Wu, Y. Zhu, K. Watanabe, T. Taniguchi, *Appl. Phys. Lett.* **2008**, *93*, 223103.))

[6]   ((C. Lee, Q. Li, W. Kalb, X. Z. Liu, H. Berger, R. W. Carpick, J. Hone, *Science* **2010**, *328*, 76.))

[7]   ((K. S. Novoselov, A. K. Geim, S. V. Morozov, D. Jiang, Y. Zhang, S. V. Dubonos, I. V. Grigorieva, A. A. Firsov, *Science* **2004**, *306*, 666.))

[8]   ((C. R. Dean, A. F. Young, I. Meric, C. Lee, L. Wang, S. Sorgenfrei, K. Watanabe, T. Taniguchi, P. Kim, K. L. Shepard, J. Hone, arXiv:1005.4917, **2010**.))

[9]   ((A. F. Young, C. R. Dean, I. Meric, S. Sorgenfrei, H. Ren, K. Watanabe, T. Taniguchi, J. Hone, K. L. Shepard, P. Kim, arXiv:1004.5556, **2010**.))

[10]   ((L. A. Ponomarenko, R. Yang, T. M. Mohiuddin, M. I. Katsnelson, K. S. Novoselov, S.V. Morozov, A. A. Zhukov, F. Schedin, E. W. Hill, A. K. Geim, *Phys. Rev. Lett.* **2009**, *102*, 206603.))

[11]   ((L. Song, L. Ci, H. Lu, P. B. Sorokin, C. Jin, J. Ni, A. G. Kvashnin, D. G. Kvashnin, J. Lou, B. I. Yakobson, P. M. Ajayan, *Nano Lett.* **2010**, *10*, 3209.))

[12]   ((J. P. Eisenstein, A. H. MacDonald, *Nature* **2004**, *432*, 691.))

[13]   ((H. Min, R. Bistritzer, J. J. Su, A. H. MacDonald, *Phys. Rev. B* **2008**, *78*, 121401.))

[14]   ((P. Blake, E. W. Hill, A. H. Castro Neto, K. S. Novoselov, D. Jiang, R. Yang, T. J. Booth, A. K. Geim, *Appl. Phys. Lett.* **2007**, *91*, 063124.))

[15]   ((A. C. Ferrari, J. C. Meyer, V. Scardaci, C. Casiraghi, M. Lazzeri, F. Mauri, S. Piscanec, D. Jiang, K. S. Novoselov, S. Roth, A. K. Geim, *Phys. Rev. Lett.* **2006**, *97*, 187401.))

[16]   ((W. S. Bacsa, J. S. Lannin, *Appl. Phys. Lett.* **1992**, *61*, 19.))

[17]   ((G. Westheimer, *J. Opt. Soc. Am.* **1972**, *62*, 1502.))

[18]   ((R. Arenal, A. C. Ferrari, S. Reich, L. Wirtz, J. V. Mevellec, S. Lefrant, A. Rubio, A. Loiseau, *Nano Lett.* **2006**, *6*, 1812.))

[19]   ((K. Watanabe, T. Taniguchi, H. Kanda, *Nat. Mater.* **2004**, *3*, 404.))

[20]   ((T. Taniguchi, K. Watanabe, *Journal of Crystal Growth* **2007**, *303*, 525.))

[21]   ((C.Casiraghi, A. Hartschuh, E. Lidorikis, H. Qian, H. Harutyunyan, T. Gokus, K. S. Novoselov, A. C. Ferrari, *Nano Lett.* **2007**, *7*, 2711.))

[22]   ((M. Bruna, S. Borini, *J. Phys. D* **2009**, *42*, 175307.))

[23]   ((T. M. G. Mohiuddin, A. Lombardo, R. R. Nair, A. Bonetti, G. Savini, R. Jalil, N. Bonini, D. M. Basko, C. Galiotis, N. Marzari, K. S. Novoselov, A. K. Geim, A. C. Ferrari, *Phys. Rev. B* **2009**, *79*, 205433.))

[24]   ((C. Casiraghi, S. Pisana, K. S. Novoselov, A. K. Geim, A. C. Ferrari, *Appl. Phys. Lett.* **2007**, *91*, 233108.))

[25]   ((W. G. Cullen, M. Yamamoto, K. M. Burson, J. H. Chen, C. Jang, L. Li, M. S. Fuhrer, E. D. Williams, arXiv:1007.4802, **2010**.))

[26]   ((*Handbook of optical constants of solids* (ed. E. D. Palik), Academic Press,

6.4 Conclusion

Large BN layers can be prepared by the mechanical exfoliation technique as widely used for graphene preparation. Thin layers of BN on oxidized silicon wafer can be identified by optical contrast and Raman spectroscopy. Hunting for atomically thin BN layers is more difficult than for the graphene due to zero opacity of BN. Thin SiO_2 enables to give better contrast for thin BN layers. Raman spectroscopy can be used for counting the number of BN layers on the basis of the BN characteristic peak intensity analysis and monolayer BN can be distinguished by an upward shift in peak position however the shifts are dependent on the local strain. Therefore two dimensional insulator BN layers for different experiments and applications can now be prepared and identified successfully.

Chapter 7

Summary and Outlook

The work presented in this thesis is related to the studies of two materials: graphene and single layer boron nitride, belonging to the novel class of two dimensional crystals [83]. Experiments were made to study the compression behaviour of monolayer graphene made on the plastic substrate by measuring the changes using Raman spectroscopy and to isolate and characterize single layer boron nitride on the Si/SiO_2.

Graphene, a single atomic layer of carbon is the first ever example of this class [3]. One important aspect of graphene is its response under mechanical deformation. Graphene has excellent elastic properties with tensile strength of 1TPa and intrinsic strength of 130 GPa [9]. Graphene can be stretched up to 20% of its actual length [9].Graphene has been extensively studied in terms of its electronic properties which can be modified by applying stress/strain [28,45,46]. Therefore it is necessary to exactly quantify the stress transfer and strain induced in the material for the purpose of strain engineering. Graphene polymer nanocomposite [10,11] is an emerging area of research which needs the precise determination of stress transfer from polymer matrix to the reinforced graphene. Probing the shift in phonon frequencies is an effective mean of monitoring stress transfer to the materials or strain induced in the material. For this purpose Raman spectroscopy has been used as a successful tool. Graphene on bendable plastic substrates [27,39] has attracted much interest for its great potential in both the field of polymer nanocomposites and strain engineering. In the work described here graphene on polymer (PMMA) substrate was successfully prepared and employed for the studies of graphene under various stress. In order to apply mechanical stress to graphene, embedded graphene flakes on PMMA substrate were prepared by mechanical exfoliation of graphite. Graphene flakes of different geometries and sizes were prepared and analyzed under uniaxial deformation (tension and compression). Monolayer graphene was confirmed by the Raman analysis of the graphene. Graphene flakes were subjected to mechanical deformation by using polymer cantilever beam technique that can be flexed up and down by adjustable screw applying compression and tension to the graphene flakes. The deflection δ was measured accurately using a dial gauge micrometer attached to the top surface of the beam. The

stress was applied smoothly with strain increment of 0.03 or 0.05 % to avoid the slippage and the maximum strain of 0.7% was obtained. The respective mechanical response of the graphene was studied by Raman spectroscopy measurements. Raman spectra were taken using 785 nm (1.58eV) excitation source. Raman G and 2D bands were studied as a function of the applied strain, and the shifts in Raman G and 2D band positions under compression and tension were analyzed; indicating that the change in phonon frequencies is a result of stress transfer to the graphene substrate. A non-linear response of G and 2D band was observed and the corresponding slopes $\partial\omega_{G,2D}/\partial\varepsilon$ decrease with strain till the

eventual turnover of the slope, indicating progressive buckling and final breakdown of the graphene flake. The buckling strain was found to be dependent on the graphene flake size and geometry. For the graphene flakes having length to width (l/w) ratios ≥ 0.2, the buckling strain is of the order of -0.5% to -0.6% whereas for graphene flakes with l/w ratios < 0.2 no failure is observed for strains even higher than -1%. Classical Euler analysis for critical buckling strain showed that the polymer (PMMA) substrate provide lateral support to the graphene and enhances the buckling strain of graphene by 6 orders of magnitude as compared to the suspended graphene in air .

Further improvement is required in the experimental work related to the graphene on polymer (flexible) substrate. The limitation to study the changes in graphene at large deformations (tension or compression) is that the graphene flakes on polymer substrate slip under large value of stress. The adhesion between the substrate and the graphene flakes needs to be improved by either improving sample making or strain application procedure so that changes in the graphene can be studied experimentally to support the theoretical data available in this regard. This strengthening of the polymer and graphene can be useful for its applications in different technological fields. Moreover transport measurement can be performed for a graphene device on polymer substrate under strain. The comparison of the transport properties of the strained and unstrained graphene can be useful for tuning of electronic properties of graphene by applying strain in the field of strain engineering [28,45].

In the second part of the thesis boron nitride layers were isolated from the bulk boron nitride using the same technique of mechanical cleavage [3] as used for graphene separation due to its layered structure. Boron nitride layers of large size (50-100 μm) were obtained by mechanical exfoliation. Monolayer boron nitride on 300 nm Si/SiO$_2$ gives very poor optical contrast. In order to find the maximum optical contrast condition different oxide thickness of Si/SiO$_2$ was used to make cleaved boron nitride samples. The

percentage contrast analysis of boron nitride layers on different oxide thickness of Si/SiO_2 shows that the oxide thickness of 80 ± 10 nm gives maximum optical contrast. Atomic force microscopy was used to confirm the thickness of the boron nitride layers. Raman spectroscopy is an unambiguous technique for counting the number of graphene layers therefore Raman spectra of boron nitride were also analysed. Boron nitride Raman characteristic peak ≈ 1366 cm^{-1} was studied and it was observed that as the number of boron nitride layers decreases the boron nitride peak becomes weaker. The position of the peak of boron nitride layers was closely analyzed and it was found that the monolayers shift to higher frequencies whereas bilayer and other thick BN layers shift toward lower frequencies with respect to the bulk BN peak position. Therefore Raman spectra of boron nitride layers can be successfully used to identify the number of boron nitride layers. Single layer boron nitride, a member of two dimensional class of materials and few layer boron nitride can now be fabricated and identified successfully.

These boron nitride layers of different thickness and size with an atomically flat surface [68,94] can be used in various graphene based devices for fundamental studies and future applications. Mobility of graphene is one of the important properties of graphene which always attract interest. Routinely room temperature mobilities of ~20,000 cm^2/Vs are obtained on Si/SiO_2. The graphene high mobility is limited by the absence of the suitable substrate. A suitable homogenous, inert and thermodynamically stable substrate was always needed in graphene based electronics and few layer boron nitride has been proven to be an ideal candidate for this purpose [68]. In addition to this, as two dimensional boron nitride can serve as a better substrate for the graphene, it can be utilized as a thin top dielectric to gate graphene [94] and thin insulator in graphene-boron nitride heterostrutures.

References

1. Katsnelson, M. I., *Materials Today* **10**, 20 (2007).

2. Geim, A. K., and K. S. Novoselov, *Nature Materials* **6**, 183 (2007).

3. K. S. Novoselov, A. K. Geim, S. V. Morozov, D. Jiang,Y. Zhang, S. V. Dubonos, I. V. Gregorieva, and A. A.Firsov, *Science* **306**, 666 (2004).

4. Novoselov, K. S., A. K. Geim, S. V. Morozov, D. Jiang, M. I. Katsnelson, I. V. Grigorieva, S. V. Dubonos, and A. A. Firsov, *Nature* **438**, 197 (2005).

5. Wallace. P. R., *Phys. Rev*. **71**, 622 (1947).

6. A. H. Castro Neto, F. Guinea, N. M. R. Peres, K. S. Novoselov, A. K. Geim, *Rev. Mod. Phys.* **81**, 109 (2009).

7. J. C. Charlier, P.C. Eklund, J. Zhu, A.C. Ferrari, *Topics Appl. Phys*. **111**, 673 (2008).

8. Y.-M. Lin, K. A. Jenkins, A. Valdes-Garcia, J. P. Small, D. B. Farmer and P. Avouris, *Nano Letters* **9**, 422 (2008).

9. Changgu Lee, Xiaoding Wei, Jeffrey W. Kysar, James Hone, *Science* **321**, 385 (2008).

10. S. Stankovich, D. A. Dikin, G. H. B. Dommett, K. M. Kohlhaas, E. J.Zimney, E. A. Stach, R. D. Piner, S. T. Nguyen and R. S. Ruoff, *Nature* **442**, 282 (2006).

11. RamanathanT, A. A. Abdala, StankovichS, D. A. Dikin, M. Herrera, Alonso, R. D. Piner, D. H. Adamson, H. C. Schniepp, ChenX, R. S.Ruoff, S. T. Nguyen, I. A. Aksay, R. K. Prud'Homme and L. C. Brinson, *Nature Nanotech.* **3**, 327 (2008).

12. Nair, R. R.; Blake, P.; Grigorenko, A. N.; Novoselov, K. S.; Booth,T. J.; Stauber, T.; Peres, N. M. R.; Geim, A. K. *Science* **320**, 1308 (2008).

13. D. C. Elias, R. R. Nair, T. M. G. Mohiuddin, S. V. Morozov, P. Blake, M. P.Halsall, A. C. Ferrari, D. W. Boukhvalov, M. I. Katsnelson, A. K. Geim, K. S. Novoselov, *Science* **323**, 610 (2009).

14. R. R. Nair, W. Ren, R. Jalil, I. Riaz, V. G. Kravets, L.Britnell, P. Blake, F. Schedin, A. S. Mayorov, S. Yuan, M.I. Katsnelson, H.-M. Cheng, W. Strupinski, L. G. Bulusheva, A. V. Okotrub, I. V. Grigorieva, A. N. Grigorenko,K. S. Novoselov, A. K. Geim, *Small* **6**, 2877 (2010).

15. http://invsee.asu.edu/nmodules/carbonmod/crystalline.html

16. Structural Properties of Graphene and Carbon Nanotubes, Brian Shevitski Department of Physics and Astronomy, University of California Los Angeles, LosAngeles, CA90095 (Dated: September28, 2010) reu.physics.ucla.edu/common/papers/2010/shevitski_brian.pdf

17. http://www.itp.phys.ethz.ch/education/lectures_fs11/solid/sol05.pdf

18. Geim, A. K., and A. H. MaDonald, Physics Today 60, 35 (2007).

19. Marcus Freitag, *Nature Nanotech*. **3**, 455 (2008).

20. Saito, R., G. Dresselhaus, and M. S. Dresselhaus, *Physical properties of carbon nanotubes* ,Imperial College Press,London (1998).

21. Reih, S., J. Maultzsh, C. Thomsen, and P. Ordejón, *Phys. Rev. B* **66**, 035412 (2002).

22. H.S. Philip Wong and Deji Akinwande, *Carbon Nanotube and Graphene Device Physics*, Cambridge University Press (2011).

23. Tsuneya Ando, *NPG Asia Mater*. **1**, 17 (2009).

24. A. Reina, X. Jia, J. Ho, D. Nezich, H. Son, V. Bulovic, M. S. Dresselhaus and J. Kong, *Nano Lett*. **9**, 30 (2008).

25. P. Blake, K. S. Novoselov, A. H. Castro Neto, D. Jiang, R. Yang, T. J. Booth, A. K. Geim, and E. W. Hill, *Appl. Phys. Lett*. **91,** 063124 (2007).

26. A.C.Ferrari, J.C.Mayer, V.Scardaci, C.Casiraghi, M.Lazzeri, F.Mauri, S. Piscanec, D. Jiang, K. S Novoselov, S. Roth and A.K Geim, *Phy. Rev. Lett*. **97,** 187401 (2006).

27. T. M. G. Mohiuddin, A. Lombardo, R. R. Nair, A. Bonetti, G. Savini, R.Jalil, N. Bonini, D.M. Basko, C. Galiotis, N. Marzari, K. S. Novoselov, A.K. Geim, A. C. Ferrari. *Phy. Rev. B* **79**, 205433 (2009).

28. F. Guinea, M. I. Katsnelson & A.K. Geim, *Nature Phys*. **6**, 30 (2010).

29. Mildred S. Dresselhaus, Ado Jorio, Mario Hofmann, Gene Dresselhaus, and Riichiro Saito, *Nano Lett*. **10**, 751(2010).

30. John R. Ferraro, Kazuo Nakamoto and Chris W. Brown, *Introductory Raman Spectroscopy* second Edition, Academic Press (1994).

31. Maher S. Amer, *Raman Spectroscopy, Fullerences and Nanotechnology*, RSC publishing (2010).

32. Ado Jorio, Mildred Dresselhaus, Riichiro Saito, and Gene F. Dresselhaus, *Raman Spectroscopy in Graphene Related Systems*, WILEY-VCH Verlag GmbH & Co. KGaA, Weinhei (2011).

33. Jun Yan, Yuanbo Zhan, Sarah Goler, Philip Kim, Aron Pinczuk, *Solid State Communications* **143,** 39 (2007).

34. A.C. Ferrari, *Solid State Commun*. **143**, 47 (2007).

35. L.M. Malard, M.A. Pimenta, G. Dresselhaus, M.S. Dresselhaus, *Physics Reports* **473**, 51 (2009).

36. C. Casiraghia, S. Pisana, K. S. Novoselov , A. K. Geim and A. C. Ferrari, *Appl. Phys. Lett*. **91**, 233108 (2007).

37. Ying ying Wang, Zhen hua Ni, Ting Yu, Ze Xiang Shen, Hao min Wang, Yi hong Wu,Wei Chen and Andrew Thye Shen Wee, *J. Phys. Chem. C* **112***,* 10637 (2008).

38. C.Thomsenand, S. Reich, *Phys. Rev. Lett*. **85**, 5214 (2000).

39. Yu, T.; Ni, Z. H.; Du, C. L.; You, Y. M.; Wang, Y. Y.; Shen, Z. X., *J. Phys.Chem.C* **112**, 12602 (2008).

40. Mingyuan Huang, Hugen Yan, Changyao Chena, Daohua Song,Tony F. Heinz and James Hone, *PNAS* **106**, 7304 (2009).

41. Georgia Tsoukleri, John Parthenios, Konstantinos Papagelis, Rashid Jalil, Andrea C. Ferrari, Andre K. Geim, Kostya S. Novoselov, and Costas Galiotis, *Small* **5**, 2397 (2009).

42. Ricardo Faccio, Luciana Fernández-Werner, Helena Pardo, Cecilia Goyenola, Pablo A. Denis and Álvaro W. Mombrú (2011). Mechanical and Electronic Properties of Graphene Nanostructures, Physics and Applications of Graphene - Theory, Sergey Mikhailov (Ed.), ISBN: 978-953-307-152-7, InTech, Available from: http://www.intechopen.com/articles/show/title/mechanical-and-electronic-properties-of-graphene-nanostructures

43. Zhen Hua Ni, Ting Yu, Yun Hao Lu, Ying Ying Wang, Yuan Ping Feng and Ze Xiang Shen, *ACS Nano* **2**, 2301 (2008).

44. Vitor M. Pereira, A. H. Castro Neto and N. M. R. Peres, *Phys. Rev. B* **80**, 045401 (2009).

45. Vitor M. Pereira, A. H. Castro Neto and N. M. R. Peres, *Phys. Rev. Lett*. **103**, 046801 (2009).

46. Seon-Myeong Choi, Seung-Hoon Jhi, and Young-Woo Son, *Phys. Rev. B* **81**, 081407 (2010).

47. M. Y. Han, B. Özyilmaz, Y. Zhang, and P. Kim. *Phys. Rev. Lett*. **98**, 206805 (2007).

48. F. Sols, F. Guinea, and A. H. Castro Neto. *Phys. Rev. Lett*. **99**,166803. (2007).

49. Xue, K. & Xu, Z, *Appl. Phys. Lett*. **96**, 063103 (2010).

50. Zhu, T.; Li, J., *Progress in Materials Science* **55**, 710 (2010).

51. Zhiping Xu (2011), Nano-Engineering of Graphene and Related Materials, Physics and Applications of Graphene Sergey Mikhailov (Ed.), ISBN: 978-953-307-217-3,InTech,Availablefrom: http://www.intechopen.com/articles/show/title/nano-engineering-of-graphene-and-related-materials

52. Paul, D. R.; Robeson, L. M., *Polymer* **49**, 3187 (2008).

53. Jeffrey R. Potts , Daniel R. Dreyer , Christopher W. Bielawski , Rodney S. Ruoff, *Polymer* **52**, 5 (2011).

54. Gong, L.; Kinloch, I. A.; Young, R. J.; Riaz, I.; Jalil, R.; Novoselov,K. S; *Adv. Mater.* **22**, 2694 (2010).

55. M. S. Dresselhaus, G. Dresselhaus, Ph. Avouris (Eds.): Carbon Nanotubes, Topics *Appl. Phys.* **80**, pp. 287 − 327 (2001).

56. Jacob N. Israelachvili, Intermolecular and Surface Forces: Revised Third Edition, Academic press publications 2011.

57. Qiang Lu and Rui Huang, *International Journal of Applied Mechanics* **1**, 443(2009).

58. Bolotin, K. I., Sikes, K. J., Jiang, Z., Klima, M., Fudenberg, G.Hone, J., Kim, P., Stormer, H. L. *Solid State Commun*. **146**, 351 (2008).

59. Balandin, A. A. Ghosh, S. Bao, W. Z. Calizo, I. Teweldebrhan,D. Miao, F.Lau, C. N., *Nano Lett*. **8**, 902 (2008).

60. L. A. Ponomarenko, F. Schedin, M. I. Katsnelson, R. Yang, E. W. Hill,K. S. Novoselov and A.K.Geim, Science **320**, 356 (2008).

61. M.C. Lemme, T.J. Echtermeyer, M. Baus, H. Kurz, *IEEE Electron Device Letters*. **28**, 282 (2007).

62. Dean, C. R.; Young, A. F.; Meric, I.; Lee, C.; Wang, L.;Sorgenfrei, S.; Watanabe, K.; Taniguchi, T.; Kim, P.; Shepard, K. L.;Hone, J., *Nature. Nanotech*. **5**, 722 (2010).

63. E. R. Mucciolo, A. H. Castro Neto, and C. H. Lewenkopf. *Phys. Rev. B* **79**, 075407 (2009).

64. D.Basu, M.J. Gilbert, L.F. Rgister and S.K. Banerjee, A. H. MacDonald, *Appl. Phys. Lett.* **92**, 042114 (2008).

65. X. Wang, Y. Ouyang, X. Li, H. Wang, J. Guo, and H. Dai*, Phys. Rev. Lett.* **100**, 206803 (2008).

66. Liu Yang and Jie Han, *Phys. Rev. Lett*. **85**, 154 (2000).

67. E. D. Minot, Yuval Yaish, Vera Sazonova, Ji-Yong Park, Markus Brink, and Paul L. McEuen *Phys. Rev. Lett*. **90**, 156401 (2003).

68. Ting Yu, Zhenhua Ni, Chaoling Du, Yumeng You, Yingying Wang, and Zexiang Shen, ACS Nano, *J. Phys. Chem. C* **112**, 12602 (2008).

69. Keun Soo Kim, Yue Zhao, Houk Jang, Sang Yoon Lee, Jong Min Kim, Kwang S. Kim, Jong-Hyun Ahn, Philip Kim, Jae-Young Choi& Byung Hee Hong, *Nature* **457,** 706 (2009).

70. M. M. Fogler, F. Guinea, and M. I. Katsnelson, *Phys. Rev. Lett*. **101**, 226804 (2008).

71. Horacio J. Salavagione, Gerardo Martínez and Gary Ellis (2011). Graphene-Based Polymer Nanocomposites, Physics and Applications of Graphene Sergey Mikhailov (Ed.), ISBN: 978-953-307-217-3, InTech, Available from: http://www.intechopen.com/articles/show/title/graphene-based-polymer-nanocomposites.

72. Moniruzzaman, M.; Winey, K. I., *Macromolecules* **39**, 5194 (2006).

73. Okamoto, M. Polymer/Clay Nanocomposites; American Scientific Publishers: Stevenson Ranch, CA, 2004; Vol. **8**.

74. Xin Zhao, Qinghua Zhang, and Dajun Chen, *Macromolecules* **43**, 2357 (2010).

75. Hyunwoo Kim, Ahmed A. Abdala, and Christopher W. Macosko, *Macromolecules* **43**, 6515 (2010).

76. Mingyuan Huang, Hugen Yan, Changyao Chen, Daohua Song, Tony F. Heinz and James Hone, *PNAS* **106**, 7304 (2009).

77. http://en.wikipedia.org/wiki/Buckling.

78. Iijima S, Brabec C, Maiti A and Bernholc J, *J. Chem.Phys.* **104,** 2089 (1996).

79. O. Lourie, D. M. Cox, and H. D. Wagner, *Phys. Rev. Lett*. **81**, 1638 (1998).

80. M. R. Falvo, G. J. Clary, R. M. Taylor,II, V. Chi, F. P. Brooks, Jr, S. Washburn and R. Superfine, *Nature* **389**, 582 (1997).

81. Timoshenko, S. P.; Gere, J. M. Theory of Elastic Stability; McGraw-Hill: New York, 1961.

82. Tsoukleri, G.; Parthenios, J.; Papagelis, K.; Jalil, R.; Ferrari,Geim, A. K.; Novoselov, K. S.; Galiotis, C. Subjecting a Graphene Monolayer to Tension and Compression. *Small* **5**, 2397 (2009).

83. Novoselov, K. S., D. Jiang, F. Schedin, T. J. Booth, V. V.Khotkevih, S. V. Morozov, and A. K. Geim, , *Proc. Natl. Acad. Sci. USA* **102**, 10451(2005).

84. Hugh O. Pierson, *"Handbook of refractory carbides and nitrides: properties, characteristics, processing and Applications"* Noyes Publications, 1996.

85. R. Geick, C.H. Perry and G. Rupprecht, *Phys. Rev*. **146**, 543 (1966).

86. Wei-Qiang Han, Lijun Wu, Yimei Zhu, Kenji Watanabe, and Takashi Taniguchi, *Appl. Phys. Lett*. **93**, 223103 (2008).

87. Pierson, H. O., *Handbook of Carbon, Graphite, Diamond and Fullerenes,* Noyes Publications, Park Ridge, NJ (1993)

88. Kenji Watanabe, Takashi Taniguchi & Hisao Kanda, *Nature Materials* **3**, 404 (2004).

89. D. Golberg , Y. Bando, Y. Huang, T. Terao, M. Mitome, C. Tang, C. Zhi, *ACS Nano* **4**, 2979 (2010).

90. Ni, Z. H., L. A. Ponomarenko, R. R. Nair, R. Yang, S. Anissimova, I. V. Grigorieva, F. Schedin, P. Blake, Z. X. Shen, E. H. Hill, K. S. Novoselov, and A. K. Geim, *Nano Lett*. **10**, 3868 (2010).

91. E. H. Hwang, S. Adam, and S. Das Sarma, *Phys. Rev. Lett*. **98**, 186806 (2007).

92. J. H. Chen, C. Jang, S. Xiao, M. Ishigami, M. S. Fuhrer, *Nature Nanotech*. **3**, 206 (2008).

93. Ishigami, M., J. H. Chen, D. W. G. Cullan, M. S. Fuhrer, and E. D. Williams, *Nano Lett*. **7**, 1643 (2007).

94. A. F. Young , C. R. Dean , I. Meric , S. Sorgenfrei , H. Ren , K. Watanabe , T. Taniguchi , J. Hone , K. L. Shepard , P. Kim , arXiv:1004.5556, 2010 .

95. Digital Instruments, *Scanning Probe Microscopy Training Notebook Version 3.0*, 2000.

96. P. Blake, P. D. Brimicombe, R.R. Nair, T. J. Booth, D. Jiang, F. Schedin, L. A. Ponomarenko, S. V. Morozov, H. F. Gleeson, E. W. Hill, A. K. Geim, K. S. Novoselov, *Nano Lett.* **8**, 1704 (2008).

97. Gong, L.; Kinloch, I. A.; Young, R. J.; Riaz, I.; Jalil, R.; Novoselov, K. S. *Adv Mater* **22**, 2694 (2010).

98. O. Frank, G. Tsoukleri, I. Riaz, K. Papagelis, J. Parthenios, A. C. Ferrari, A. K. Geim, K.. S. Novoselov & C. Galiotis, *Nature Communications* **2**, 225 (2011).

99. Ingrid De Wolf, *Semicond. Sci. Technol.* **11,** 139 (1996) .

100. O. Lourie and H. D. Wagner, *J. Mater. Res.* **13**, 2418 (1998).

101. V. G. Hadjiev, M. N. Iliev, S. Arepalli, P. Nikolaev and B. S. Files, *Appl. Phys. Lett*. **78**, 3193 (2001).

102. B. Radisavljevic, A. Radenovic, J. Brivio, V. Giacometti and A. Kis, *Nat. Nanotceh.* **6**, 147 (2011).

103. Yu-Ming Lin, Alberto Valdes-Garcia, Shu-Jen Han, Damon B. Farmer, Inanc Meric,Yanning Sun, Yanqing Wu, Christos Dimitrakopoulos, Alfred Grill, Phaedon Avouris, Keith A. Jenkins, *Science* **332**, 1294 (2011).

104. http://research.nokia.com/page/11906.

105. Augustin J. Hong, Emil B. Song, Hyung Suk Yu, Matthew J. Allen, Jiyoung Kim, Jesse D. Fowler, Jonathan K. Wassei, Youngju Park, Yong Wang, Jin Zou, Richard B. Kaner, Bruce H. Weiller, and Kang L. Wang, *ACS Nano*, Articles ASAP (2011).

106. http://www.manchester.ac.uk/aboutus/news/display/?id=7484

107. L. A. Ponomarenko, A. K. Geim, A. A. Zhukov, R. Jalil, S. V. Morozov, K. S. Novoselov, I. V. Grigorieva, E. H. Hill, V. V. Cheianov, V. I. Fal'ko, K. Watanabe, T. Taniguchi and R. V. Gorbachev, *Nature Physcics*, Published online Oct. 2011.

Appendix

List of Publications

1. OtakarFrank, Georgia Tsoukleri, John Parthenios, Konstantinos Papagelis, **Ibtsam Riaz**, Rashid Jalil, Kostya S. Novoselov, Costas Galiotis "Compression Behavior of Single-layer Graphene" *ACS Nano* **4**, 3131 (2010).

2. . L. Gong, I. A. Kinloch, R. J. Young, **I. Riaz**, R. Jalil, K. S. Novoselov "Interfacial Stress Transfer in a Graphene Monolayer Nanocomposite" *Advanced Materials* **22**, 2694 (2010).

3. R. R. Nair, W. C. Ren, R. Jalil, **I. Riaz**, V. G. Kravets, L. Britnell, P. Blake, F. Schedin, A. S. Mayorov, S. Yuan, M. I. Katsnelson, H. M. Cheng, W. Strupinski, L. G. Bulusheva, A. V. Okotrub, I. V. Grigorieva, A. N. Grigorenko, K. S. Novoselov, A. K. Geim "Fluorographene: Two Dimensional Counterpart of Teflon" *Small* **6**, 2773 (2010).

4. Otakar Frank, Georgia Tsoukleri, **Ibtsam Riaz**, Konstantinos Papagelis, John Parthenios, Andrea C. Ferrari, Andre K. Geim, Kostya S. Novoselov, Costas Galiotis "From Graphene to Carbon Fibres: Mechanical Deformation and Development of a Universal Stress Sensor" *Nature Communications* **2**, 1 (2011).

5. Otakar Frank, Marcel Mohr, Janina Maultzsch, Christian Thomsen, **Ibtsam Riaz**, Rashid Jalil, Kostya S. Novoselov, Georgia Tsoukleri, John Parthenios, Konstantinos Papagelis,Ladislav Kavan, Costas Galiotis "Raman 2D-Band Splitting in Graphene: Theory and Experiment" *ACS Nano* **5**, 2231 (2011).

6. Robert J. Young, Lei Gong, Ian A. Kinloch, **Ibtsam Riaz**, Rashid Jalil, and Kostya S. Novoselov "Strain Mapping in a Graphene Monolayer Nanocomposite" *ACS Nano* **5**,3079 (2011).

7. R. V. Gorbachev, **I. Riaz**, R. R. Nair, R. Jalil, L. Britnell, B. D. Belle, E. W. Hill, K. S. Novoselov, K. Watanabe, T. Taniguchi, A. K. Geim, P. Blake "Hunting for Monolayer Boron Nitride: Optical and Raman Signatures" *Small* **7**, 465 (2011).

8. Robert J. Young, Lei Gong, Ian A. Kinloch, **Ibtsam Riaz**, Rashid Jalil, and Kostya S. Novoselov "Optimizing the Reinforcement of Polymer-Based Nanocomposites by Graphene" Submitted to ACS Nano.

9. Otakar Frank, Milan Bousa, **Ibtsam Riaz**, Rashid Jalil, Kostya Novoselov, Georgia Tsoukleri, John Parthenios, Ladislav Kavan, Kostas Papagelis, Galiotis C. "Phonon and structural changes in deformed Bernal stacked bilayer graphene" Submitted to Nano Letters.